TECHNISCHE UNIVERSITÄT WIEN

Diploma Thesis

Age, Sex and Treatment Related Changes of Bone Mineral Density Based on CT Data

carried out for the purpose of obtaining the degree Master of Science,
submitted at TU Wien, Faculty of Mechanical and Industrial Engineering, by

Sebastian BACHMANN

Mat.Nr.: 00925947
Senekowitschgasse 3/3/10, 1220 Wien, Austria

under the supervision of

Associate Prof. Dipl.-Ing. Dr.techn. Dieter Pahr

Institute of Lightweight Design and Structural Biomechanics, E317

Affidavit

I declare in lieu of oath, that I wrote this thesis and performed the associated research myself, using only literature cited in this volume. If text passages from sources are used literally, they are marked as such. I confirm that this work is original and has not been submitted elsewhere for any examination, nor is it currently under consideration for a thesis elsewhere.

Vienna, October 2018

Signature

Essentially, all models are wrong,
but some are useful.

GEORGE BOX

Abstract

People lose bone mass as they age. The overall rate of bone loss is a simple indicator showing age, sex, or treatment related changes. *In-vivo* screening methods to measure bone density are DXA or QCT. Usually mean densities over defined ROIs are evaluated. In this work a new approach is presented. A novelty is the usage of density distributions based on ROIs instead of a single value. Statistical models based on BVTV are created which give insight into the changes at specific sites inside the bone. These models are called "BVTV frequency models". Changes between groups of people can be seen by using "BVTV frequency difference models". Such models were constructed for age related changes at the radius using HR-pQCT data for both men and women and treatment related changes at the lumbar spine and femoral head using QCT data for postmenopausal women treated with Denosumab. Additionally, a simple geometrical model for the specific surface in dependency of the current relative density was developed and used in a rate based remodelling model. This model was then used to predict the changes of bone volume over total volume (BVTV) in the radius data set.

Age related changes can be seen in the bone frequency difference model. The trabecular distribution shifted to lower BVTV values and the cortical distribution decreased in magnitude. The total turnover rate was more than twice as fast in women as in men. Men showed loss in denser regions than women. Treatment related changes can be observed as well, both in the lumbar spine as well as in the femoral head. While the placebo group lost bone in the trabecular distribution, the treated group gained bone in those regions. Only a trabecular but no cortical increase was observed in both bones.

The rate based remodelling model was not able to explain all parts of the changes. The overall trend was observed though but the predicted curve did deviate largely from the actual curve.

Bone frequency models can not only be used to examine changes in ageing but also differences between sex or treatments. The frequency distribution gives more insight into the changes than a single density value. The number of samples in the radius data set was too small for a more accurate evaluation. The resolution of the HR-pQCT data was not enough to show cortical changes in detail. Such models can be created from existing QCT data without any additional effort for the patient.

Zusammenfassung

Menschen verlieren mit zunehmendem Alter an Knochenmasse. Die globale Rate des Knochenverlusts ist dabei ein einfacher Indikator für alters-, geschlechts- oder behandlungsbedingte Veränderungen. *In-vivo* Untersuchungsmethoden zur Messung der Knochendichte sind Dual-Röntgen-Absorptiometrie (DXA) oder quantitative Computertomografie (QCT). Üblicherweise werden gemittelte Dichten über definierten Bereiche (ROI) ausgewertet. In dieser Arbeit wird ein neuer Analyseansatz vorgestellt. Neu dabei ist die Verwendung von Grauwertverteilungen von kleineren Auswertebreichen sowie eine Unterscheidung zwischen kortikalen und trabekulären Knochenregionen mittels segmentierter 3D-CT-Daten. Es werden statistische Modelle anhand von BVTV erstellt, welche einen Einblick in die Veränderungen an bestimmten Stellen im Knochen geben. Diese Modelle werden "BVTV Frequenz-Modelle" genannt. Änderungen zwischen verschiedenen Altersgruppen können anhand von "BVTV Frequenz-Differenz Modellen" gezeigt werden. Zusätzlich wurde ein analytisches Modell der Knochen-Mikrostruktur, sowie ein Raten basiertes Remodelling Modell erstellt. Beide Modelle wurden zur Vorhersage der altersbedingten Änderungen des Knochens verwendet.

BVTV Frequenz-Modelle wurden für drei verschiedene Knochen erzeugt. Den Radius, proximalen Femur und Lendenwirbel. Am Radius wurden altersbedingte Veränderungen untersucht, an den anderen beiden Knochen die Veränderung durch medikamentöse Behandlung and postmenopausalen Frauen. Altersbedingte Veränderungen konnten in den den Frequenz-Modellen gefunden werden. Die trabekuläre Verteilung verschob sich dabei hin zu niedrigeren Werten, während die kortikale Verteilung kleiner und die Verteilung der Hohlräume größer wurde. Behandlungsspezifische Veränderungen konnten ebenfalls festgestellt werden, während die Placebo-Gruppe Knochen im trabekulären Bereich verlor, konnte dieser in der behandelten Gruppe aufgebaut werden. Das analytische Modell wurde schlussendlich auf die Radius Daten angewendet, allerdings konnten nur schwache Voraussagen getroffen werden. Einige Aspekte der Knochenalterung konnten durch das Modell dennoch gezeigt werden.

Knochen-Frequenz-Modelle können nicht nur verwendet werden, um Veränderungen im Alter, sondern auch Unterschiede zwischen Geschlecht oder Behandlungen zu untersuchen. Diese Unterschiede können nun nicht nur mit einem einzelnen Mittelwert gezeigt werden, sondern auch für unterschiedliche Bereiche im Knochen. Die Anzahl der Radius Datensätze war zu klein, um genauere Aussagen über die Alterungseffekte zu erhalten, auch war die Auflösung der CT Daten zu gering, um Veränderungen der Kortex korrekt zu erfassen, da kortikale Poren nicht genau genug aufgelöst wurden. Die generelle Anwendbarkeit von Knochen-Frequenz-Modellen konnte gezeigt werden, etwa zur Überwachung des Osteoporose Status oder in der Anwendung als Remodelling Modell. Knochen Frequenz Modelle können ohne weiteren Aufwand aus bestehenden Datensätzen gewonnen werden und stellen für Patienten keinen Mehraufwand dar.

Acknowledgements

I would like to thank all members of the Institute of Lightweight Design and Structural Biomechanics (ILSB), where this diploma thesis was carried out, in particular my supervisor Dr. Dieter Pahr for his guidance as well as Lukas Steiner and Alexander Synek for many helpful discussions.

A special thanks goes to my family and friends, for their support throughout my studies.

Contents

Acronyms

aBMD areal bone mineral density. 5, 10, 17

B.Ar.T.Ar. bone area over total area. 5, 11

BMC bone mineral content. 5, 41, 67

BMD bone mineral density. 5, 10, 12–14, 16, 17, 19, 20, 22–25, 35, 36, 38, 41–44, 58, 67

BMU bone multicellular unit. 5, 35

B.Pm.T.Ar. bone perimeter over total area. 5, 11

BSTV bone surface over total volume. 4, 5, 11, 12, 16, 34, 35, 40, 52, 54, 56, 57, 68–70

BVTV bone volume over total volume. 1, 2, 4, 5, 11, 12, 16, 19–26, 28, 30, 31, 35, 36, 38, 39, 41–44, 46–52, 58–63, 65–71

CoD coefficient of determination. 5, 43, 46, 50

CSV comma-separated values. 5, 38

μCT micro CT. 5, 10, 17–20, 25, 26, 36, 42, 65, 67, 69

DRFO distal radius fracture osteosynthesis. 5, 36

DXA dual energy X-ray absorptiometry. 1, 2, 5, 10, 16–18, 41

FE finite element. 5, 42, 59

FGP full genetic potential. 5, 12, 13

FREEDOM fracture reduction evaluation of denosumab in osteoporosis every 6 months. 5, 41, 59

GoF goodness of fit. 5, 46

HAP hydroxyapatite. 5, 8, 10

HR-pQCT high resolution peripheral quantitative computed tomography. 1, 4, 5, 10, 16, 17, 19, 20, 24, 36, 41–43, 58, 59, 65–67, 70

KDE kernel density estimate. 5, 25–28, 36, 38, 46, 47, 59

MDMB mean degree of mineralization of bone. 5, 10

PBM peak bone mass. 5, 12–14, 35

PDF probability density function. 5, 20, 21, 25, 26, 28–30, 38, 48, 71

QCT quantitative computed tomography. 1, 2, 5, 10, 16, 17, 19, 41, 42, 59, 65, 68–70

ROI region of interest. 1, 2, 5, 11, 12, 19–22, 24, 38, 41, 42, 46, 58, 66–69

RSS residual sum squared. 5, 39–41, 46, 52–57, 69

SED strain energy density. 5

vBMD volumetric bone mineral density. 5, 10, 17

VE volume element. 5, 11, 12, 16, 20, 25, 26, 35, 38

VOI volume of interest. 5, 11, 12, 20–24, 31, 32, 38, 39, 58, 67, 69

Chapter 1

Introduction

1.1 Introduction

Bone is an interesting material. It is stable enough to withstand the forces of daily use but is lightweight and has the ability to repair itself at the same time. A lot of questions regarding bone are still open, despite enormous efforts to understand the biochemical and biomechanical mechanisms of bone. HUISKES et al. [43] framed the famous sentence "If bone is the answer, what is the question?". This describes the current knowledge quite well. It is clear that bone, just like every other tissue, must meet some functional requirements but is restricted in many ways. The current teaching says that bone is the most optimal structure which achieves all desired properties like lightweight design, stability, repairability and ability to adopt under the given restrictions: cells alone must be able to create and maintain the structure of bone during all stages of adolescence and adulthood. Certain mechanisms have been decoded over the years, but there is yet much to learn about bone.

Bone is a highly hierarchical, composite material consisting of water, organic and inorganic material with volume fractions of about a third each. The organic material consists mainly of collagen type I. The most common inorganic material is the calcium containing mineral hydroxyapatite (HAP). While the volume fractions are equal, the mass fractions are not. HAP accounts for approximately half the wet mass, while the organic mass fraction is about 32%.

Many pores of different size can be found in bone at a microscopic level. The pores pose some specific purposes, among one of them is the supply with nutrients and the ability to repair damaged tissue. The porous structure also allows sensing mechanical stimulation [51]. Two different parts of bone can be recognized when observing it on a larger scale: A dense and a more porous part. The dense bone, also known as cortical bone, can be found at outer surfaces which is referred to as the cortex. The porous bone, also known as trabecular or cancellous bone, can be found below the cortical surface. Figure 1.1 shows microscopic images of trabecular and cortical bone respectively. Long bones, like the femur or radius, also contain void space where only bone marrow can be found. The trabecular bone volume is also different to cortical bone, as it consists of small bone struts, called trabeculae, with a diameter of at most $400\,\mu\mathrm{m}$. The microstructure of trabecular bone is further divided into rods and plates [95]. Cortical bone on the other hand is much more dense but also has a microstructure. The main building block of cortical bone are called osteons. Osteons

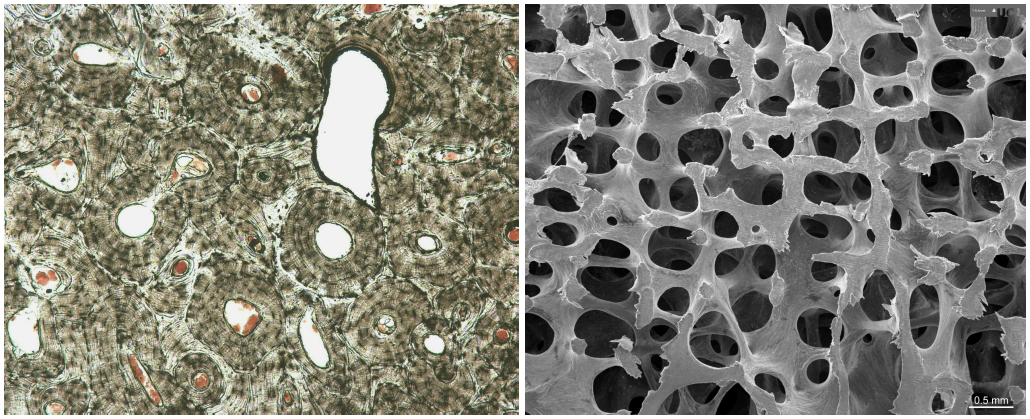

Figure 1.1: Left: Microscopic slice through cortical bone. Single osteons can be seen, as well as osteocytes inside the lamellae. Right: trabecular structure of the 3rd lumbar vertebra of a healthy 30 year old woman. Both images with kind permission of Prof Tim Arnett (`mailto:t.arnett@ucl.ac.uk`), via Bone Research Society (`http://www.brsoc.org.uk`).

have the form of concentric cylinders, with a pore in the middle. This pore is also known as Haversian channel and contains blood vessels. The bone cylinders show a microstructure like twisted plywood [34].

Different cells can be found inside bone. Three specific types of cells are found in bone and are regarded as bone cells. These cells have two different tasks: mechanical sensing and bone repair. Osteocytes are cells which are walled into the bone matrix and are believed to be responsible for sensing mechanical stimuli and orchestration of the other bone cells [5]. The osteocytes live within small caves, called lacunae, inside the bone and connects itself to other osteocytes via gap junctions at the end of their processes. The processes of the cells lie inside canaliculi, Latin for small channels. While there are many ideas how osteocytes sense mechanical stimuli, the exact mechanisms are still not known today [6]. The osteocyte itself does not form any bone tissue and is believed to have the role of a conductor. It orchestrates the two other cells: osteoblasts and osteoclasts. Osteoclasts derive from macrophages and have the purpose of resolving old bone matrix and digesting the degradation products [101]. Osteoblasts on the other hand can build up new bone material [56]. Some of the osteoblasts "stay behind" and differentiate into osteocytes, which are cemented into the bone matrix.

Bone is a living tissue and has the ability to reorganize itself over time. It is believed that bone adopts due to the sensation of mechanical stimuli. Those stimuli can originate from the muscle forces or external loads like during weight training. Just like muscles can be trained, also bone has the ability to increase its mass when loaded repeatedly. And just like muscles loose mass when not used, bone will also decrease in mass if it is not loaded properly. One example is space flight, where the astronauts loose bone in the femoral head twelve times faster than postmenopausal women on earth [11]. Special training is required in order to maintain the bone mass in space [2]. Another example is immobilisation after an accident or due to paralysis. Long time bed rest or immobilisation of limbs can have severe effects on bone mass. The time frame for changes in muscles and bone is different though. While training effects on muscles are seen within weeks, bone adaptation is seen only after several months.

The process of resolving and rebuilding bone matrix in an organized way is usually referred to as bone *remodelling cycle* or simply *remodelling* [49]. Another mechanism, under the name *modelling*, describes

the non-coordinated work of osteoclasts and osteoblasts and occurs usually in the non-mature bone and during fracture healing. In the literature is not always clear which term is meant and when observing a process on a certain temporal or spatial scale, both processes can be found to be active. Sometimes both processes are referred to as *bone adaptation* but also the term *(re)modelling* is used in the literature. In this work, the term *remodelling* is used as a synonym for bone adaptation.

A lot of different methods to investigate bone were invented over the last century. They range from classical X-ray, over computed tomography (CT) to dual energy X-ray absorptiometry (DXA) as well as quantitative computed tomography (QCT) and high resolution peripheral quantitative computed tomography (HR-pQCT). All these technologies use X-rays, but other technologies are used as well. The most common used ones are ultrasound [92], lasers [24] and magnetic resonance [32]. Today, DXA and less often QCT are used in the clinical practise, while HR-pQCT and other methods are usually used solely for clinical studies. A very important figure for clinicians is the bone mineral density (BMD). BMD can be measured in two different ways, either by using a 2D method like DXA and a resulting areal bone mineral density (aBMD) with the units $\mathrm{mgHA/cm^2}$ or by using a 3D method like CT which results in a volumetric bone mineral density (vBMD) with the unit $\mathrm{mgHA/cm^3}$. DXA and QCT do not measure the density of bone directly, but give the density of HAP inside the volume element. Both values correlate [23, 31, 57], but volume based approaches have more spatial information. This information might be of interest, as BMD differs in regions throughout bone [94].

If new bone tissue is created, a collagen matrix is created first which is mineralized afterwards. This mineralization requires some time, thus the bone is not fully mineralized immediately. At some point in time, the maximum mineralization level is reached. This value is also known as mean degree of mineralization of bone (MDMB). Once fully mineralized, it is similar in the whole bone and does not change much in ageing [86]. This means, that the main variation in ageing is porosity and not strictly speaking density. Another name for MDMB is $\mathrm{BMD_{max}}$. It can be derived from the density of pure HAP and the volume fraction in bone. The density of HAP is about $3160\,\mathrm{mg/cm^3}$, and the fraction by weight is about 50% and by volume about one third. Therefore, the theoretical maximum density of bone is about $2000\,\mathrm{mgHA/cm^3}$ But this theoretical value is not achieved in human bone. Fully mineralized bone has a density of about $1000\,\mathrm{mgHA/cm^3}$ to $1100\,\mathrm{mgHA/cm^3}$ while extremal values can range up to $1600\,\mathrm{mgHA/cm^3}$ [3]. These values are only measured at a micro scale.

Typical locations for assessment of BMD are the femoral head, distal radius, distal tibia and vertebrae. Also a full body BMD can be calculated when using DXA or QCT. Special QCT scanners exists, which only fit peripheral limbs like radius or tibia. Such devices are called peripheral-QCT. Ultimately, the smaller form factor of those devices lead to a higher resolution. These devices are then called HR-pQCT. The advantage of HR-pQCT is its resolution in the range of $30\,\mathrm{\mu m}$ to $80\,\mathrm{\mu m}$. The duration inside the tomograph needs to be limited for *in-vivo* scans in order to reduce the exposure to X-rays for the patient. This can be achieved either by a lower resolution or limited scan size.

But not only BMD is of interest, also other figures can be calculated from the images. The field of bone histomorphometry knows over forty different figures which can be calculated for both cortical and trabecular bone [19, 76]. The first histomorphometrical figures were created using histological cuts of bone. Bone slices were prepared, cut and polished and then observed under an optical microscope. Today it is possible to create the same figures using 3D imaging techniques and image processing algorithms [69,

73]. Using 3D based image processing has the advantage of being non-destructive. It is also possible to generate each figure for several volume element (VE) while a classical histomorphometrical approach is limited to the number of histological slices which are taken from a bone sample.

Image processing can also be used for various other tasks like image segmentation and image separation. The process of image segmentation on bone images tries to differentiate areas of bone versus areas of non-bone tissue. This could be bone marrow, surrounding soft tissue, water or other materials like bone screws. The segmented image contains three types of voxels: voxel which code for bone (bone volume), voxels which code for marrow and voxels code for neither of both (zero volume). The information about the zero volume can also be separated from the segmented image and be part of an additional mask. Figure 1.2 shows a single VE with segmented and masked data and how the terms apply in this image. Image separation however tries to identify structural differences in the same tissue. For example, the cortical shell can be separated from the trabecular core.

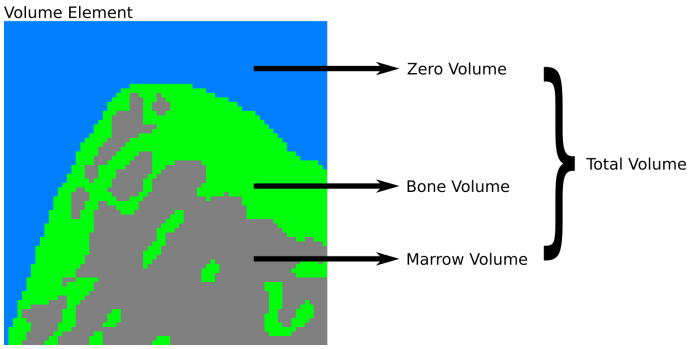

Figure 1.2: Definitions of voxel types inside a VE for a segmented image. All voxels which do not belong to the bone itself are coded as "zero volume". Two types of voxels can be found inside the bone: actual bone and marrow. All volumes together form the total volume, which is the same as the size of the volume element.

Properties of bone are not the same in every bone of the human body and also vary inside each bone. It is required to standardise the measurements in order to compare measured quantities. Using the same regions of bone is one method for standardisation. Such a region is also referred to as region of interest (ROI) and can be defined either by a fixed position or anatomical landmarks. The total volume of a ROI is not necessarily the same for each individual, as relative positions are possible. Such volumes can be normalised by size to get comparable results. A ROI can contain a number of VEs or volume of interest (VOI). Both terms can be used interchangeably. If image separation is applied to a ROI, histomorphometrical figures can also be given for trabecular and cortical bone individually.

Two measures are of special interest in this work: BVTV and BSTV. BVTV gives the ratio of actual bone volume and total volume, while BSTV gives the ratio of total surface area and total volume. It is important to specify what exactly the total volume is. Different definitions of the total volume are possible, depending on the question. A *global*, *overall* or *total* BVTV can be calculated if the total volume is the ROI. Total BVTV is called $\mathrm{BVTV}_{\mathrm{tot}}$. The names $\mathrm{BVTV}_{\mathrm{tb}}$ and $\mathrm{BVTV}_{\mathrm{ctx}}$ are used if only trabecular or cortical bone is involved in the calculation. The same notation is used for BSTV as well. These two figures are usually calculated for 3D volumes, but 2D analogue exists. BVTV is then called bone area over total area (B.Ar.T.Ar.) and BSTV becomes bone perimeter over total area (B.Pm.T.Ar.). But these terms are rarely

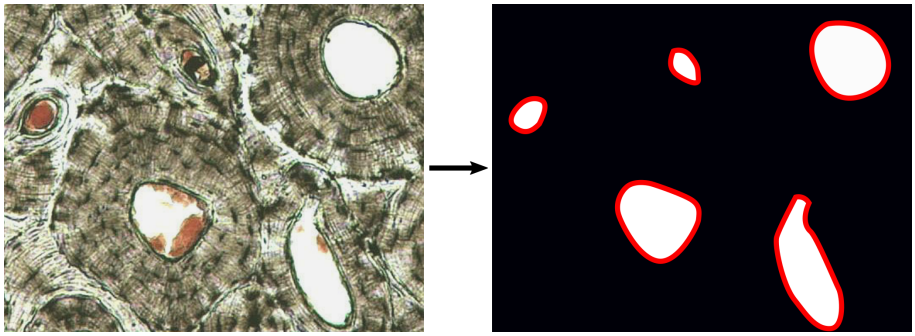

Figure 1.3: Calculation of BVTV and BSTV in 2D. First, the VOI (here area of interest) is masked. In the right image, black codes for bone, while white codes for non-bone areas. BVTV is then calculated as the fraction of black area to the total area. In this image, the value for BVTV is about 89%. To compute BSTV, the total perimeter (red) of pores is measured and divided by the total area. In this case the value for BSTV is around $0.037/\mathrm{mm}$. The exact calculation of both values depends on the resolution and therefore the number of small pores that are correctly imaged. Beside the larger pores in this image, smaller pores like canaliculi cannot be seen in this image. Therefore, the total BSTV might be higher and BVTV lower if all small pores would be added.

used. To illustrate both BVTV and BSTV, a 2D representation is shown in figure 1.3. Instead of calculating the total BVTV or BSTV, a *local* BVTV or BSTV can be calculated as well. Many VEs are placed inside a single ROI. Each VE is now used to calculate an individual value, resulting in many BVTV or BSTV values for a ROI. There are different methods how such VEs can be created and placed inside a ROI.

As bone changes during a lifetime, also the properties and figures describing bone are changing. The most interesting parameter for clinicians is BMD. The changes during a lifetime of BMD are well investigated and many different studies were performed and are still conducted on the topic of BMD changes. During adolescence the BMD increases up to a point where a maximum BMD is reached. This point is usually referred to as peak bone mass (PBM). PBM itself is correlated with different anthropometric figures, like body weight or body height [59]. This is not surprising as a larger body should also have stronger bones. There might be other factors which lead to PBM though, like nutritions, sport or diseases and several biochemical markers [36]. Also ethnics and origin play a role when PBM is reached [109].

In theory there is a set of factors which lead to an optimal, thus maximum, PBM. The term full genetic potential (FGP) describes this theoretical value, which is the maximal BMD for a living being [39]. Figure 1.4 shows the progress of the BMD curve over a lifetime. In this idealized figure, the FGP describes a bone mass which is build up during adolescence and never lost if PBM is reached. Ageing is regarded as a negative effect on bone mass in this model. PBM might be one of the crucial figures for BMD in later age [39] as BMD decreases after the peak is reached. It is thought, that the BMD over a lifetime curve can be modified for example by training, extra nutrition or medication in a positive way [40, 85] or by diseases in a negative way. Also PBM might be influenced if such a modification are started very early in life. It is also thought that the process of decreasing BMD after the peak is programmed into the cells, just like other ageing effects which are commonly seen in old people like creases of the skin. This would means, that a person with a very high PBM has a lower chance to develop osteoporosis in ageing. But the topic is controversial. In experiments with young rabbits, the bone mass decreased after an intervention using os-

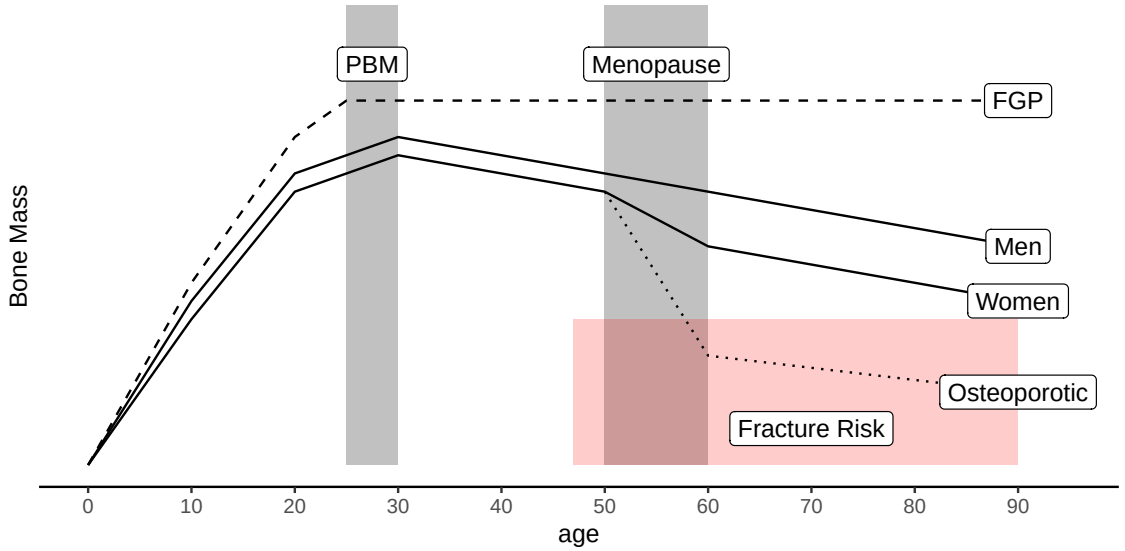

Figure 1.4: Schematic curve of BMD over a lifetime. The dashed line gives the theoretical FGP curve, which can only be reached if all factors for bone mass would be regulated perfectly. Such a curve is not observed in reality. Men usually do not have a period of increased bone loss and also have a higher PBM than women. The dotted curve describes a severe bone loss during menopause resulting in osteoporosis. The red region indicates values of bone mass which lead to an increased risk for fractures.

teoporosis inducing substances but reached the same level as the control group shortly after the intervention stopped [30]. This lead to the question if short term interventions, for example in the childhood, can be used to improve the situation in ageing. The results from that study showed, that the determination of PBM might not be influenced via external factors but determined by a genetic program which is hard to override. This genetic program can be overwritten though if enough "force" is applied. Excessive training or medication do have some effect on bone mass. But the system slowly finds its way back to the homoeostatic state if the stimulus is removed. In the study of WASNICH et al. [107], postmenopausal women received medication against BMD loss in the form of either alendronate or oestrogen/progestin. The medication was withdrawn and changed to a placebo after four years and the patients were monitored for a total of seven years. BMD values were constantly increasing during medication, but they dropped with a much higher rate than the control group after withdrawal for the oestrogen/progestin group. The rates in the alendronate group were comparable to the control group, but longer monitoring of the patients would be necessary to show if the treated patients would eventually reach the same level as the untreated control group after several years. This question could only be answered by long term studies, which are currently not available to the author's knowledge.

BMD loss per year is described as a percentage of PBM in many cases, as it is thought that bone mass will continuously decrease after PBM is reached. Therefore, the rate can then be normalized to PBM. For example, typical values are 0.25% PBM/a and three to four time that during menopause [40]. Other studies yielded 1.08% BMD/a for women and 0.54% BMD/a for men at the distal radius [10]. Menopausal changes are not observed in all studies as the rates during ageing are constant [67]. It was shown, that the loss rates

are different in four phases of menopause though [27]. Thus, the method of gathering rates for specific parameters is crucial here. For example, it might be required to observe the rate beginning with the start of menopause instead of using age matched groups.

Not only the BMD is changing during ageing, also geometry and microstructure is affected as well. Contradictory to the decreasing BMD, the diameter of bones is increasing in age [18]. The trabecular bone volume as well as the trabecular size decreases while trabecular spacing increases [13, 15, 60, 75]. Also the cortex is affected and shows increased porosity [60], even a change in the distribution can be observed [66]. The cortical volume over total volume increases [12] while the cortical thickness is decreasing [97]. Those changes are not only dependant on age but also on the specific bone, the location inside the bone and are also sex-specific [21].

Additionally to the age related changes in BMD, there are also disease related changes. One of the most common bone diseases worldwide is osteoporosis. About 30% of all women after the menopause are affected by osteoporosis, which makes osteoporosis not only a serious disease but also a common phenomena of ageing. It is known, that oestrogen deficiency is causing bone loss which is increasing the effect of ageing too [80]. But not only women suffer from osteoporosis. Immobilised bone can get osteoporotic, which is known as disuse osteoporosis [108]. This is usually the case if bone is not stimulated enough, for example by regular walking. Results of prolonged immobilisation are higher calcium excretion [22] and therefore muscle and bone atrophy [84]. Osteoporotic bone shows other figures than healthy bone. An osteoporotic bone has a higher number of pores and thinner cortices than healthy bone [72]. These changes can also be seen in an decreased BMD. Several models exists to evaluate the changes due to ageing and diseases. The effects of immobilisation are investigated on humans using bed rest studies [53] or in animal models for example by limb unloading [68].

Using the knowledge about the normal changes of BMD during ageing lead to the invention of a simple system to monitor a patient's osteoporosis status, called t-score. The t-score is the number of standard deviations of which a measured BMD is off the average PBM. Thresholds are defined at which a bone is regarded as healthy, osteopenic or osteoporotic [71]. The t-score has the disadvantage to classify too many elderly people as osteoporotic, where in fact their bones are healthy. It is also known that the reference BMD values vary depending on the population [47]. Therefore, reference measurements need to be taken for each population. Another reference value can be used instead in order to improve the diagnosis. The new method is called z-score and uses age matched healthy populations for the comparison of BMD. But both t- and z-score fail in some cases to detect a risk of fracture. This poses a high risk for patients.

In order to overcome these limitations better risk assessment tools were created. FRAX is one of the most commonly used tools at the moment [46]. Also a new term called *bone quality* was created, which measures not only the quantitative figures like BMD but also qualitative figures like structural parameters [65].

The changes of bone due to ageing, immobilisation or diseases are reported in various studies. But the ultimate goal is to understand the root cause and mechanism of bone remodelling. Models can help clinicians in order to predict changes of bone. Theoretical models were created in order to investigate properties of bone under adaptation. Such models are usually referred to as *bone remodelling models*. Those models are often used to investigate the changes due to mechanical stimuli. The roots of bone remodelling research began probably with the work of Julius Wolff [63] and Wilhelm Roux, who formulated independently from

each other laws on bone adaptation at the begin of the twentieth century. Years later, Harold Frost formulated the Mechanostat theory, which explains the bone adaptation by mechanical stimuli [28]. Since then, many different models for bone remodelling were created. Those models, usually quite different in their approach, can nevertheless be ordered into two groups: phenomenological and mechanobiological. While the first group of models tries to explain the remodelling only based on empirical data, the latter try to explain the behaviour in terms of cell activity or even biochemical processes. When referring to the size of bone elements that are used in the model, yet another distinction can be made. Microscopic models work in the spatial range of single pores or trabeculae, while macroscopic models try to get a more abstract view and work with larger volume elements, even in the range of mm. Both types have their advantages, as for example microscopic models have the ability to show remodelling processes very precise for small parts of bone, while macroscopic models lack this precision but can be used to model the behaviour of a whole bone at once. Such models are not only of importance to understand the mechanisms in bone remodelling but also to predict bone changes in patients. They might predict if a patient will develop osteoporosis at a stage, where countermeasures can still be applied.

1.2 State of the Art

1.2.1 Mean Values and Rates for Age Related Changes of Bone

Many population based studies were performed since the first DXA and QCT devices were available. Such studies are conducted for specific devices as well as for specific populations. Usually the age related change of BMD is recorded, but also other histomorphometrical figures are used.

DXA based studies usually use the hip, especially the proximal femur, the lumbar spine and in some cases the distal forearm. The same bones are imaged when QCT is used, but only peripheral bones like the distal forearm or distal lower leg are used in peripheral-QCT.

A selected list of population based studies is given in table 1.1. Additionally the mean BMD and age rates for studies examining the radius are given in table 1.2. Age related rates are usually not given directly in the studies. They are calculated from the mean data of the age groups. A list of QCT based studies can be found in ENGELKE et al. [26] while HR-pQCT studies can be found in RIETBERGEN et al. [81].

1.2.2 Models for BSTV

Bone remodelling can only occur at surfaces and not inside the dense bone matrix [37]. The surface available inside a VE can be expressed as BSTV. But remodelling models usually only use the density of a VE as a parameter for the intensity of remodelling. Therefore, it is required to find a relationship between the density of a volume element, expressed as BVTV for the surface available, BSTV.

Such models were constructed in the past with the aid of histological specimens and curve fitting. The first model was created by MARTIN [64]. It uses a polynomial of fifth degree and bone porosity $P = 1 - \mathrm{BVTV}$:

$$\mathrm{BSTV} = 32.2\,P - 93.9\,P^2 + 134\,P^3 - 101\,P^4 + 28.8\,P^5 \tag{1.1}$$

Another model was created by LEREBOURS et al. [54]. A square root model is used, with two parameters a and b which need to be fitted on the data:

$$\mathrm{BSTV} = a\,\sqrt{1 - \mathrm{BVTV}}\;b\,\mathrm{BVTV} + 1 - b \tag{1.2}$$

The square root model is similar to the one of FYHRIE et al. [29].

These models can be used in remodelling models to scale the current activity inside a VE proportional to the available surface. Even if only the density of the VE is known.

Study	Method	Location	Population
RIGGS et al. [83]	DXA	proximal femur	US
LOOKER et al. [58]	DXA	proximal femur	US
WARMING et al. [106]	DXA	distal forearm, hip, lumbar spine	Danish
LEUNG et al. [55]	DXA	Femur	Chinese
MAKKER et al. [62]	DXA	Hip, Lumbar spine, Forearm	Indian
BUTZ et al. [10]	QCT	forearm	German
TSUZUKU et al. [98]	QCT	distal radius	Japanese
DJURIC et al. [21]	μCT	Femur	Serbian
HAYASHI et al. [38]	HR-pQCT	Vertebrae	Japanese
HUNG et al. [44]	QCT	Radius, Tibia	Chinese

Table 1.1: A selection of age specific BMD reference studies. The typical anatomical sites for measuring vBMD or aBMD are proximal femur, distal radius (or forearm), distal tibia and vertebrae. Data is available for different populations using different measurement techniques.

DXA based studies		
Variable	Value	Age Range
MAKKER et al. [62]	Radius 33%	
Male		
Rate	$0.0068\,\mathrm{gHA/cm^2/a}$	65 - 77
Mean	$0.796\,\mathrm{gHA/cm^2}$	71 - 83
Female		
Rate	$0.0063\,\mathrm{gHA/cm^2/a}$	65 - 78.5
Mean	$0.583\,\mathrm{gHA/cm^2}$	71 - 86
WARMING et al. [106]	Distal Radius	
Male		
Rate	$0.003\,\mathrm{gHA/cm^2/a}$	50 - 80
Mean	$0.47\,\mathrm{gHA/cm^2}$	70 - 89
Female		
Rate	$0.005\,\mathrm{gHA/cm^2/a}$	50 - 80
Mean	$0.33\,\mathrm{gHA/cm^2}$	70 - 89

CT based studies		
Variable	Value	Age Range
TSUZUKU et al. [98]	Distal Radius (D100)	
Male		
Rate	$4.76\,\mathrm{mgHA/cm^3/a}$	60 - 79
Mean	$489.5\,\mathrm{mgHA/cm^3}$	70 - 79
Female		
Rate	$3.32\,\mathrm{mgHA/cm^3/a}$	60 - 79
Mean	$392.5\,\mathrm{mgHA/cm^3}$	70 - 79
HUNG et al. [44]	Distal Radius	
Female		
Rate	$2.09\,\mathrm{mgHA/cm^3/a}$	20 - 89
Mean	$385.8\,\mathrm{mgHA/cm^3}$	20 - 29

Table 1.2: Rates and mean values from existing studies for both DXA and CT based studies at the radius. Values as specified in each publication. The age range gives the range for which the parameter is given. The study of HUNG et al. [44] also gives separate rates for $\mathrm{BMD_{tb}}$ and $\mathrm{BMD_{ctx}}$.

1.3 Thesis Goals

Changing bone mass is usually described by a single parameter, BMD or BVTV. These values are used in clinics as a marker for certain bone diseases. Such values are usually calculated over a single ROI. But such a mean value does not reflect the inhomogeneity and the bone's morphology. Many different changes are observed in bone, which can probably not measured by a single value alone. The limitations of the "single parameter method" can be seen at the example of t-scores. Sometimes the method fails to detect osteoporosis or osteoporosis is diagnosed on healthy bones. Better diagnosis tools are required, which do not require extra effort of the patients. It is hypothesised that a distribution of this parameter contains more information about the changes and thus is able to explain changes in bone better. Such a distribution can easily be created from existing CT data, thus does not require any effort of the patient at all, as the data is already collected. The research question was formulated as: Does a distribution of local bone densities gives more information about the age, sex or treatment related changes than a simple mean value alone?

Distributions of BVTV are examined in this work to answer the hypothesis and the following research objectives were formulated:

1. to investigate the BVTV distribution at the radius using HR-pQCT data.
2. to investigate the age related changes in BVTV in those distributions.

Also the following sub-objectives were formulated:

3. to determine if changes in the distribution are also visible using QCT data.
4. to find out whether the age related changes can be explained by a simple geometrical model for BVTV and a rate based remodelling law.

This work was intended as a pilot study in order to identify possible new diagnosis measures without additional harm to a patient.

Chapter 2

Material and Method

2.1 Distributions of BVTV in Bone

The usual approach to investigate a patient's osteoporosis status is by using a single value like the mean BMD inside a specific bone. When using 3D imaging technologies like HR-pQCT, it is possible to get distributions of such values for a number of VOI inside a ROI. Figure 2.1 shows how these volumes are defined on a CT scan. VOI can also be referred to as VE, averaging volume, rasterisation volume or scan window.

Such distribution curves can be computed for BVTV. The distribution should be given in a normalized form, in order to simplify the equation. In this case $f_{\mathrm{BVTV}}(x)$ gives the relative frequency for a BVTV value $x \in [0, 1]$ for the VEs inside the ROI. It then forms a PDF, which has the property that the area under the curve is equal to one:

$$\int_0^1 f_{\mathrm{BVTV}}(x)\, dx = 1 \tag{2.1}$$

Next, the mean (expected value) of the distribution can be calculated by weighting the relative frequencies by the BVTV value. This gives then the mean BVTV inside the ROI, $\mathrm{BVTV}_{\mathrm{tot}}$.

$$\mathrm{BVTV}_{\mathrm{tot}} = \int_0^1 x\, f_{\mathrm{BVTV}}(x)\, dx \tag{2.2}$$

The shape of the distribution is influenced by the choice of parameters for ROI and VOI. Shape and size of VOI will change the distribution. It is possible to use any kind of shape for the VOI, like spheres or irregular shapes, but regular shapes like rectangles are less computing intensive, as 3D images are usually constructed from rectangular shapes as well. The shapes might be defined as overlapping or adjacent. Each volume will contain information of the neighbouring volumes if overlapping shapes are used. Overlapping has a smoothing effect on the distribution. VOI are regarded as adjacent cubes in the following sections.

The size of the volume, i.e. the edge length of the cube influences the distribution as well. The effect of different volume element size can be seen in figure 2.3. The smaller the volume size is, the further away are the two peaks of the distribution. For the very small volume element size of $0.5\,\mathrm{mm}$, the distribution

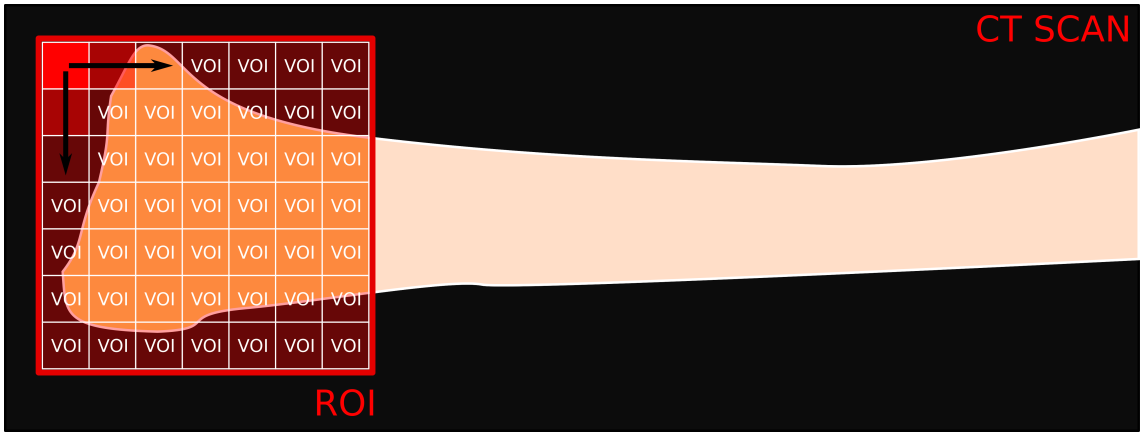

Figure 2.1: Definition of ROI and VOI at the example of a radius CT scan. The ROI defines a region inside the CT scan which is used for further analysis. In this example the distal part of the radius was selected as ROI. Inside the ROI, many VOI are used to calculate certain values, for example the BVTV. In this case cubic and adjacent VOI are used.

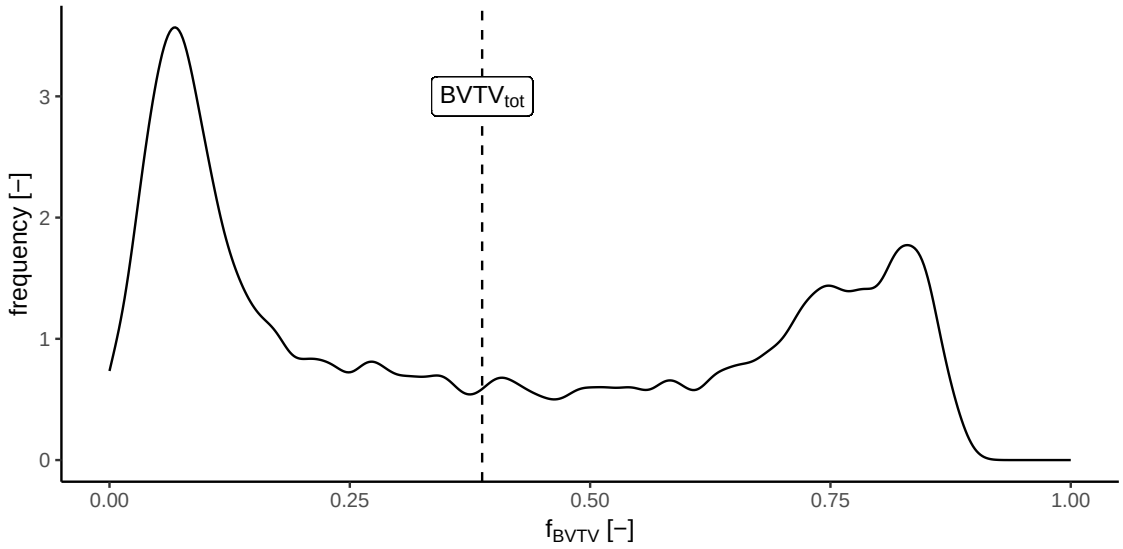

Figure 2.2: A PDF of BVTV. The mean value (dashed line) corresponds to $\mathrm{BVTV_{tot}}$

.

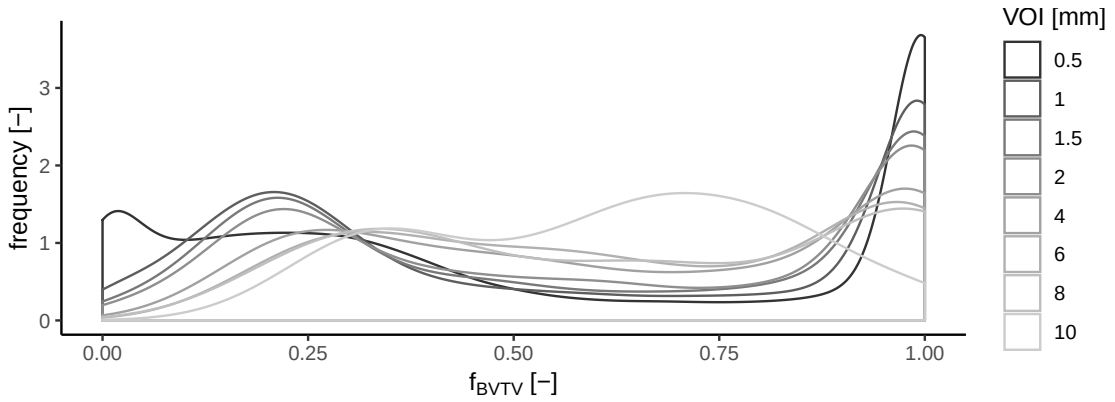

Figure 2.3: Dependency of VOI size to the BVTV density curve. The larger the cube size is set, the more the two distributions come to the middle of the range.

shows a pronounced peak at one and a smaller peak close to zero as well as a second peak close to 0.25. The largest volume element with an edge length of $10\,\mathrm{mm}$ shows two peak, one close to 0.75 and the other one close to 0.4.

Using a too small volume element results in a distribution, where large parts are at the extremal values, zero and one. On the other hand, choosing a too large volume element size results in a averaged distribution, with the extremal case that only a single VOI is inside the ROI. The resulting curve will be a Dirac distribution at $\mathrm{BVTV}_{\mathrm{tot}}$.

There are at least two different ways to extract the BVTV from an image. Either by using the BMD coded grey-values or by using image segmentation. Both methods pose different challenges and will result in different distributions in the general case.

Using image segmentation results in a very easy relationship for BVTV. Only the bone volume BV, total volume TV and zero volume ZV must be known. The resulting equation for BVTV is given in equation 2.3, an example how this extraction process looks graphically is shown in figure 2.4.

$$\mathrm{BVTV}_{\mathrm{tot}} = \frac{\mathrm{BV}_{\mathrm{tot}}}{\mathrm{TV}_{\mathrm{tot}} - \mathrm{ZV}} = \frac{\text{number of bone volume voxels}}{\text{number of voxels} - \text{zero volume voxels}} \tag{2.3}$$

Using the BMD is not much more difficult. There is only one prerequisite: It is required to have voxels with calibrated BMD as grey-value. Then the BVTV of a volume element can be defined as given in equation 2.4. A zero volume must be considered like in the segmentation approach, which is up to the implementation of the calculation of $\mathrm{BMD}_{\mathrm{tot}}$.

$$\mathrm{BVTV}_{\mathrm{tot}} = \frac{\mathrm{BMD}_{\mathrm{tot}}}{\mathrm{BMD}_{\mathrm{max}}} \tag{2.4}$$

For this relationship to hold, reasonable values for $\mathrm{BMD}_{\mathrm{max}}$ are required. $\mathrm{BVTV}_{\mathrm{tot}}$ values larger than one can occur if $\mathrm{BMD}_{\mathrm{max}}$ is set too low. Typical values for $\mathrm{BMD}_{\mathrm{max}}$ are $1200\,\mathrm{mgHA/cm^3}$ [61] [90] or $1400\,\mathrm{mgHA/cm^3}$ [17]. The segmentation method will never produce BVTV values larger than one.

Separate values for trabecular ($\mathrm{BVTV}_{\mathrm{tb}}$) and cortical bone ($\mathrm{BVTV}_{\mathrm{ctx}}$) can be calculated instead of $\mathrm{BVTV}_{\mathrm{tot}}$. Equations 2.3 and 2.4 needs to be adopted to use only the trabecular or cortical volumes.

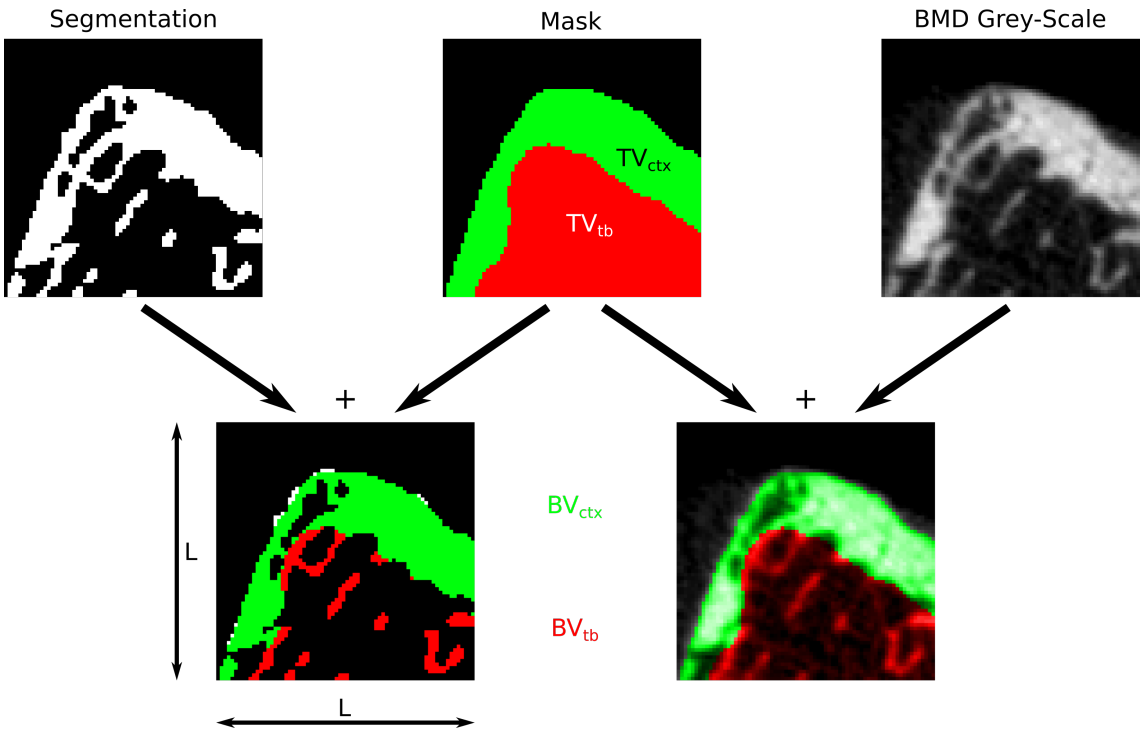

Figure 2.4: Extraction process from a VOI to get BVTV, schematically shown for an area instead of a volume. The VOI size is L^2. Input images are the segmentation, masks from separation and BMD scaled image. $\mathrm{TV}_{\mathrm{ctx}}$ and $\mathrm{TV}_{\mathrm{tb}}$ can be calculated from the mask directly. The results are: $\mathrm{TV}_{\mathrm{ctx}} = 0.266\,L^2$ and $\mathrm{TV}_{\mathrm{tb}} = 0.36\,L^2$. $\mathrm{BV}_{\mathrm{ctx}}$ and $\mathrm{BV}_{\mathrm{tb}}$ is calculated from segmentation and mask together or from the BMD scaled image and the mask. For the segmentation, the results are: $\mathrm{BV}_{\mathrm{ctx}} = 0.219\,L^2$ and $\mathrm{BV}_{\mathrm{tb}} = 0.06, L^2$. BVTV can be calculated as $\frac{\mathrm{BV}}{\mathrm{TV}}$ and result in $\mathrm{BVTV}_{\mathrm{ctx}} = 0.823$ and $\mathrm{BVTV}_{\mathrm{tb}} = 0.168$ while $\mathrm{BVTV}_{\mathrm{tot}} = 0.446$. The BMD scaled image can be used as well and results in an average $\mathrm{BMD}_{\mathrm{ctx}} = 0.604\,\mathrm{BMD}_{\mathrm{max}}$ and $\mathrm{BMD}_{\mathrm{tb}} = 0.142\,\mathrm{BMD}_{\mathrm{max}}$. In order to calculate BVTV from BMD, a specific value for $\mathrm{BMD}_{\mathrm{max}}$ must be used.

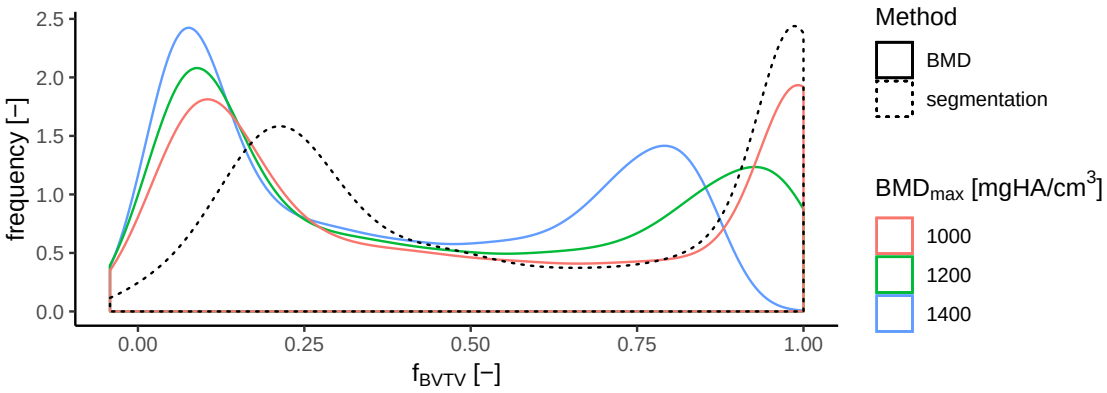

Figure 2.5: Difference in density curves for BMD and segmentation extraction method. A HR-pQCT image of the radius with an isotropic voxel size of $82\,\mu\mathrm{m}$ was used. The whole image was used as ROI. Three different values for $\mathrm{BMD}_{\mathrm{max}}$ are given. In order to not allow BVTV values larger than one, such values were limited to one for both $1000\,\mathrm{mgHA/cm^3}$ and $1200\,\mathrm{mgHA/cm^3}$. As the maximum BMD value in the image was limited to $1400\,\mathrm{mgHA/cm^3}$, a clipping is not necessary for this curve. The VOI size was set to $1.5\,\mathrm{mm}$ (rounded to the next voxel dimension).

Both methods were applied to a HR-pQCT scan of the radius. The whole scanned segment was used as a ROI, while adjacent cubes with side length of $1.5\,\mathrm{mm}$ were used to calculate the distribution. Both distributions can be see in figure 2.5. It can be seen, that the segmentation approach favours higher values, while the BMD approach had virtually no higher values than 0.95 in the case of $\mathrm{BMD}_{\mathrm{max}}$ set to $1400\,\mathrm{mgHA/cm^3}$. The curves, especially in the higher BVTV region are getting more and more similar if the value for $\mathrm{BMD}_{\mathrm{max}}$ is lowered. This behaviour can be explained, as no BVTV values larger than one are allowed. Therefore, the resulting BVTV is clipped at this point. The image data contained values with a maximum BMD of $1400\,\mathrm{mgHA/cm^3}$, therefore no values need to be clipped.

The lower BVTV region, on the other hand, is reaching much closer to zero when using the BMD approach. This behaviour can be explained as in the CT data, there are virtually no voxels with a true value of zero, as the image has a lot of noise in it. That means, that due to the noise, empty space will almost always contain some voxel which are larger than zero and thus the distribution of the lower values is broader.

A systematic difference can be seen in the residual plot, when only looking at the differences between $\mathrm{BMD}_{\mathrm{max}}$ of $1400\,\mathrm{mgHA/cm^3}$ and the segmentation method. These residuals along the z-axis of the scan when subtracting segmentation results from BMD method results are shown in figure 2.6. This systematic difference can be reduced if a lower value for $\mathrm{BMD}_{\mathrm{max}}$ is chosen, as seen in figure 2.5.

When using the segmentation method, the results look much “cleaner”, as noise as well as some information is removed from the image in the segmentation process. While the distribution of trabecular bone benefits from the noise reduction, the cortical bone distribution is forfeited as information is lost. Small pores and channels are not visible in the segmented image, while BMD values can still describe the micro-porosity. For this reason, the majority of the cortical distribution is near to or exactly 100% BVTV. Throughout this work, the segmentation method was used to determine BVTV values if not otherwise noted. The BMD method is susceptible for noise in the image, which can elegantly removed by segmentation.

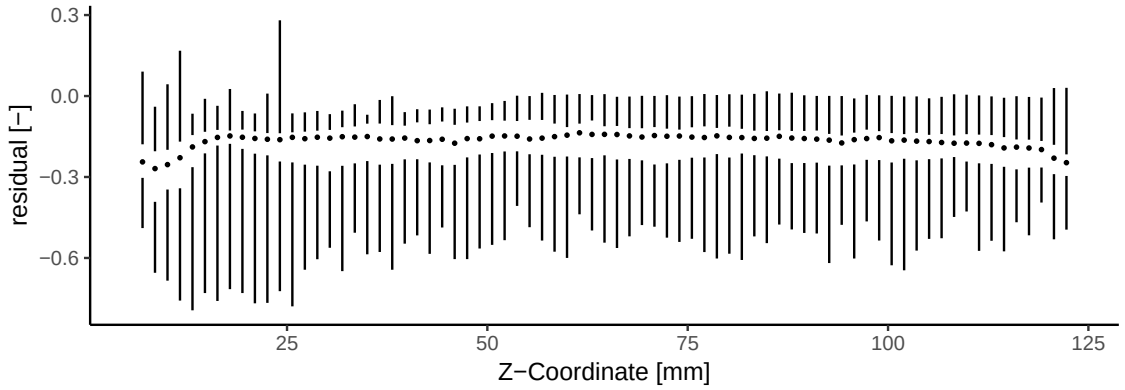

Figure 2.6: Residuals of BMD and segmentation method. The BVTV calculated by the BMD method was subtracted from the result of the segmentation method. A systematic error can be clearly seen, as all values are rather shifted towards the negative. The boxplots are shown for each Z-coordinate from distal to proximal. It can be seen, that the first and last slices have higher residuals while the residuals in the other slices are relatively the same.

2.2 Reducing Variables Using Curve Fitting

Frequency distributions are usually presented as a histogram. The BVTV distributions are calculated for each possible BVTV value, which results in a high number of variables. There are exactly k possible BVTV values when using the segmentation method, where k is the number of voxels inside a VE. This representation is the same as a histogram with k bins. k is usually much larger than 1000, as a single voxel has an edge length of $82\,\mu\mathrm{m}$ and the overall VE size is in the range of $1.5\,\mathrm{mm}$.

One way of reducing the number of variables used, is by describing the data using an analytically defined PDF. This PDF might have several components itself and the exact function must be found using a theoretical model. Curve fitting algorithms can then be used to fit such a PDF to the data. In fact, this reduces the number of variables significantly. Using such a model has a convenient side effect: If the model's parameters are chosen carefully, they will have a physical meaning. The frequency distribution itself does not have such parameters. The process of describing a BVTV frequency distribution by a theoretical PDF is shown in figure 2.7. First, the frequency distribution is created from CT images, then a kernel density estimate (KDE) is applied to the frequency distribution. A overall PDF is constructed from several PDFs and finally the overall PDF is fitted to the density distribution, revealing the parameters of the model. The next chapters explain the process and its components in more detail.

1. Construct frequency distribution from CT image

$n = 6859$ variables

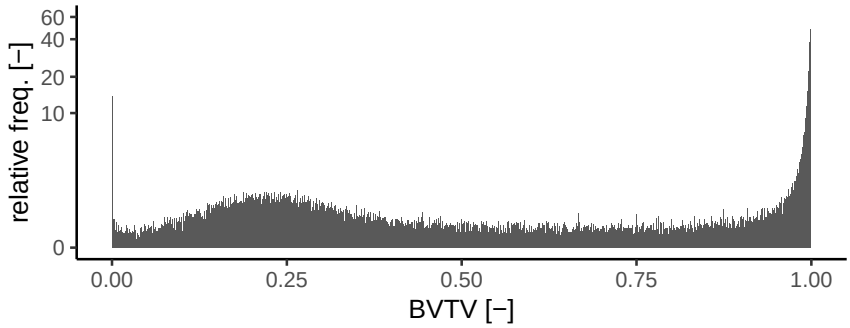

2. Smooth frequency distribution

$n + 2$ variables

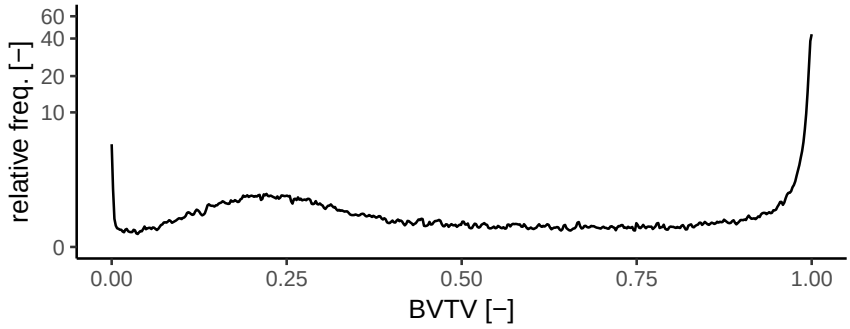

3. Fit PDF for overall BVTV

$k = 10$ variables

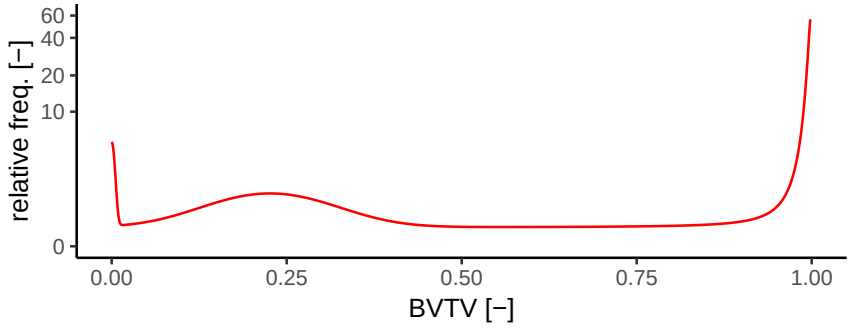

Figure 2.7: Process of reducing the variables from a frequency distribution. First, the frequency distribution contains many variables. In this case $n = 19^3 = 6859$, which is the number of voxels in the VE. For better visual clarity, the histogram shows 512 bins instead of all variables. Next, a KDE is applied to the frequency distribution in order to smooth it. This adds two additional variables, one for the bandwidth and one for the kernel in use. In the last step a theoretical model is fitted, which reduces the number of variables to $k = 10$.

2.3 Kernel Density Estimates

KDEs, as their name suggest, can be used to estimate a density function from a random sample. A KDE can be constructed using different kernels and a bandwidth parameter. This estimation has the advantage, that intermediate values can be calculated from the KDE.

The KDE makes use of a smoothing kernel, which is applied for each sample point. The Gauss kernel is used in this work exclusively. The function of the kernel is given in equation 2.5.

$$k(t) = \frac{1}{\sqrt{2\pi}} \exp\left(-\frac{1}{2}t^2\right) \tag{2.5}$$

From a random sample $x_1, \ldots, x_n$ and the bandwidth parameter $h > 0$, the KDE function $d(t)$ is defined as:

$$d(t) = \frac{1}{nh} \sum_{j=1}^{n} k\left(\frac{t - x_j}{h}\right) \tag{2.6}$$

An example of a KDE for a random sample is given in figure 2.8. Five samples are drawn from a standard normal distribution. Then the Gaussian kernels are calculated for each sample, which are then summed to form the KDE. Using a different bandwidth parameter results in a different curve. The lower bandwidth parameter gives a more detailed curve. But the bandwidth parameter could be chosen too low, which results in a curve which does not estimate the actual distribution. Different methods are available to select a proper bandwidth. One method is to use bandwidth estimators, like the *SJ* algorithm [91].

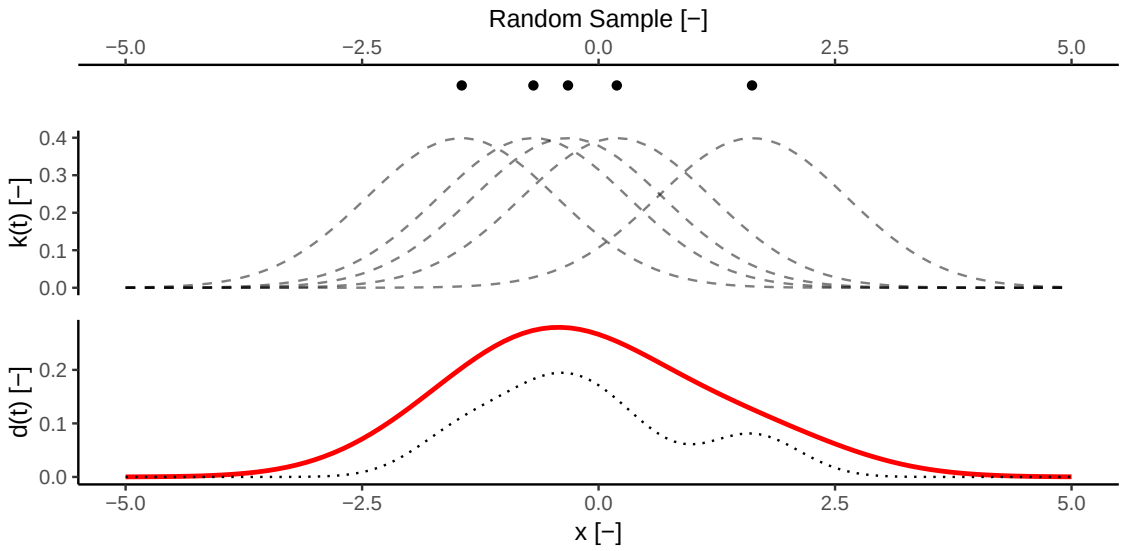

Figure 2.8: KDE from a random sample of size 5. Shown are the Gauss kernels as dashed lines for each of the samples as well as the resulting KDE. The red line uses a bandwidth parameter of $h = 1$, while the dotted line uses a bandwidth parameter of $h = 0.5$. The lower the bandwidth parameter, the more details can be seen in the resulting curve. Using a higher bandwidth results in a smoother curve.

2.4 Distributions for Special Purposes

The KDE gives a smooth function but has still the disadvantage of depending on all the variables of the BVTV frequency distribution. But statistical samples, like the frequency distribution, can often be described by their originating PDF. For example, a random sample stemming from a normal distribution can easily be described by two parameters: The mean μ and standard deviation σ.

While the normal distribution can be used at many occasions, especially for data which stems from natural origins, it fails to describe certain datasets. Sometimes the samples show an asymmetric form, i.e. the samples show a tendency to one side of the distribution. Other samples show a lot more "extremal" values than the normal distribution. Sometimes a distribution is required where the tails do not decay that fast. Such a distribution is also called "heavy-tailed". Two distributions which allow the description of non-normal distributed data are presented here. The first one is the skewed normal distribution, which can be used to described asymmetric data, while the Cauchy distribution can be used for heavy-tailed data.

The skewed normal distribution N_{sk} is a derivate of the normal distribution. It is described by three parameters: ξ, ω and α [1]. The PDF for the skewed normal distribution can be given as:

$$f(x) = \frac{2}{\omega\sqrt{2\pi}} e^{-\frac{(x-\xi)^2}{2\omega^2}} \int_{-\infty}^{\alpha\left(\frac{x-\xi}{\omega}\right)} \frac{1}{\sqrt{2\pi}} e^{-\frac{t^2}{2}}\, dt \tag{2.7}$$

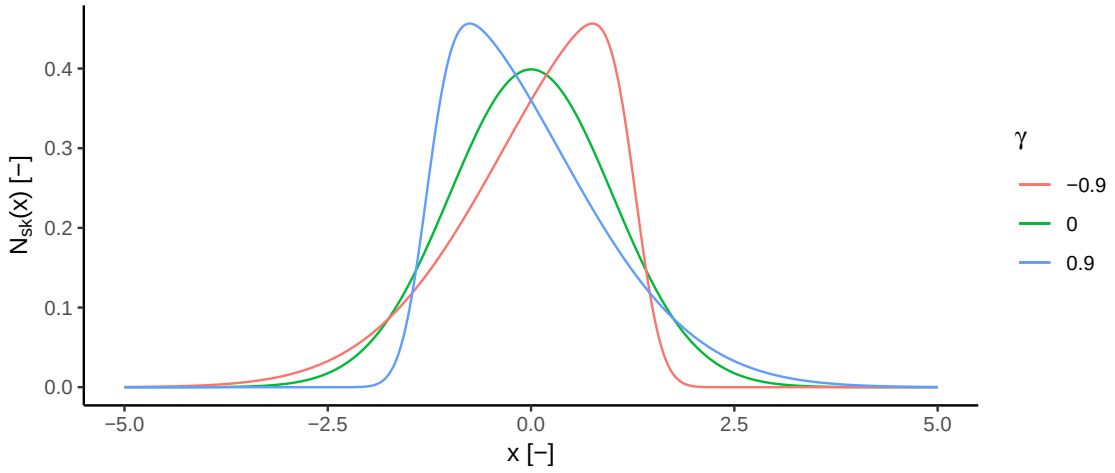

Figure 2.9: Examples of a skewed normal distribution. All three models have $\mu = 0, \sigma = 1$. The function is equal to the standard normal distribution if $\gamma = 0$.

In order to use this distribution with parameters gained from a sample, it is necessary to define estimates for the parameters of the skewed normal. It is possible to create a PDF, which is described by the usual parameters mean μ, standard deviation σ and skewness γ. The maximum skewness for the skewed normal distribution is limited to $\gamma \in [-1, 1]$ though. A maximum likelihood estimate can be calculated, which gives an estimate for α by this function:

$$\hat{\alpha} = \frac{\delta}{\sqrt{1-\delta^2}} \tag{2.8}$$

where δ can be calculated from the sample skewness $\hat{\gamma}$:

$$\delta = \operatorname{sgn}(\hat{\gamma}) \sqrt{\frac{\pi}{2} \frac{|\hat{\gamma}|^{\frac{2}{3}}}{|\hat{\gamma}|^{\frac{2}{3}} + \left(\frac{4-\pi}{2}\right)^{\frac{2}{3}}}} \tag{2.9}$$

The parameter ξ and ω can be calculated using $\hat{\alpha}$ as well as the mean and standard deviation of the sample:

$$\omega = \sqrt{\frac{\sigma^2}{1 - \frac{2\delta^2}{\pi}}}, \quad \xi = \mu - \omega\delta\sqrt{\frac{2}{\pi}} \tag{2.10}$$

with δ being:

$$\delta = \frac{\hat{\alpha}}{\sqrt{1 + \hat{\alpha}^2}} \tag{2.11}$$

Figure 2.9 shows several examples for the skewed normal distribution with different skewness parameters. If the skewness parameter is set to zero, the resulting distribution is equal to the normal distribution. Therefore the distribution is appropriate in situations where a normal distribution should be extended by skewness.

The Cauchy distribution, also known as Lorentz distribution, is a heavy-tailed distribution. While the peak of the Cauchy distribution is still tall, its tails decay slower than those of the normal distribution. The normal distribution's tails decay quickly as 99% of all values are in the range $\mu \pm 2.576\sigma$. It is a continuous probability function with the special property that neither mean or variance are defined. Instead only the median can be given - even though the distribution is symmetric. The PDF has two parameters $s > 0$ and $-\infty < t < \infty$, where t is equal to the median and s is a scale parameter. The PDF of the Cauchy distribution is given in equation 2.12. Examples of different parameters can be seen in figure 2.10. The scale parameter is similar to the standard deviation. It scales the width of the peak.

$$f(x) = \frac{1}{\pi} \cdot \frac{s}{s^2 + (x-t)^2} \tag{2.12}$$

When $t = 0$ and $s = 0$, the Cauchy distribution is also equal to the Student's t-distribution with one degree of freedom.

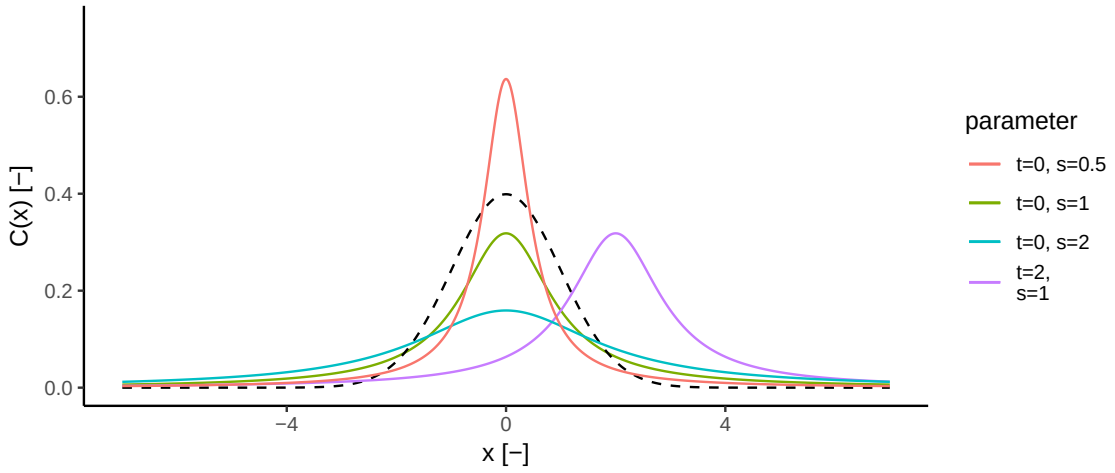

Figure 2.10: Cauchy distributions with different parameters. The dashed line shows a standard normal distribution as reference.

2.5 Probability Density Function for Total BVTV

Having now several building blocks in hand, it is possible to construct a PDF for the total BVTV. This function can then be used to reduce the number of variables of the BVTV frequency distribution from several thousand to only a dozen. The actual number of variables depends on the granularity and number of single PDF which contribute to the overall function.

Using the knowledge about the structure of bone and its composition, a theoretical model describing the total BVTV can be created. At least two different distributions should contribute to the overall distribution of bone. At least a cortical and a trabecular distribution. Voids, like in the diaphysis, are also part of bones. Thus, a third distribution accounting for void space should be added as well. But imaging technologies are not perfect and both the machine as well as the image post-processing add an error to the resulting image, which can be either an additive error to the whole image or a convolution of an error function. To simplify the calculations, only an additive error is added here. This results in four different distributions f, which are scaled by their volume fractions φ:

$$f_{\mathrm{BVTV}} = \varphi_{\mathrm{void}}\, f_{\mathrm{void}} + \varphi_{\mathrm{tb}}\, f_{\mathrm{tb}} + \varphi_{\mathrm{ctx}} f_{\mathrm{ctx}} + \varphi_{\mathrm{error}} f_{\mathrm{error}} \tag{2.13}$$

It is required that the integral of f_{BVTV} is one in order to form a PDF. This is not necessarily the case. Therefore, the whole equation is scaled in such a way to have an integral of one. This can be achieved by multiplying the volume fractions φ with a common term. It should be noted that the sum of all volume fractions φ is not necessarily one. A more detailed explanation is given in the appendix A.1. An example of such a model is shown in figure 2.11.

Such a model will also have different parameters at different sites inside the bone. For example, in the diaphysis, where almost no trabecular bone is found, only the cortical peak and the void distribution will be observed. On the other hand, at regions with less cortical bone - like the femoral head - this curve will contain almost only the trabecular distribution.

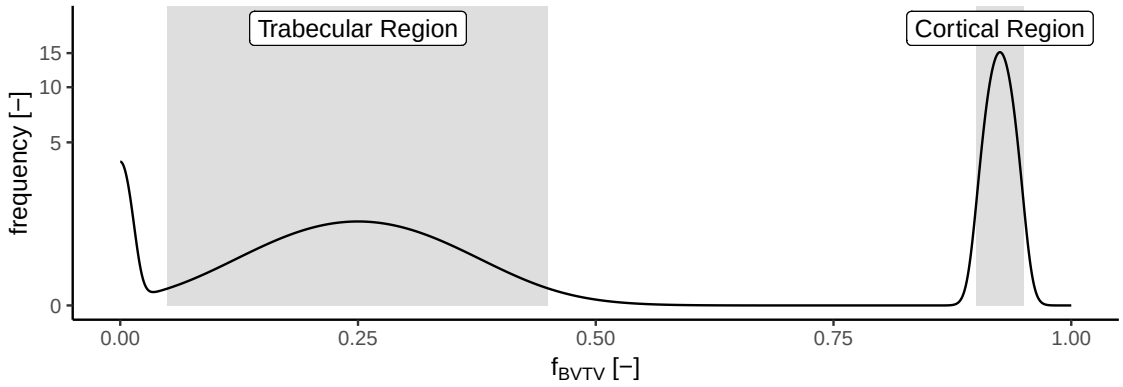

Figure 2.11: Example for a theoretical distribution of BVTV.
Using the distribution $0.95 \cdot (0.1\,N(0, 0.01) + 0.5\,N(0.925, 0.0125) + 0.4\,N(0.25, 0.1))$. Only normal distributions $N(\mu, \sigma)$ are used. The volume fractions indicate a mixture of approximately 10% voids, 40% trabecular bone and 50% cortical bone. 0.95 is a correction factor to scale the integral of the whole function to one.
The mean values for cortical and trabecular bone relates to the range of porosity from the literature. For cortical bone a porosity of 5 to 10% was assumed, while the porosity of trabecular bone is given with 55 to 95%. The standard deviations relate to the range of porosity found in the regions of bone. For the normal distribution approximately 95% are in the range of $\pm 2\sigma$. Therefore, the standard deviations are 0.1 and 0.0125 for trabecular and cortical bone respectively, as trabecular bone ranges from 0.05 to 0.45 and cortical bone from 0.9 to 0.95. Cortical bone range is given with 0.9 to 0.95. These regions are also marked as grey in the plot.

The resulting model will have a number of parameters, which can be related to quantities observed in bone as well. The mean of f_{tb} and f_{ctx} is directly related to $\mathrm{BVTV}_{\mathrm{tb}}$ and $\mathrm{BVTV}_{\mathrm{ctx}}$. The standard deviation accounts for the width of the distribution around the mean value. Thus, the standard deviation describes the range of porosity around the mean in each region of bone. Certain variables have a pre-defined value. The mean of f_{void} will always be 0 - as it gives the fraction of voids inside the bone at the current VOI size.

2.6 Influence of the Cortical/Trabecular Transition Zone

The distribution of BVTV values can either be calculated for the total volume or for cortical and trabecular volume separately. The latter case results in two distributions, while the former case creates a single distribution containing both parts of bone. On a first glance, the sum of the separated distributions should be equal to the total distribution. But this is not always the case as both methods create different distributions. The reason for this behaviour is the region at the transition zone between cortical and trabecular bone, referred to as cortical/trabecular border.

In a fictitious volume with volume fractions of a half each, $\mathrm{BVTV}_{\mathrm{ctx}}$ is measured to be 0.95, while $\mathrm{BVTV}_{\mathrm{tb}}$ is only 0.25. $\mathrm{BVTV}_{\mathrm{tot}}$ can be calculated to be 0.6. The effect on the distribution can be seen in figure 2.12. Separating the data first will also result in a much more separated distribution between the cortical and trabecular bone, while the distribution of the cortical/trabecular border shows up as a band of

values between the two peaks if the total bone is used.

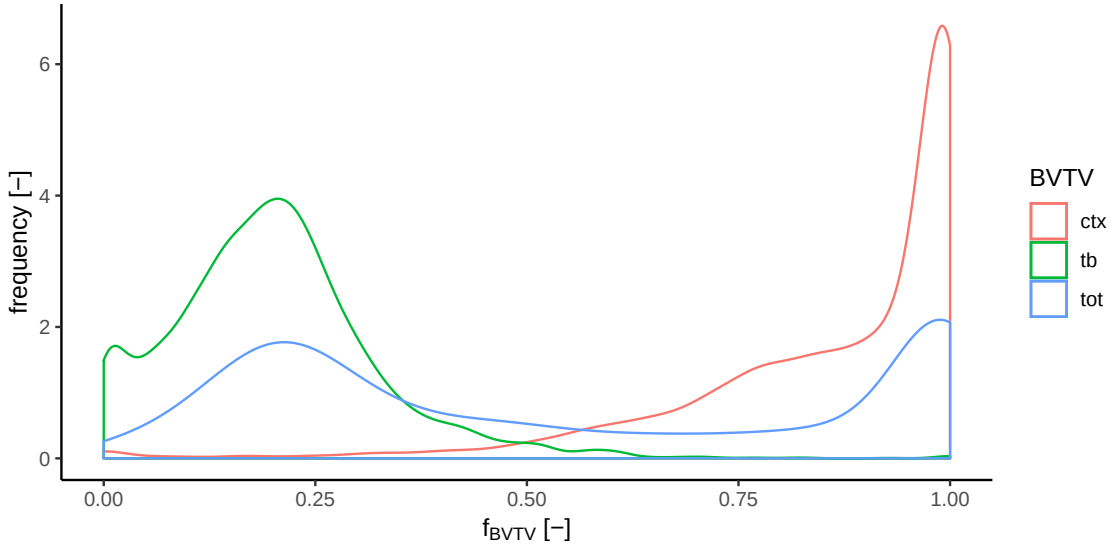

Figure 2.12: Influence of separating bone first before calculating the distribution. A long flat section can be seen between 0.5 and 0.8 when $\mathrm{BVTV_{tot}}$ is used. This section contributes to the cortical/trabecular border.

Depending on the question to answer, one or the other method might be used. One question is how the cortical/trabecular border changes during ageing. The changes in porosity are already discussed. The images should not be separated if those changes should be visible in the distribution. The reason is, that the separation technique might not separate the cortical/trabecular border zone equally for all age groups. If the cortical/trabecular border can be separated very precisely in younger age, it might not be easily possible in old bone due to large pores in this zone. Such porous bone might be classified as trabecular bone instead. This means, that parts of the cortical distribution will migrate to the trabecular distribution due to ageing. But the flow from each distribution to another cannot be tracked without performing specialized studies and image registration. Therefore, $\mathrm{BVTV_{tot}}$ is used instead of the separated distributions, in order to reduce artefacts in both distributions due to the separation.

2.7 Simple Geometry Model for Specific Surface

An analytical model is presented here, which uses only simple geometric shapes like cubes as VOI and cylinders either as pores or trabeculae. 3D models of both shapes can be seen in figure 2.13.

Equations for both $\mathrm{BVTV_{ctx}}$ and $\mathrm{BSTV_{ctx}}$ can be given for cortical bone. The geometrical model uses a cube with side length L and a hollow cylinder with radius r. The hollow cylinder represents a single channel inside the dense bone matrix.

$$\mathrm{BVTV_{ctx}} = \frac{L^2 - \pi r^2}{L^2} \tag{2.14}$$

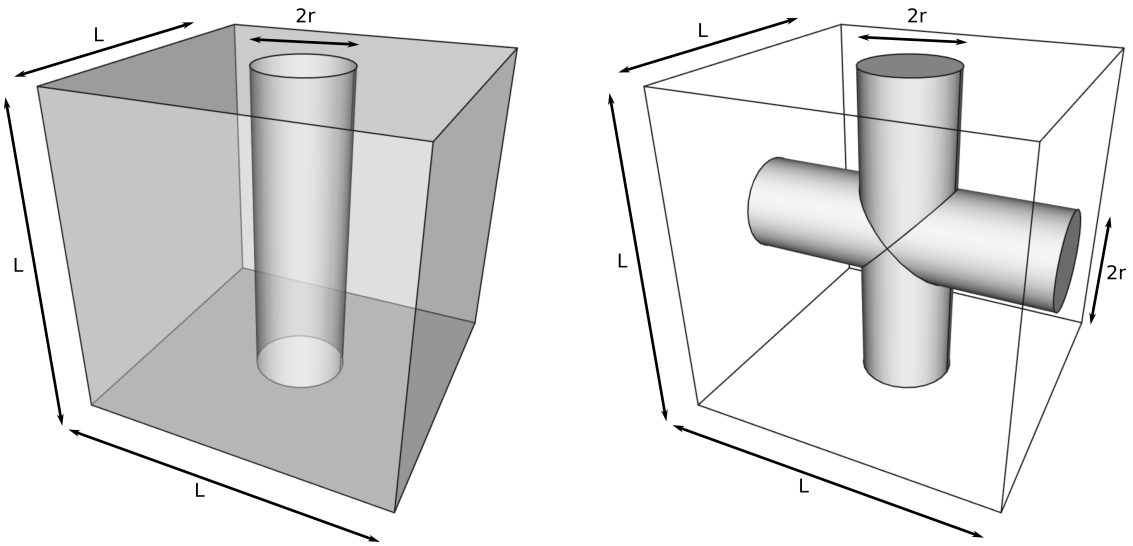

Figure 2.13: Model for cortical (left) and trabecular (right) bone. Each volume is a cube with either a cylindrical pore or two cylindrical bone cylinders (trabeculae). Each cube has the volume L^3, while the cylinders have a diameter of $2r$.

$$\mathrm{BSTV}_{\mathrm{ctx}} = \frac{2\pi r}{L^2} \tag{2.15}$$

Inserting equation 2.14 into equation 2.15 gives an equation for the specific surface in dependency of only the relative volume fraction.

$$\mathrm{BSTV}_{\mathrm{ctx}} = \frac{2\sqrt{\pi}}{L}\sqrt{1 - \mathrm{BVTV}_{\mathrm{ctx}}} \tag{2.16}$$

This equation is valid for $0 \geq r \geq \frac{L}{2}$, i.e. $\mathrm{BVTV}_{\mathrm{ctx}}$ between around 21% and 100%. If r would be larger, the cylinder would intersect the cube's surfaces. Therefore, another model needs to be created, which can be used for lower BVTV values.

This model, also called trabecular model, uses dense cylinders with radius r in an otherwise empty cube with edge length L. When both cylinders intersect each other, a correction term needs to be applied. The intersected figure is also called a Steinmetz 2-solid and equations for surface area and volume are available [50]. For brevity, the complete calculation is shown in the appendix in chapter A.2. Equations for $\mathrm{BVTV}_{\mathrm{tb}}$ and $\mathrm{BSTV}_{\mathrm{tb}}$ can be written as:

$$\mathrm{BVTV}_{\mathrm{tb}} = \frac{2L\pi r^2 - \frac{16}{3}r^3}{L^3} \tag{2.17}$$

$$\mathrm{BSTV}_{\mathrm{tb}} = \frac{4L\pi r - 16r^2}{L^3} \tag{2.18}$$

It is required that $L \geq \frac{4r}{\pi}$, otherwise the result will be negative. Likewise, inserting equation 2.17 into equation 2.18 results in the trabecular model:

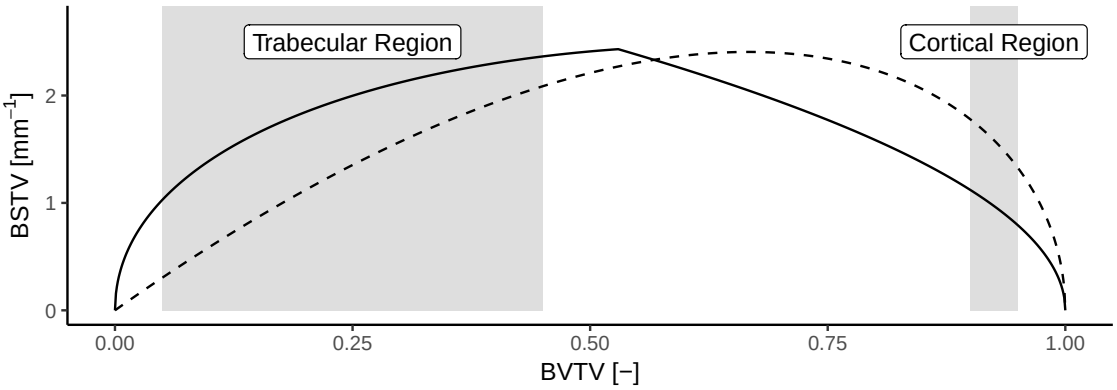

Figure 2.14: Joined BSTV curve for the Steinmetz 2-solid type trabecular structure and for the cortical cylindrical type structure. The variable L is set to 1. In grey are the ranges of trabecular and cortical bone according to literature. The dashed line gives the model of LEREBOURS et al. [54]. The coefficients are set to $a = 6.25$ and $b = 1$ to match the scale of the geometrical model.

$$\mathrm{BSTV}_{\mathrm{tb}} = \frac{\pi^2}{L}\left(\frac{1}{4} - \sin^2\left(\frac{1}{3}\arcsin\left(1 - \frac{48\,\mathrm{BVTV}_{\mathrm{tb}}}{\pi^3}\right)\right)\right) \tag{2.19}$$

Both models still depend on the parameter L. The ratio of r and L should be taken in such a way, that they reflect the real geometry of bone. As a single trabeculae is a maximum of $200\,\mu\mathrm{m}$ in radius, a good estimation for L might be $1\,\mathrm{mm}$, which is in the macroscopic region. This means, that this model can be used in macroscopic remodelling models.

The cortical model is not as accurate as a model that takes into account several smaller pores. The single large channel of radius r_1 can be divided into n small channels of radius r_2. When keeping the volume constant, the specific surface will still change as $r_2 = \frac{r_1}{\sqrt{n}}$. Thus, it will be $\sqrt{n}$ times larger than the surface of a single channel. A similar relationship exists for the trabecular model. The total surface area increases if more smaller cylinders are used instead of fewer larger ones. The "advanced" model has the new parameter n, which is not dependant on BVTV. This parameter needs to be fitted to has some relationship to BVTV in order to use the model.

Both formulations for $\mathrm{BSTV}_{\mathrm{tb}}$ and $\mathrm{BSTV}_{\mathrm{ctx}}$ can be used in a single function. The point where both functions are equal can be found by setting $\mathrm{BSTV}_{\mathrm{tb}} = \mathrm{BSTV}_{\mathrm{ctx}}$. This point results in $\mathrm{BVTV} \approx 0.53$. Figure 2.14 shows both equations and their transition. The plot also shows the model of LEREBOURS et al. [54] for comparison. While the overall shape is similar for both models, the geometry model gives a larger effective surface in the trabecular region but a smaller effective surface in the cortical region.

2.8 Remodelling Equations Based on Mass Rates

It is possible to describe changes in bone mass as a differential equation. The rate of mass over time $\frac{dm}{dt}$ for each volume element is given by the positive values mass input m_{in} and mass output m_{out}:

$$\frac{dm}{dt} = m_{\mathrm{in}} - m_{\mathrm{out}} \tag{2.20}$$

Figure 2.15 shows such mass rates and the resulting mass curve over time. A perturbation of the input mass rate is added between the age of 45 and 60 resulting in a faster drop of overall mass.

The rate of mass change can be made dependant on the available surface inside the VE. Combining equation 2.20 with the BSTV model from chapter 2.7 gives the equation for the rate of mass which is proportional to BVTV and also to the current mass of the VE m:

$$\frac{dm}{dt} = c\ (m_{\mathrm{in}} - m_{\mathrm{out}})\ \mathrm{BSTV}(m) \tag{2.21}$$

The proportionality constant c needs to be adopted to give the correct result. Resorption and addition of bone mass, i.e. osteoclastic and osteoblastic activity, can be modelled simultaneously at a macroscopic level, as it is thought that the bone multicellular unit (BMU) are working in a coordinated way [89]. Instead of using a mass m, also the volume fraction BVTV can be used as both values are proportional to each other. This model only works on a porous bone. If BVTV is 1, the resulting surface is zero, thus the change in mass will be also zero. Real bone does have this property, but image data or artificially created data might have BVTV values of one or larger.

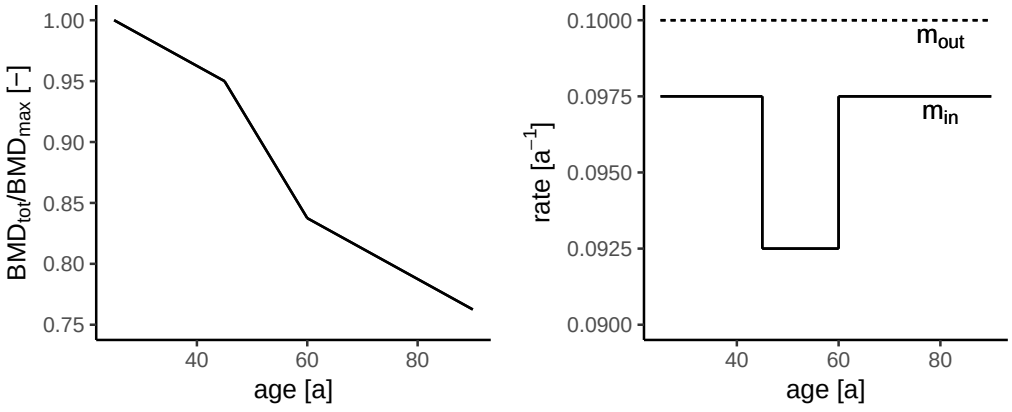

Figure 2.15: BMD as a simplified function of age (left) and rates of mass input and output which creates this curve (right). The left curve can be calculated by taking in the integral of $m_{\mathrm{in}} - m_{\mathrm{out}}$ over time. The calculations starts at PBM, therefore the BMD starts at one.

2.9 HR-pQCT: Distal Radius Study Using Whole Segment

The overall procedure of image processing and data analysis can be seen in the visual abstract in figure 2.17. It structures itself into four parts, where each part depends on the previous one. First, BMD and volume figures as well as the relative frequencies of BVTV were extracted from the images. KDEs were constructed from the frequency distributions. Each KDE was then grouped by sex and age. A mean KDE was then calculated for each group. Curve fitting was applied to the mean KDE in order to reduce the variables. In the last step, three different approaches were used to investigate the differences between age groups.

Radius HR-pQCT scans were obtained from the DRFO study [96]. In this study, a total of 21 fresh frozen, cadaveric human radius pairs of both sexes in different ages were scanned using a HR-pQCT (XtremeCT, Scanco Medical AG, Switzerland). The X-ray parameters were $60\,\mathrm{kVp}$ and $900\,\mu\mathrm{A}$ with an isotropic voxel size of $82\,\mu\mathrm{m}$ and a total resolution of 1536×1536 pixel per slice and 1617 pixel length ($125.952\,\mathrm{mm} \times 125.952\,\mathrm{mm} \times 132.594\,\mathrm{mm}$). The images were already scaled to BMD using the calibration curve of the HR-pQCT device and segmented using Laplace-Hamming filter, thresholding and morphological closing filter [96]. Also masks for both trabecular and cortical bone were available, which were created using the Fill method of MedTool [74]. Exemplary slices of the three images can be seen in figure 2.16. Masking allowed to determine trabecular and cortical sections in the image, while segmentation showed the difference between actual bone (white in the image) and other tissues (black). Age and sex information was missing for three pairs, which got excluded. The data set was separated into two groups for each sex: all individuals below 80 and all above. This age was chosen, as it separated the sample into almost equally sized groups of four pairs per group except for males below 80 with six pairs.

Figure 2.16: Slices from the image processing.**A**: BMD scaled image, **B**: masks containing trabecular bone and cortical bone, **C**: bone segmentation

Figure 2.17: Next page. Visual abstract of the process of extraction and computation. The whole process is grouped into four parts. 1) read the CT image data and compute KDEs and volume fractions as well as BMD measurements. In order to create the KDE, the relative frequencies were calculated from the masks and segmentation of the CT image. 2) group the data into four groups based on sex and age. 3) calculate mean KDE curve for each group and use a nonlinear least square (nls) curve fitting in order to get the parameters for the BVTV frequency model. 4) compare the two age groups for each sex by using three different methods: The BVTV frequency difference model, the BVTV age rate model and an analytical remodelling model.

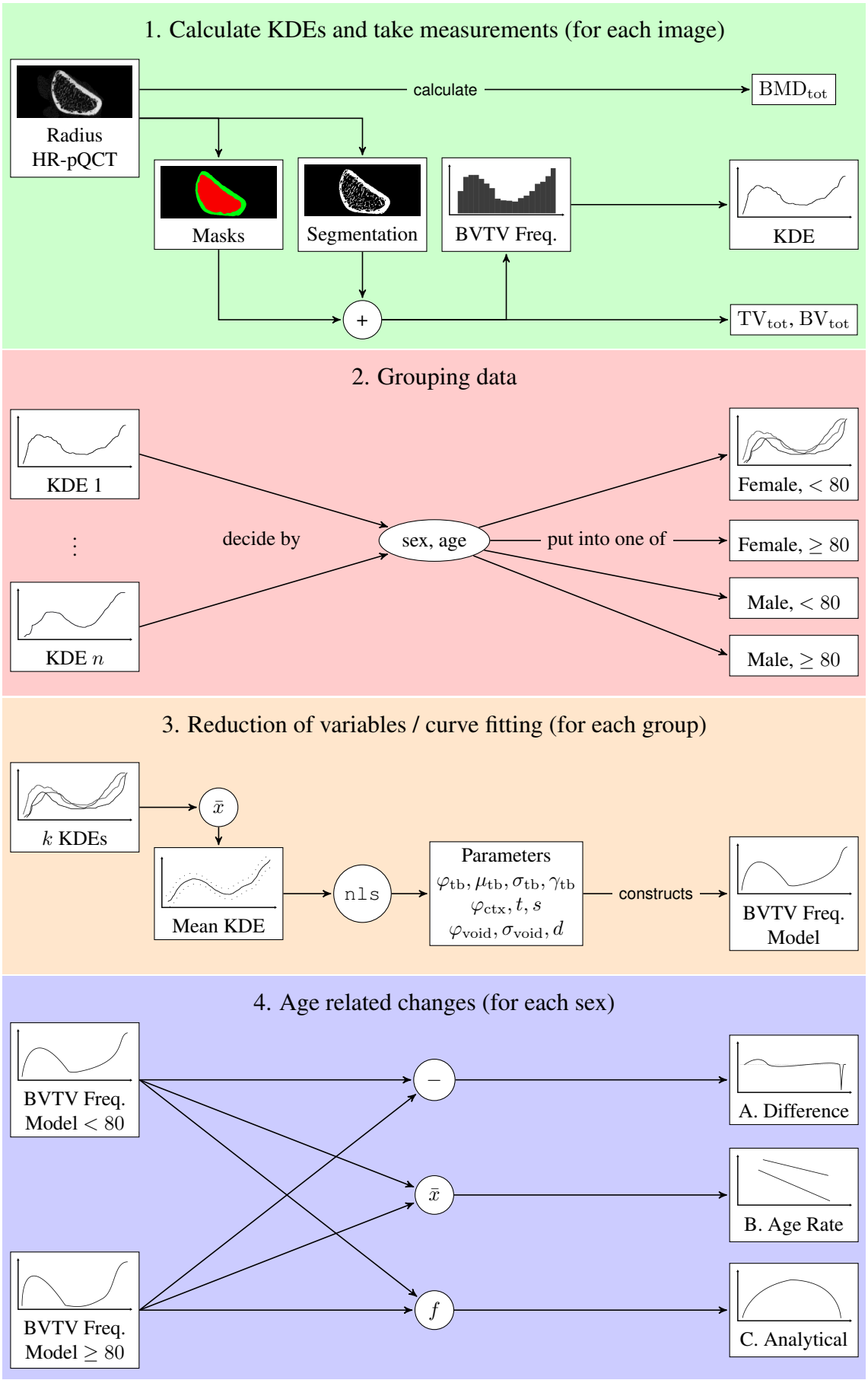
1. Calculate KDEs and take measurements (for each image)
Radius
HR-pQCT
calculate
$\mathrm{BMD}_{\mathrm{tot}}$
Masks
Segmentation
BVTV Freq.
KDE
+
$\mathrm{TV}_{\mathrm{tot}}$, $\mathrm{BV}_{\mathrm{tot}}$
2. Grouping data
KDE 1
KDE n
decide by
sex, age
put into one of
Female, < 80
Female, ≥ 80
Male, < 80
Male, ≥ 80
3. Reduction of variables / curve fitting (for each group)
k KDEs
$\bar{x}$
Mean KDE
nls
Parameters
$\varphi_{\mathrm{tb}}, \mu_{\mathrm{tb}}, \sigma_{\mathrm{tb}}, \gamma_{\mathrm{tb}}$
$\varphi_{\mathrm{ctx}}, t, s$
$\varphi_{\mathrm{void}}, \sigma_{\mathrm{void}}, d$
constructs
BVTV Freq.
Model
4. Age related changes (for each sex)
BVTV Freq.
Model < 80
BVTV Freq.
Model ≥ 80
−
$\bar{x}$
f
A. Difference
B. Age Rate
C. Analytical

The whole scanned segment was chosen as ROI, while adjacent cubes with edge length of $1.558\,\mathrm{mm}$ ($1.5\,\mathrm{mm}$ rounded to the next voxel dimension) were used as VOI. The following *global* parameters were calculated for the whole ROI:

1. Total BMD: $\mathrm{BMD}_{\mathrm{tot}}$
2. Total BVTV: $\mathrm{BVTV}_{\mathrm{tot}}$
3. Total cortical and trabecular volume: $\mathrm{TV}_{\mathrm{ctx}}$, $\mathrm{TV}_{\mathrm{tb}}$
4. Cortical and trabecular bone volume: $\mathrm{BV}_{\mathrm{ctx}}$, $\mathrm{BV}_{\mathrm{tb}}$

TV and BV values were calculated using the masks and segmentation, while $\mathrm{BMD}_{\mathrm{tot}}$ was calculated directly using the BMD calibrated grey-value image.

Statistical tests were performed on the gathered data. To test the influence of the paired radii, a two sided t-test for connected samples was performed on the *global* $\mathrm{BVTV}_{\mathrm{tot}}$ and $\mathrm{BMD}_{\mathrm{tot}}$ of each sample. The differences between $\mathrm{BVTV}_{\mathrm{tot}}$, $\mathrm{BMD}_{\mathrm{tot}}$ and volumes between sexes were calculated using two sided Welch test (t-test), as both distributions do not have the same variance.

Next, the distribution of *local* $\mathrm{BVTV}_{\mathrm{tot}}$ was calculated for all VOI inside the ROI. All VE were rejected which contained more than 90% zero volume to avoid partial volume effects. BVTV was calculated using the segmentation approach. The resulting data was collected into a comma-separated values (CSV) file and then loaded into R [78] for further processing. From the frequency distribution of BVTV values, a probability density curve was calculated for each sample using a KDE. A Gaussian kernel was used for all KDE, the lower limit was set to 0 and the upper limit to 1. The bandwidth was calculated using the *SJ* algorithm [91]. Then the mean probability density curve as well as standard deviation and standard error was calculated from the individual KDEs in each group. The resulting mean curve was then scaled to have an area of one under the whole curve, i.e. to be used as a PDF again.

A model for BVTV was fitted to the density function, in order to minimize variables and noise in the function. Some parameters need to be restricted to a certain range. Therefore, only certain algorithms can be used for minimisation, as not all support minimising with a parameter range. A non-linear adaptive least squared algorithm was used which was provided by the R function `nls` and the netlib PORT library [20].

The BVTV model described in section 2.5 was used for fitting. The resulting function for f_{BVTV} can be seen in equation 2.22. The starting values and limits for fitting are given in table 2.1. $\hat{N}_{sk}$ is an estimate for the skewed normal distribution with parameters ξ, ω and α, estimated from the location parameters μ and σ and the shape parameter γ (skewness). $C(t,s)$ is the Cauchy distribution and $N(\mu,\sigma)$ is the normal distribution. The variable μ_{void} was set to zero and was not fitted. An error term d was added, which accounted for a shift of the data in positive y direction.

$$f_{\mathrm{BVTV}} = \underbrace{\varphi_{\mathrm{tb}} \cdot \hat{N}_{sk}(\mu_{\mathrm{tb}}, \sigma_{\mathrm{tb}}, \gamma_{\mathrm{tb}})}_{trabecular} + \underbrace{\varphi_{\mathrm{ctx}} \cdot C(t,s)}_{cortical} + \underbrace{\varphi_{\mathrm{void}} \cdot N(\mu_{\mathrm{void}}, \sigma_{\mathrm{void}})}_{voids} + \underbrace{d}_{error} \tag{2.22}$$

The whole model was scaled after the fitting to have an integral of 1, to form a correct PDF. Scaling was performed by multiplying the constants φ_{tb}, φ_{ctx}, φ_{void} and d by a correction factor.

		start	lower	upper	
trabecular	φ_{tb}	0.1	0	∞	
	μ_{tb}	0.2	0.05	0.75	
	σ_{tb}	0.1	0	∞	
	γ_{tb}	0	-0.9	0.9	
cortical	φ_{ctx}	0.3	0	∞	
	t	0.99	0.8	1.1	
	s	0.01	0.001	∞	
voids	φ_{void}	0.5	0	1	
	σ_{void}	0.01	0	∞	
	d	$\bar{x}$	0	∞	start value: median of distribution

Table 2.1: Parameters used in the model with their start value and limits.

An iterative process was used to fit the model, as the algorithm will find local minima. The first starting values were guessed by statistical analysis of the data and visual inspection. Ranges for each parameter were set in order to produce only models in the definition region of the function. Residual sum squared (RSS) was used to check the model for a good fit. The resulting curve is called "BVTV frequency model", which is described by a set of parameters.

For each sex the older group's model was subtracted form the younger group's model. The resulting curve is called "BVTV frequency difference model", as it gives the changes for each BVTV in the bone. The total bone turnover was calculated from the resulting frequency distribution which is given by equation 2.2.

$\mathrm{BVTV}_{\mathrm{tot}}$ was calculated for each model in the same way and a linear model was created by taking the mean ages and $\mathrm{BVTV}_{\mathrm{tot}}$ values of each group. This model is called "BVTV age rate model" and describes the linear change of BVTV over age. Additionally, the rate was calculated for the cortical region and trabecular region. The cortical region consisted of all values larger than 75%, while the trabecular was formed by using all values between 5% and 75%. Different ranges for trabecular and cortical BVTV are available from the literature. The actual ranges also depend on the size of the VOI. If the VOI is set to the organ's size, there will almost always be some bone in the VOI. Contrary a very small VOI might not contain any bone. Cortical bone is usually regarded as "high" density, typical values are 70% [112], 85% [54] and even 90% [14]. In order to account for the smaller VOI size used in this work, the value was set to 75%. Trabecular bone can be defined as all bone with a lower porosity than cortical bone [7]. Ranges for trabecular bone are much more variable but should be in the range of 5 to 30% [33] and less than 7% [77]. It was found, that most samples in the radius study had a local minima in the BVTV frequency curve at about 5%. Therefore, the lower bound for trabecular bone was to to 5% while the cortical threshold of 75% is the upper bound.

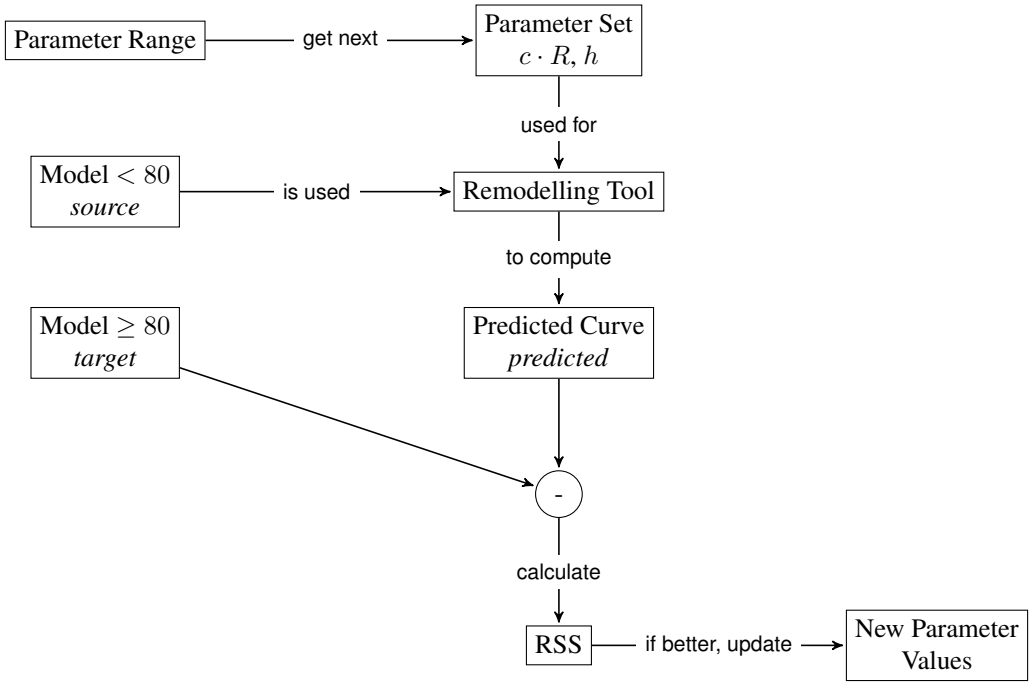

Figure 2.18: Process of generating the predicted curves for the analytical model. As the parameters are unknown beforehand, they are fitted using a minimal squared difference approach and grid search. The parameter ranges are chosen in an interval where values are expected.

Additionally the rate based remodelling equations were used to predict the bone frequency models of the groups above age of 80 by using the data from the groups below age of 80. The model of the group below age of 80 is called *source*, while the other age group is called *target*. The curve calculated by the remodelling model is called *predicted*.

Three parameters are required to describe the remodelling model. The parameter c is a proportionality constant for the BSTV part and $R = m_{\text{in}} - m_{\text{out}}$ being the total mass rate. A new parameter $h \in [0, 1]$ was used, which describes the fraction of bone under remodelling. Only the fraction h for each BVTV value was allowed to change, the other fraction $1 - h$ was kept constant. A physiological value for the fraction of tissue under remodelling is in the range of 10% per year [79]. Therefore, the value for h was fixated to 0.1.

Euler's method was used to solve the differential equations for the change of mass using a time step of 0.1. At first, random generated data stemming from a normal distribution was used to test the model's functionality. Then the *source* curve was used as an input for the model. The remodelling started with the mean age of the younger group and stopped at the mean age of the older group.

An exhaustive grid search over a defined parameter range was used to minimize the RSS of the *predicted* and *target* curve. The product of the parameters c and R and the parameter h were optimized. The limits were $0.001 \leq c \cdot R \leq 0.05$ using an initial step size of 0.001 and $0.01 \leq h \leq 1$ using an initial step size of 0.01. A finer search was performed in a second iteration. This search was performed using the best parameter $\pm$ half the step size of the previous run and a new step size of one tenth the old step size. Although h was already fixed, a full grid search was performed with this parameter to investigate the global shape of the RSS function. For comparison, the BSTV model of LEREBOURS et al. [54] was implemented

as well. Again, a grid search was performed to find the best fitting parameter based on minimization of RSS.

2.10 HR-pQCT: Distal Radius Study Using Slices

Additional values for the most distal $20.5\,\mathrm{mm}$ of the radius were calculated in the same way as described in the literature [103]. Measured *global* parameters for the whole ROI where:

1. Trabecular volume: $\mathrm{TV_{tb}}$
2. Cortical volume: $\mathrm{TV_{ctx}}$
3. Total volume: $\mathrm{TV_{tot}} = \mathrm{TV_{tb}} + \mathrm{TV_{ctx}}$
4. Trabecular bone mineral content (BMC): $\mathrm{BMC_{tb}}$
5. Cortical BMC: $\mathrm{BMC_{ctx}}$
6. Total BMC: $\mathrm{BMC_{tot}} = \mathrm{BMC_{tb}} + \mathrm{BMC_{ctx}}$
7. Total BMD: $\mathrm{BMD_{tot}}$
8. Trabecular BMD: $\mathrm{BMD_{tb}}$
9. Cortical BMD: $\mathrm{BMD_{ctx}}$
10. Trabecular BVTV: $\mathrm{BVTV_{tb}} = \frac{\mathrm{BMD_{tb}}}{\mathrm{BMD_{max}}}$

$\mathrm{BVTV_{tb}}$ was calculated by applying equation 2.4 with $\mathrm{BMD_{max}}$ set to $1200\,\mathrm{mg/cm^3}$, as described in the publication [103]. These values were solely calculated for comparison with the literature in order to check whether the current set of bones was similar to existing studies. No BVTV frequency models were created for the slices.

2.11 QCT: Proximal Femur and Lumbar Spine Study

QCT scans of femur and vertebral bodies from the FREEDOM study [16] were used to test the frequency models on QCT data. The effect of Denosumab was tested in the FREEDOM study on postmenopausal women in a randomized, placebo controlled trial. QCT images were created for a subset of the complete cohort, while all other patients were only monitored using DXA. The study was performed at eleven different centres with a total of 7868 women in the study. Examinations were performed at a baseline and at 12, 24 and 36 months after the study start. From the total of 7868 women, only 101 were imaged with QCT. The QCT images were BMD calibrated using cycling phantoms in all centres. Of one patient, the treatment information was not available. From the remaining 100 patients, 80 patients had a complete set of images of vertebrae and 57 had a complete set of the femur. For 47 patients, both image sets were available. For the vertebral data, L1 and L2 were separated from the image. For two patients only one vertebrae was available

while all other patients had both images. For one of the two patients, only L1 was separated, while the other had only L2. Therefore, per vertebrae a total of 79 images was available.

The original subset was selected in such a way to reflect the overall study cohort. To test the influence of the remaining samples, z-tests were performed on the age of the patient. Other data like BMI and geographical region was not available but recorded in the original study.

In comparison to the radius data set, the images of the FREEDOM study were created using different CT devices. Nine different devices were used, also using different voxel sizes. The sensor resolution was the same for all devices with 512×512 pixel. While the HR-pQCT produced cubic voxels, the QCT used in the FREEDOM study produced rectangular voxels. For the femur, two different datasets are available with either a pixel spacing of $391\,\mu\mathrm{m} \times 391\,\mu\mathrm{m}$ or $781\,\mu\mathrm{m} \times 781\,\mu\mathrm{m}$ called small field of view and large field of view, respectively. Some variations in the exact pixel spacing can be seen but are lower than $1\,\mu\mathrm{m}$. The slice thickness varied, depending on the device, and was either $1\,\mathrm{mm}$, $1.25\,\mathrm{mm}$ or $1.5\,\mathrm{mm}$. Vertebral bodies were always imaged with a pixel spacing of $351\,\mu\mathrm{m} \times 351\,\mu\mathrm{m}$. A few images were taken with $341\,\mu\mathrm{m}$ or $391\,\mu\mathrm{m}$ though. The slice thickness was either $0.5\,\mathrm{mm}$, $0.6\,\mathrm{mm}$, $0.625\,\mathrm{mm}$ or $0.65\,\mathrm{mm}$, again depending on the device. The X-ray tube potential was set to $120\,\mathrm{kVp}$, with the exception of some images using values in the range of $110\,\mathrm{kVp}$ to $140\,\mathrm{kVp}$. X-ray tube current was used in the range of $37\,\mathrm{mA}$ to $440\,\mathrm{mA}$, with a median of $100\,\mathrm{mA}$ for vertebrae and $227\,\mathrm{mA}$ for the femur. Most devices used a 16 bit resolution, while some devices only used 12 bit resolution. Usually all images of a series were created using the same device and settings, but some exceptions occur in the dataset.

The data was already segmented, separated and a ROI selected, according to the steps used for a finite element (FE) based study [113]. As the voxels are much larger, the BMD method for BVTV calculation was used instead of the segmentation method. The segmentation based method does not work on this size of voxels, as most of the voxels would be filled with bone. Frequency models were created for each image in the same manner as for the radius data. No curve fitting was applied as the resulting curves differed from the curves in the radius model. No theoretical model for the overall BVTV was available.

Chapter 3

Results

3.1 HR-pQCT: Distal Radius Study Using Whole Segment

The results are structured in the same way as shown in the visual abstract (figure 2.17). First, some general data is presented from the sample set. Then the BVTV frequency models are presented. At last, the results for the frequency model, age rate model and analytical model are shown.

$\mathrm{BMD}_{\mathrm{tot}}$ and $\mathrm{BVTV}_{\mathrm{tot}}$ were calculated from the samples. Regression models for $\mathrm{BMD}_{\mathrm{tot}}$ are given in figure 3.1. The loss in BMD over time is clearly visible in both men and women. Coefficient of determination (CoD) was higher in females while the low value for men indicates a high dispersion of the sample. Table 3.1 gives an overview about the figures of the sample in numerical terms. The loss in BMD and BVTV can be seen in the values as well. Linear regression models for $\mathrm{TV}_{\mathrm{ctx}}$, $\mathrm{TV}_{\mathrm{tb}}$, $\mathrm{BV}_{\mathrm{ctx}}$ and $\mathrm{BV}_{\mathrm{tb}}$ is given in figure 3.2. While the cortical volumes decreased, trabecular volumes increased for both sexes. The CoD are again low for men.

T-tests showed that, $\mathrm{BVTV}_{\mathrm{tot}}$ was higher in males ($p = 0.0478$) than in females, while $\mathrm{BMD}_{\mathrm{tot}}$ did not show any significant difference ($p = 0.0673$). There was no difference between left an right ($\mathrm{BVTV}_{\mathrm{tot}}$: $p = 0.277$, $\mathrm{BMD}_{\mathrm{tot}}$: $p = 0.355$) but a statistical significant difference between the higher and lower value ($\mathrm{BVTV}_{\mathrm{tot}}$: $p < 0.001$, $\mathrm{BMD}_{\mathrm{tot}}$: $p < 0.001$) was found. From the 18 samples, 13 had higher $\mathrm{BMD}_{\mathrm{tot}}$ and $\mathrm{BVTV}_{\mathrm{tot}}$ in the left arm. Volumes were larger ($p < 0.001$) for males than females for both $\mathrm{TV}_{\mathrm{ctx}}$ and $\mathrm{TV}_{\mathrm{tb}}$ as well as $\mathrm{BV}_{\mathrm{ctx}}$ and $\mathrm{BV}_{\mathrm{tb}}$.

	n	age[a] [a]	median [a]	range [a]	$\mathrm{BMD_{tot}}$[a] [$\mathrm{mgHA/cm^3}$]	$\mathrm{BVTV_{tot}}$[a] [-]
total	18	79.17 ± 12.28	75.5	$54 - 97$	520.54 ± 79.89	0.53 ± 0.073
female	8	81 ± 12.73	82	$67 - 97$	493.1 ± 80.15	0.51 ± 0.068
< 80	4	69 ± 3.12	67.5	$67 - 74$	568.38 ± 15.72	0.58 ± 0.013
≥ 80	4	93 ± 2.93	92.5	$90 - 97$	417.81 ± 23.77	0.45 ± 0.023
male	10	77.7 ± 12.04	75.5	$54 - 94$	542.5 ± 74.45	0.56 ± 0.071
<80	6	69.67 ± 7.69	72	$54 - 76$	568.29 ± 80.29	0.58 ± 0.078
≥ 80	4	89.75 ± 4.92	91	$83 - 94$	503.8 ± 45.44	0.53 ± 0.044

Table 3.1: Age, BMD and BVTV distribution from the radius data set. **a**: values are mean $\pm$ sd.

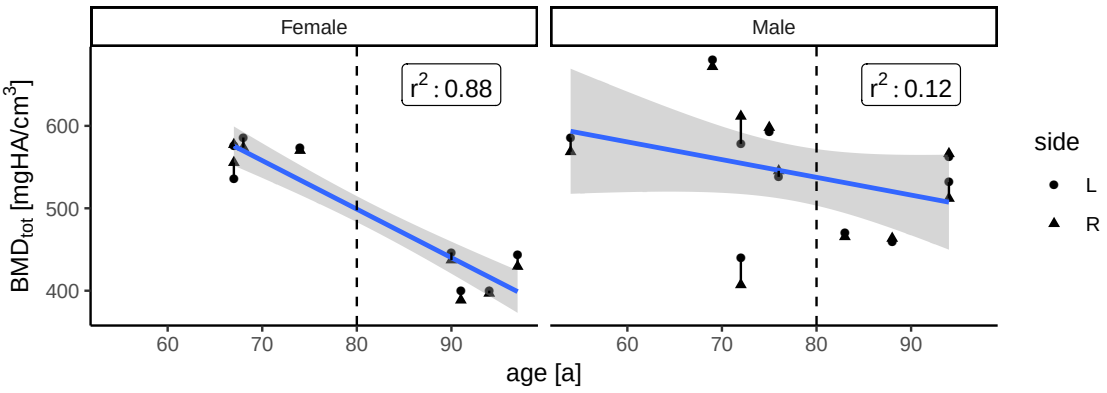

Figure 3.1: $\mathrm{BMD_{tot}}$ over age for the radius data set. Pairs are connected by lines. The two groups per sex are divided into all samples below the age of 80 and all above. The blue line gives a linear model for the age related loss of BMD, the grey region gives a confidence interval for the linear model.

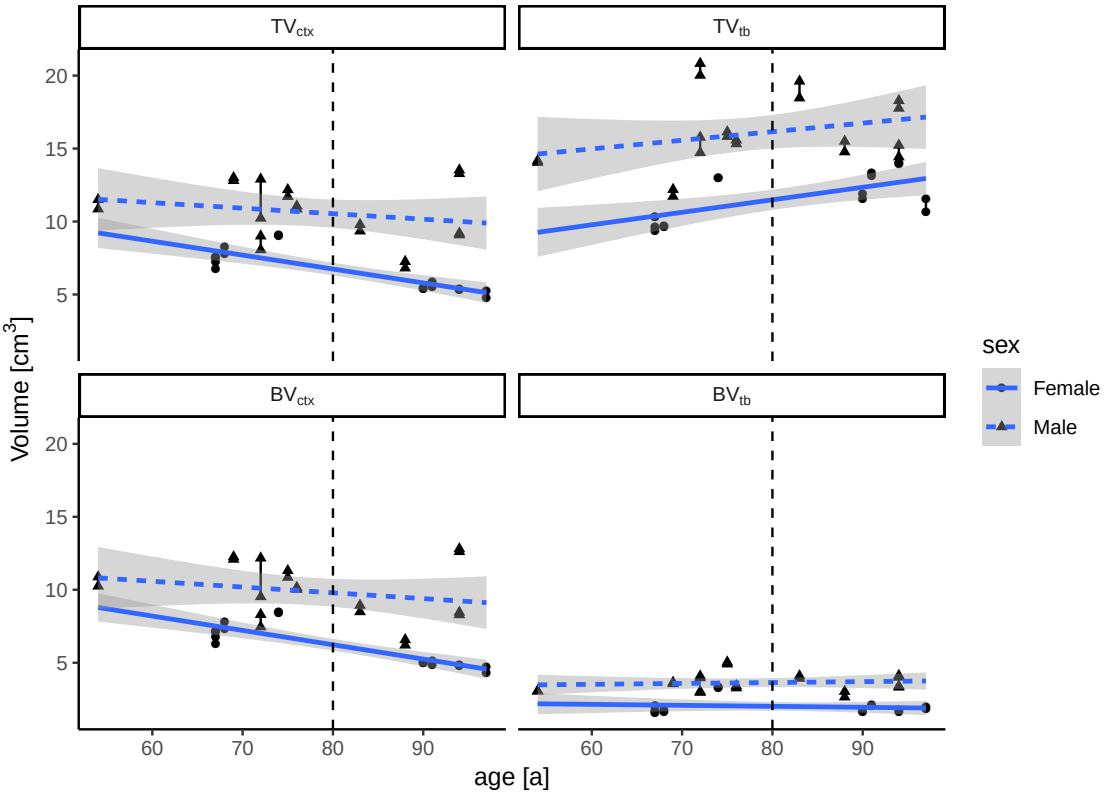

Figure 3.2: Linear regression models of total volume (upper) and bone volume (lower) for both cortical and trabecular region.The two groups per sex are divided into all samples below the age of 80 and all above. The blue line gives a linear model for the age related change of total and bone volume, the grey region gives a confidence interval for the linear model. r^2 for males: $\mathrm{TV_{ctx}}$: 0.051; $\mathrm{TV_{tb}}$: 0.084; $\mathrm{BV_{ctx}}$: 0.056; $\mathrm{BV_{tb}}$: 0.013. r^2 for females: $\mathrm{TV_{ctx}}$: 0.707; $\mathrm{TV_{tb}}$: 0.432; $\mathrm{BV_{ctx}}$: 0.749; $\mathrm{BV_{tb}}$: 0.0241.

3.1.1 BVTV Frequency Model

A density estimate using a KDE was created for each sample from the BVTV frequency distribution inside the ROI. Then the mean KDE was calculated for each group using the sample KDEs. This mean KDE was then scaled to have an integral of one. This results in four mean KDE curves, one for each sex in each group.

Figure 3.3 shows the mean KDE curves plus and minus the standard deviation for both sexes split into age groups. The shape of the mean KDEs for male and female are quite similar. Both have a prominent peak close to a BVTV of one a much broader distribution in the lower region of BVTV. The height of the peak is different in the two age groups for both sexes. A shift to the left in the older group of this broader distribution can clearly be seen. It is also notable, that the standard deviation in the lower region of BVTV in males is very high, while the two distributions are separating from each other in females. The region between 50% and 90% is very similar in both age groups and is almost a flat line for both males and females but was not zero.

The fitted functions for the mean KDE can be seen in figure 3.4, while the parameters of the fitted functions are given in table 3.2. A true goodness of fit (GoF) like CoD cannot be calculated for the fitted model as the model is non-linear. Therefore, only residual sum squared (RSS) were calculated and a visual inspection of the fitted curve was performed. From visual inspection of the fitted curve, the mean KDE curve was fitted good for most parts. RSS for each model were close to zero. Problematic areas, where the fit was not perfect, are in the region between the trabecular and cortical distribution as well as in the zones between the tail and the peak of the cortical distribution.

The differences between the groups are not only visible in the plots but are also found in the fitted parameters. When looking at the trabecular and cortical distribution separately, it can be seen that in both cases the location is shifted more to the left side. For the cortical distribution, the differences in median t are only marginal, but the shape parameter s as well as the volume fraction φ_{ctx} increased in both sexes. Especially the change in shape parameter s leads to a broader distribution. For the trabecular distribution, the mean μ_{tb} gets lower for both sexes, while the standard deviation σ_{tb} increased only for females but decreased for men. The skewness γ_{tb} got smaller, which means that the distribution is getting more symmetric, as the skewness of the first group was always larger than zero. The volume fraction φ_{tb} increased

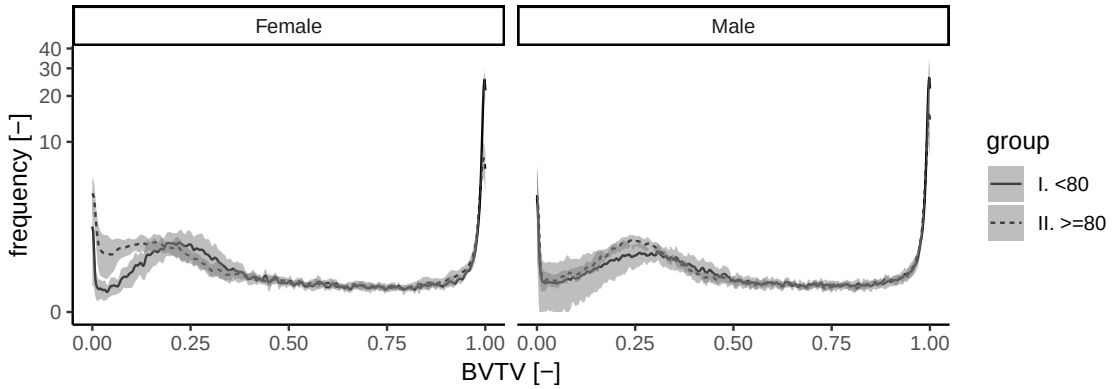

Figure 3.3: Mean KDE $\pm$ standard deviation in grey.

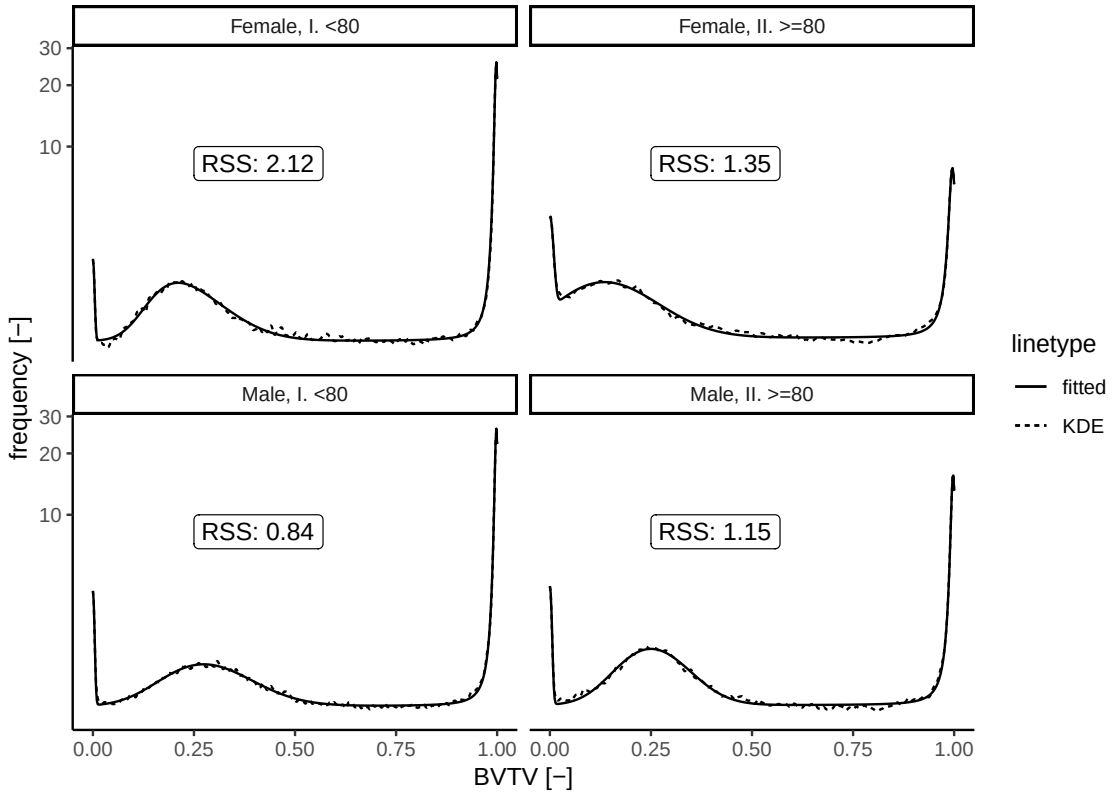

Figure 3.4: Mean KDE and fitted density function for the BVTV frequency model.

for the trabecular distribution, which means that the overall fraction of bone is getting larger in the lower BVTV zone. For the male groups, the trabecular standard deviation σ_{tb} got smaller while it increased in females. It can be observed, that the standard deviation of the mean KDE is much larger in the lower BVTV region for males than it is for females. The large standard deviation in this part of the curve indicates a high variability in the trabecular region. On the other hand, the cortical region shows a lower standard deviation. Contrary to females, the volume fraction of void φ_{void} decreased in males. The void's standard deviation increased in both sexes. The error term d only changed slightly in both sexes. This term accounts for the shift in positive y-direction of the whole distribution.

	Parameter	Female		Male	
		< 80	≥ 80	< 80	≥ 80
trabecular	φ_{tb}	0.018469	0.068053	0.032573	0.042648
	μ_{tb}	0.241742	0.148842	0.287240	0.255541
	σ_{tb}	0.090550	0.117222	0.108289	0.085060
	γ_{tb}	0.559934	0.224722	0.229504	0.129065
cortical	φ_{ctx}	0.277627	0.361344	0.233347	0.314119
	t	0.997783	0.995600	0.998012	0.997252
	s	0.004820	0.009056	0.004599	0.006083
voids	φ_{void}	0.415295	0.496929	0.401464	0.314119
	σ_{void}	0.003503	0.007822	0.003501	0.004337
error	d	0.450359	0.496929	0.499756	0.510343

Table 3.2: Fitted parameters and their values for all four groups. Correction was already applied to this parameters, thus the integral of the resulting PDF is equal to one.

3.1.2 BVTV Frequency Difference Model

To get an even better overview about the differences in the two groups, the fitted curve of the older group was subtracted from the younger one. The resulting curve is shown in figure 3.5. The difference curve shows that there are certain parts that increased while others decreased. Also the shifting trabecular distribution is clearly visible, as one part is below the zero line and one is above. The biggest change is in the cortical distribution, as the amount is reduced. The small peak in the positive direction before the cortical peak indicates a slightly shifting cortical distribution. As the two distributions have an area under the curve of one, the difference of both distributions has a total area under the curve of zero. The total bone turnover is calculated as shown in equation 2.2. This turnover describes the absolute loss of bone mass over between the two groups and is equal to the mean value of the difference curve.

The differences between the sexes can be seen quite good in the difference curve. It can be observed, that men have a lower turnover than women. In the trabecular region, the loss is towards lower values in women. The zero crossing in the trabecular zone is at 18% BVTV for women, while it is at 34% for men. Also men loose less bone in the cortical region, which can be seen from the lower difference in this region.

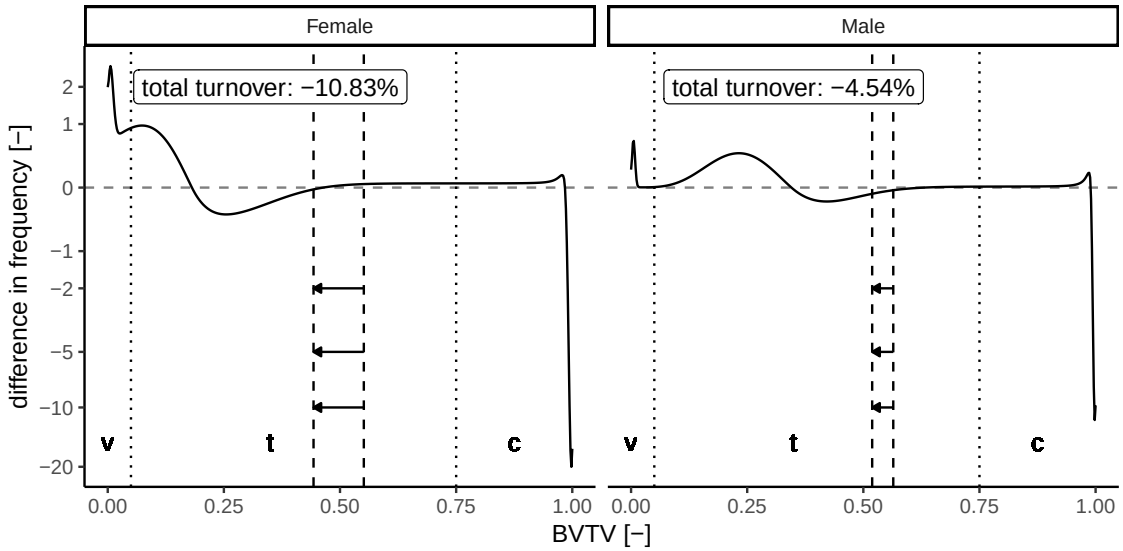

Figure 3.5: Differences of bone models. The three sections show the ranges which are used later in the linear model (see figure 3.7). **v**: voids (BVTV less than 5%), **t**: trabecular bone (BVTV between 5% and 75%), **c**: cortical bone (BVTV larger than 75%). The limits for cortical and trabecular bone were chosen based on local minima of the data itself, as no definite ranges were given in the literature.
The mean age difference for females was 25 years, while the mean age difference between males was 19 years. The dashed vertical lines indicate the mean of BVTV for the two groups. The arrows show that bone was lost, as the mean reduced over time. The length of the arrow is equal to the "total turnover".

3.1.3 BVTV Age Rate Model

The difference model describes the absolute change between the two groups. But as the mean age of each group might be different, the absolute value is not as good for a comparison than the rates of change. Linear models were created from the given BVTV frequency models. These models are useful, as the total turnover in the BVTV frequency difference models is given for the difference in mean ages between the groups. If the difference in mean ages are not equal, also the total turnover will vary, even if the actual rates of BVTV loss were equal.

Such a linear model for the total bone loss can be seen in figure 3.6, while figure 3.7 shows the model for separated cortical and trabecular bone using the thresholds (5% and 75%) shown in figure 3.5. No CoD as well as standard deviations can be calculated for those models, as the mean values for both groups were used directly, thus no residuals can be calculated. The slopes give the mean reduction of BVTV per year. Men have a lower rate in both the combined model as well as in the separated model. In the separated model, women have almost the same rate for both cortical and trabecular bone, while men have a twice as high rate for trabecular bone than for cortical bone.

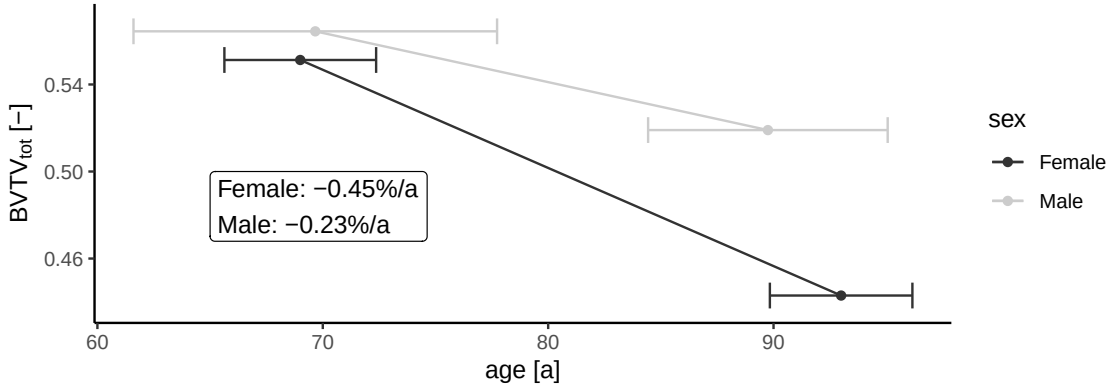

Figure 3.6: Age rate model for BVTV based on averages of BVTV. Shown are the mean ages for each group as well as the standard deviation of the ages. The slopes give the reduction in BVTV per year.

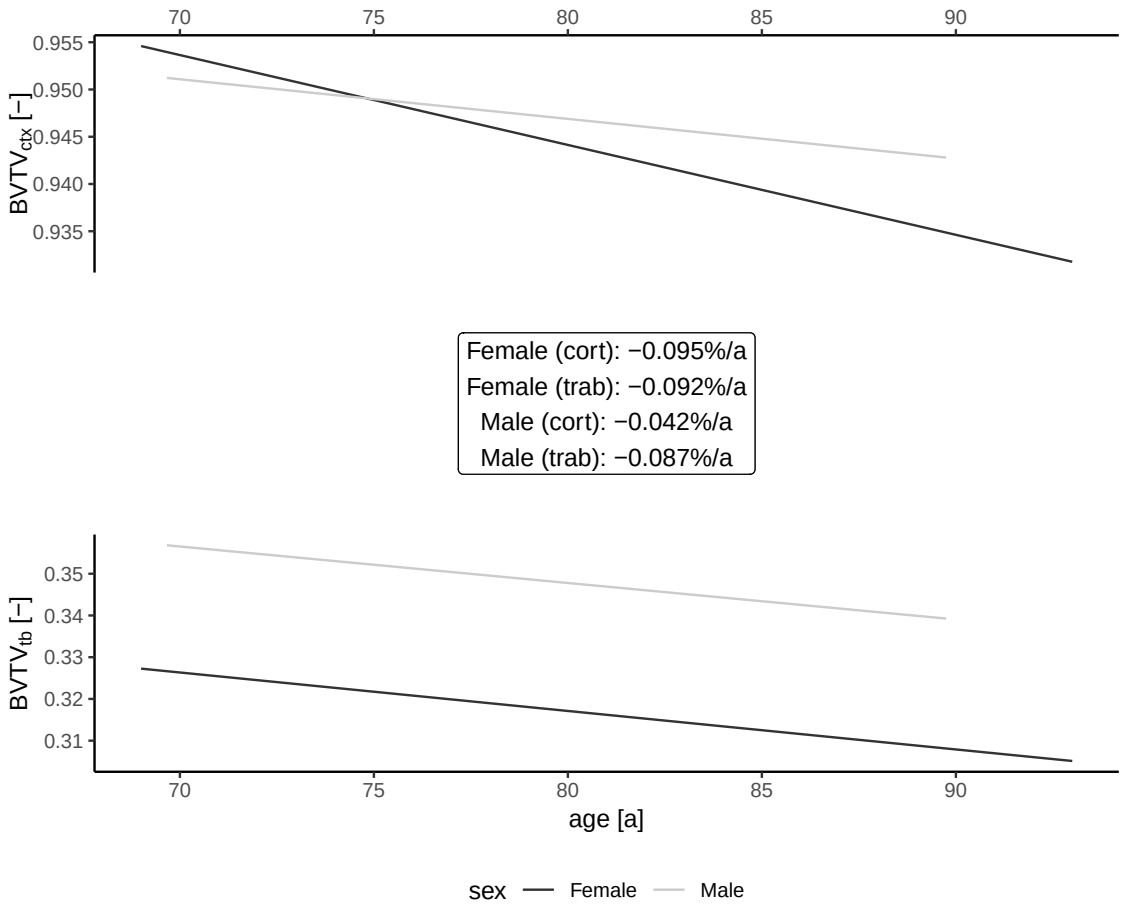

Figure 3.7: Age rate model for BVTV based on separation of cortical and trabecular bone. Cortical bone was defined as bone with a density higher than 75%, while trabecular bone was defined as bone with a density lower than 75% and higher than 5%.

3.1.4 Analytical Model

The rate based remodelling model with dependency to the BSTV model for bone was used to predict the changes of the BVTV frequency curve of the older group by using the younger group's curve as a starting point. This prediction was performed for each sex. This prediction should show if the changes in BVTV can be explained by the simple remodelling model and a simple geometrical model for the specific surface available.

The rate based remodelling model has three parameters, which need to be fitted for each sex. Two of those three parameters can be regarded as a single parameter, as they occur as a product in the rate equation. These parameters are c and R, the proportionality constant and the remodelling rate. The other parameter h describes the fraction of bone under remodelling. It was fixed to 0.1 but the parameters was also used as a variable in the grid search to observe the overall shape of the resulting function. The RSS of the predicted model and the older group's curve was used as a target value for minimisation.

RSS values for the range of parameters h and $c \cdot R$ are shown in figure 3.8. The RSS curve showed a hyperbolic behaviour, therefore one of the two parameters needs to be fixed in order to determine a minimal value. The resulting predicted curve which uses the parameters with minimal RSS can be seen in figure 3.10. The older group was not exactly replicated by the prediction, as the predicted curve deviates in many places from the older group's curve, which can also be observed by high RSS values.

Even though the predicted curve does not fit the older group's curve, certain aspects match the observed behaviour. The reduction in the cortical area is clearly visible and the shifted distribution can be seen in the trabecular region as well as increased voids. The increased height and broadening of the trabecular distribution was not predicted. The cortical peak was broader in the prediction than in the actual data.

Additionally to the geometrical model for BSTV, the function of LEREBOURS et al. [54] was implemented as well. Parameters were fitted in the same manner. The resulting RSS curve can be seen in figure 3.9. The RSS curve showed the same shape but the absolute values are higher than in the geometrical model, indicating a worse fit. The predicted curve can be seen in figure 3.11. Again, the older group's curve and the prediction do not match but the curve shows a similar behaviour as the geometrical model.

To observe the differences between the two predicted curves, the difference of the curves was calculated and is shown in figure 3.12. It can be seen, that both curves have the highest agreement in the region from around 0.05 to 0.9 - except for a minor peak in the lower trabecular region. The biggest disagreement is in the void area as well as in the cortical area. This difference means, that the model of LEREBOURS et al. [54] produces higher values at the extrema, as the difference is negative. In front of the negative peaks is always a positive peak as well, indicating that the geometry model shifts the values slightly away from the extremal values 0 and 1.

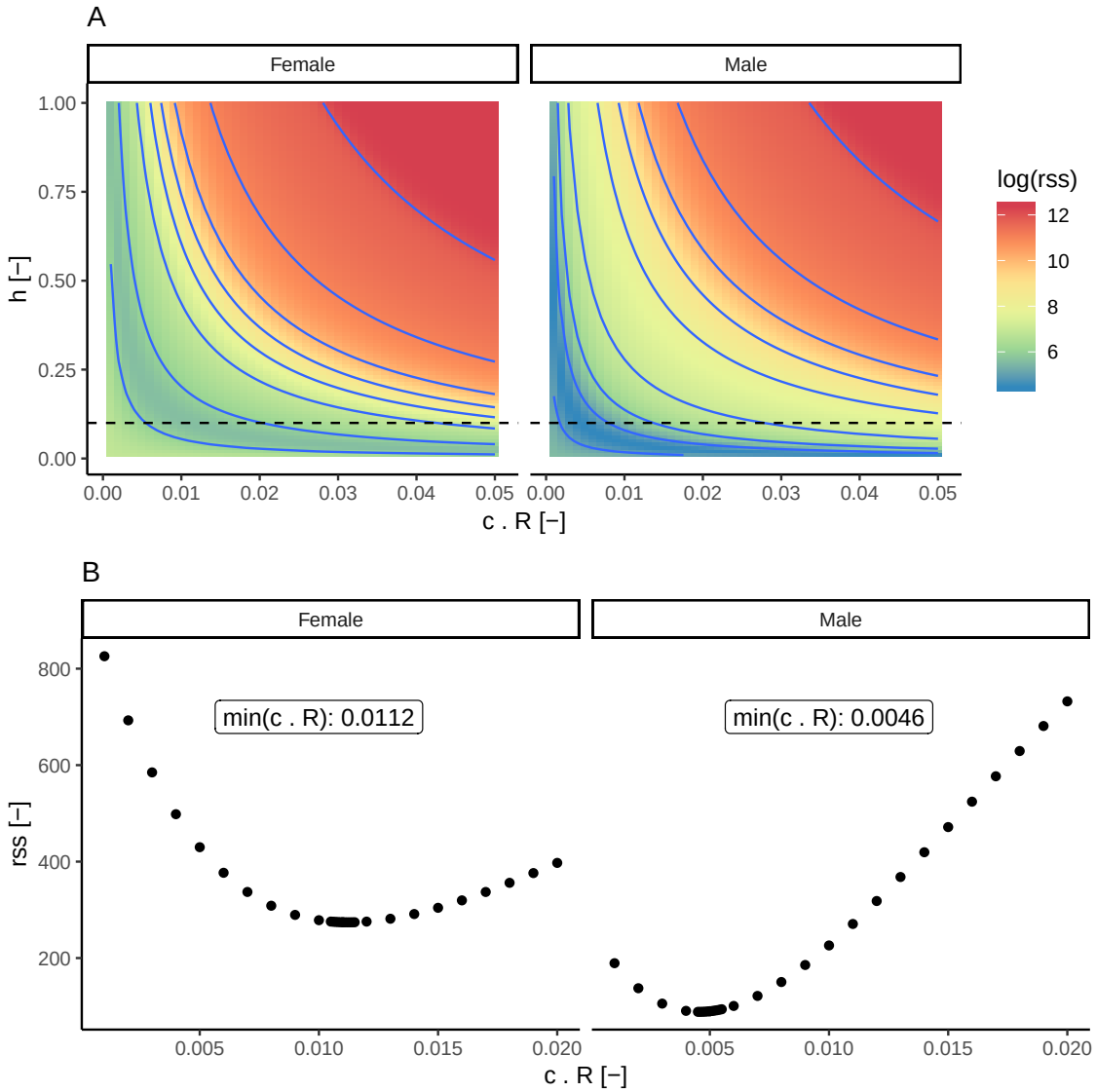

Figure 3.8: RSS between predicted and actual dataset. **A**: Overall behaviour of the RSS curve. As a minima can be found for each value of h, this parameter was fixed to 0.1, i.e. a 10% remodelling per time step (dashed line). **B**: shows the RSS for $h = 0.1$. The finer search region can be recognized by the higher amount of points near the minima of the curve.

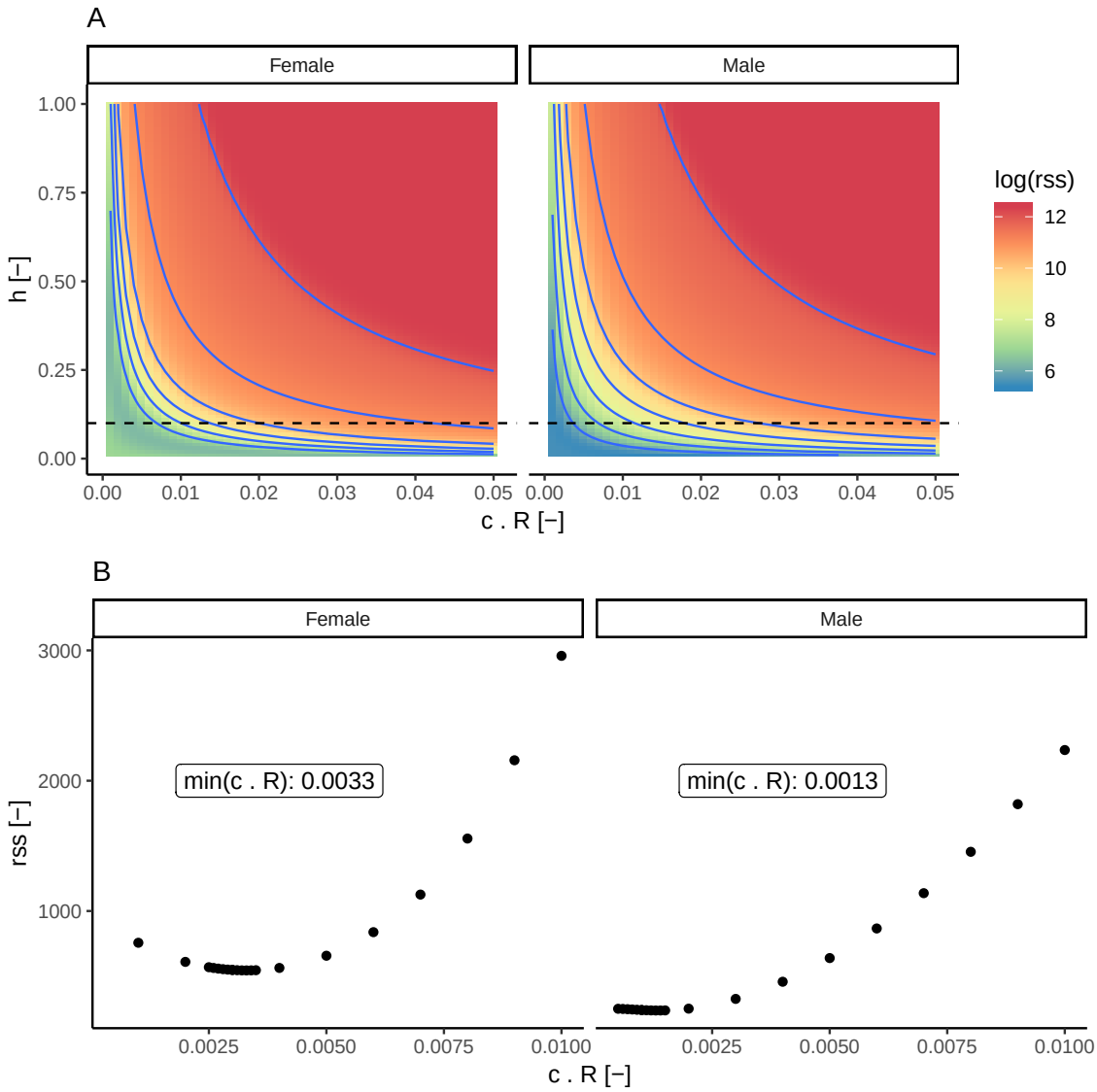

Figure 3.9: RSS between predicted and actual dataset for the BSTV equation of LEREBOURS et al. [54]. **A**: Overall behaviour of the RSS curve, the dashed line gives the fixated value for $h = 0.1$. **B**: shows the RSS for $h = 0.1$. For males, the curve looks like to be very close with the minimal value at the limits set for the search. The parameters for the BSTV model were set to $a = 6.25, b = 1$ to match the height of the geometry model.

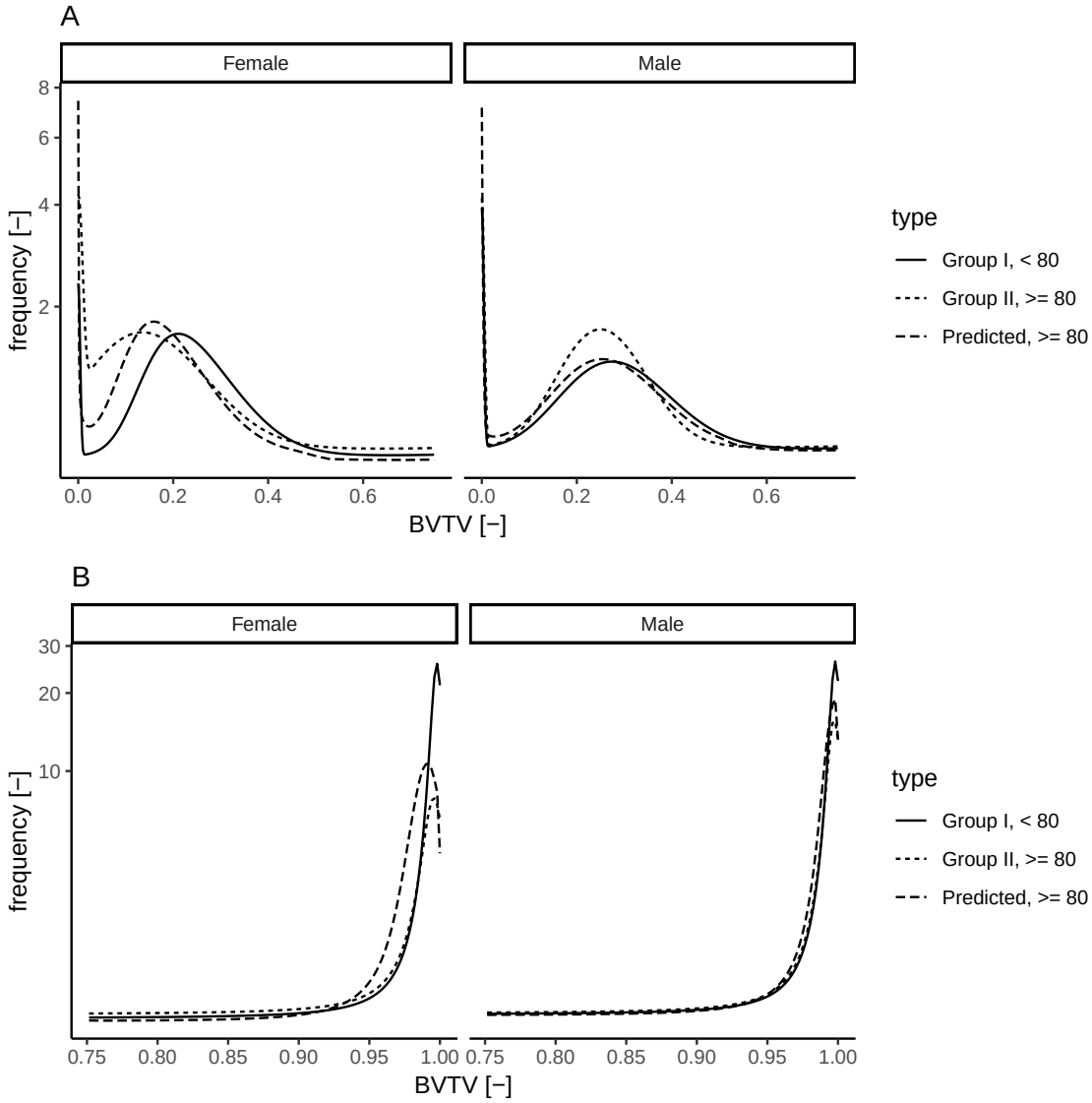

Figure 3.10: Resulting curve for the model with the lowest RSS, using parameters $h = 0.1, c = 1$ for both models and $R = 0.0112$ for females and $R = 0.0046$ for males. **A**: shows the curve from 0 to 0.75, **B**: shows the curve from 0.75 to 1.

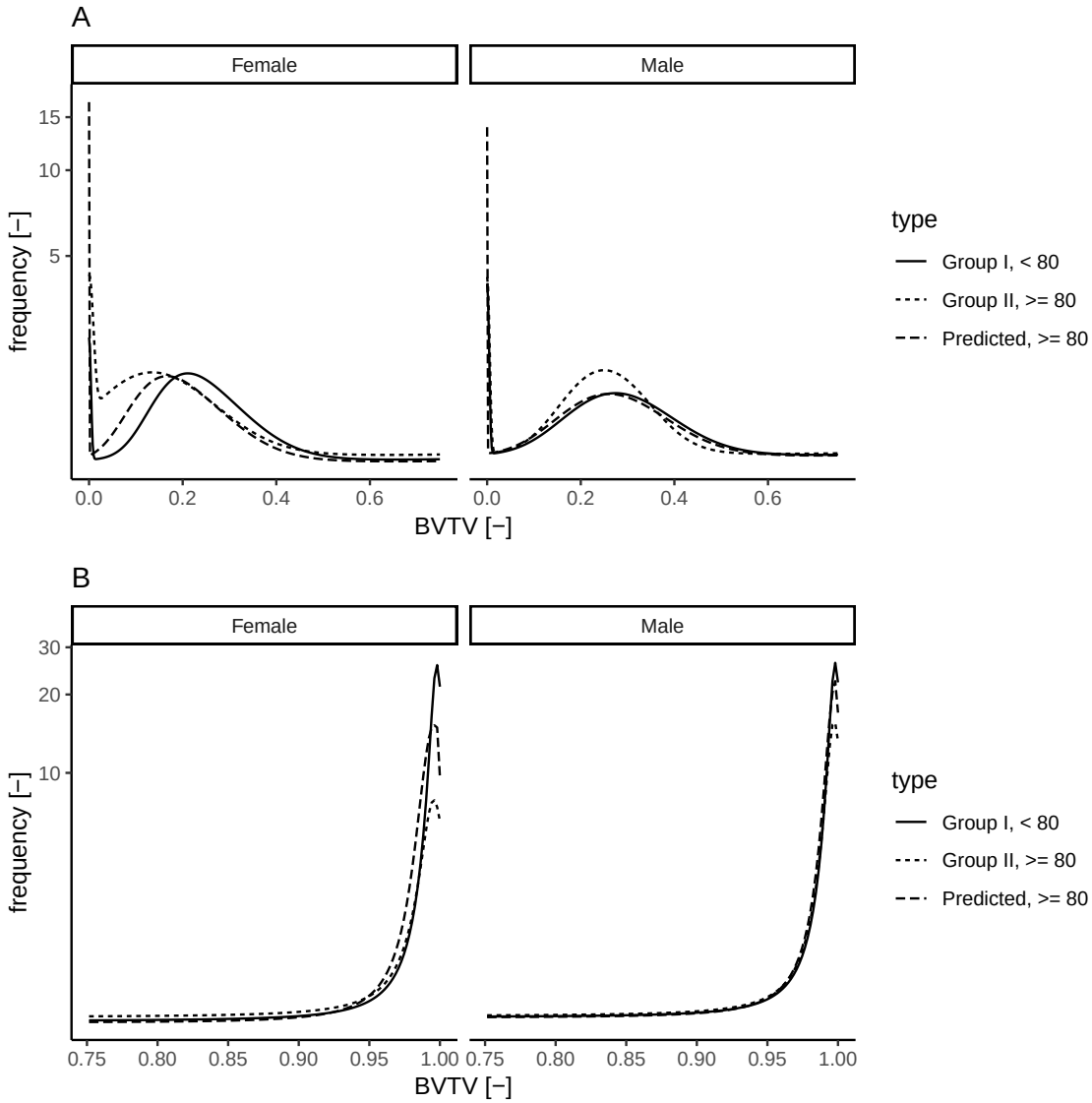

Figure 3.11: Resulting curve for the model with the lowest RSS using the BSTV model of LEREBOURS et al. [54], using parameters $h = 0.1, c = 1$ for both models and $R = 0.0033$ for females and $R = 0.0013$ for males. **A**: shows the curve from 0 to 0.75, **B**: shows the curve from 0.75 to 1.

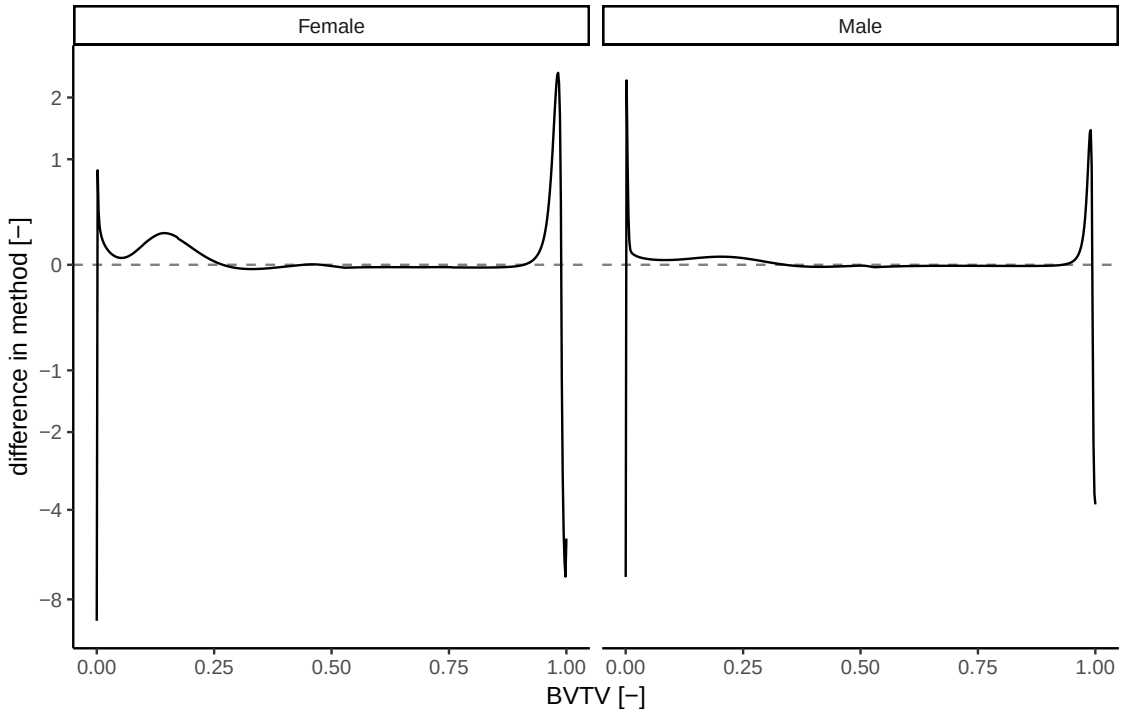

Figure 3.12: Difference in BSTV method. For both models with the lowest RSS. The value is calculated by subtracting the method of LEREBOURS et al. [54] from the geometry model.

3.2 HR-pQCT: Distal Radius Study Using Slices

To create comparable results, additional figures were calculated for the most distal $20.5\,\mathrm{mm}$ of the radius. All values were calculated using the *global* method, using a single VOI with the same size as the ROI. No differentiation was made between sexes, also no age groups were created. Differentiation between cortical and trabecular bone was made by the same masks as used for the frequency distributions. BVTV was calculated using the BMD approach instead of segmentation, $\mathrm{BMD_{max}}$ was set to $1200\,\mathrm{mgHA/cm^3}$ according to literature [103]. The calculated figures are given in table 3.3. $\mathrm{BMD_{tot}}$ can be compared to the figures of the whole segmented, given in table 3.1. It can be seen that the value of the whole segment ($520.53\,\mathrm{mgHA/cm^3}$) is much higher than $\mathrm{BVTV_{tot}}$ of the slice and is more comparable with $\mathrm{BMD_{ctx}}$ of the slice. This is not surprising, as the whole segment contains a lot more cortical bone than the slice. Only 14% of the total volume account for cortical bone in the slice, while the volume fraction of cortical bone in the whole segment is more than 40%.

		mean $\pm$ sd
$\mathrm{TV_{tot}}$	$[\mathrm{cm^3}]$	6.02 ± 1.02
$\mathrm{TV_{tb}}$	$[\mathrm{cm^3}]$	5.16 ± 0.84
$\mathrm{TV_{ctx}}$	$[\mathrm{cm^3}]$	0.86 ± 0.42
$\mathrm{BMC_{tot}}$	[mgHA]	1458.41 ± 663.8
$\mathrm{BMC_{tb}}$	[mgHA]	938.77 ± 382.88
$\mathrm{BMC_{ctx}}$	[mgHA]	519.65 ± 328.3
$\mathrm{BMD_{tot}}$	$[\mathrm{mgHA/cm^3}]$	234.82 ± 86.35
$\mathrm{BMD_{tb}}$	$[\mathrm{mgHA/cm^3}]$	179.31 ± 64.11
$\mathrm{BMD_{ctx}}$	$[\mathrm{mgHA/cm^3}]$	568.01 ± 80.37
$\mathrm{BVTV_{tb}}$[a]	[%]	14.94 ± 5.34

Table 3.3: Resulting figures for the most distal $20.5\,\mathrm{mm}$ of the radius. **a**: was calculated by dividing $\mathrm{BMD_{tb}}$ by $\mathrm{BMD_{max}}$ set to $1200\,\mathrm{mgHA/cm^3}$.

3.3 QCT: Proximal Femur and Lumbar Spine Set

In order to evaluate the method of BVTV frequency distributions on lower resolution data, such distributions were created from QCT images. These images were collected during the FREEDOM study at regular intervals of 12 months. Baseline age characteristics for the patients are given in table 3.4. In order to test if the available data was comparable to the whole cohort, a z-test was performed on the age data of the femur and vertebral samples. The test showed that there was no difference ($p = 0.0549$) for the placebo but a difference ($p = 0.0147$) for the treated group in comparison to the whole cohort in the vertebral samples. The femur samples showed no difference ($p = 0.257$) for the placebo group and also no difference ($p = 0.453$) for the treated group.

$\mathrm{BVTV}_{\mathrm{tot}}$ was calculated for each visit and normalized to the baseline by dividing each visit by the baseline BVTV. The resulting curve for the femur can be seen in figure 3.13. Both treated and placebo group showed an overall increase of BVTV over time. The results for the placebo group are distorted by two outliers. The majority of patients lost BVTV over time though. Figure 3.14 gives the same values for the vertebrae. The curves give an expected result, as the BVTV increased in the treated group but stayed the same on average for the placebo group.

BVTV frequency models were created for the QCT images using the same approach as for the HR-pQCT study: First, calculation of frequency distribution. Second, calculation of KDE per frequency distribution and third, calculation of mean KDE for each group. No curve fitting was applied to the mean KDE curves though.

The resulting BVTV frequency models for the femur can be seen in figure 3.15. Patients with Denosumab treatment showed a slight reduction in density at the lower BVTV levels and an increase in the higher levels. The overall change was very small though, which can be seen from the absolute values, given in table 3.5. The differences are not as pronounced as in the HR-pQCT data, which was expected as the duration of the trial was only 36 months. The vertebral BVTV frequency models are shown in figure 3.16. There is a reduction of BVTV in the lower region near the peak but an increase in the more dense zone for the treated group. Almost no difference can be seen in the placebo group.

The shape of the frequency curves is as expected. For the vertebrae, almost no cortical bone as well as void space can be seen. The articular processes were cut of during the image processing, thus very few cortical bone is in the image. These cuts were performed mainly because the image data was used for a FE study, which had no need for them. The rest of the vertebrae is filled with trabecular bone, thus the void spaces are missing in the curve as well. The femoral curve shows a larger portion of cortical bone, as well as a broader range of trabecular bone. Also void spaces are visible. Again, this can be explained by the shape of the bone. The femoral head has a thin cortex, filled with trabecular bone, while the shaft is hollow with a thicker cortex. In this sense, the femur shows a mixture of vertebrae and radius.

	Spine		Femur	
	Placebo (N=37)	Denosumab (N=43)	Placebo (N=23)	Denosumab (N=34)
Age (years)	74.0 ± 5.96	73.8 ± 3.97	73.2 ± 6.20	72.4 ± 4.41

Table 3.4: Baseline characteristics at the start of the study. Values are given as mean±sd.

		D1	M36	Difference
Femur	Denosumab	0.23824	0.25009	+1.18%
	Placebo	0.24265	0.23342	−0.92%
L1	Denosumab	0.13153	0.14258	+1.10%
	Placebo	0.13336	0.13409	+0.07%
L2	Denosumab	0.13196	0.14303	+1.11%
	Placebo	0.13229	0.13432	+0.02%

Table 3.5: Absolute changes of BVTV based on the BVTV frequency models for the baseline and 36 month dataset.

When the BVTV frequency models are created for each hospital, an effect of the usage of different devices and parameters can be seen. Figure 3.17 shows the BVTV frequency models for the femur and figure 3.18 for the vertebrae, both plotted per hospital. In both cases different shapes and number of modes can be observed.

As a last step, the BVTV frequency difference models between 36 months and baseline were calculated. These curves can be seen in figure 3.19 for femur and figure 3.20 for the vertebrae. It can be seen, that there was a reduction of low and an increase of high BVTV values in both bones for the treated groups. Both untreated groups showed an increase in the very low BVTV values and a decrease in higher values.

As the variability due to the different CT devices was too high, no further examinations were performed on the data.

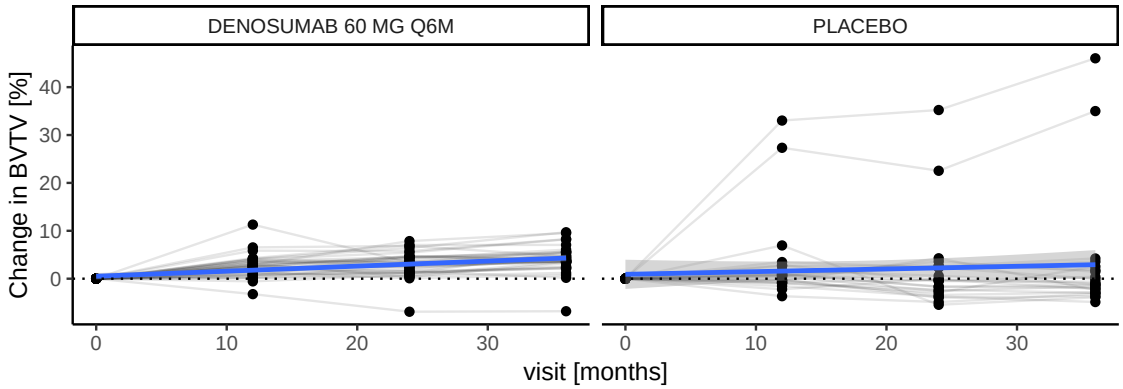

Figure 3.13: Normalized BVTV for each patient over treatment time for the proximal femur. The thick lines gives a linear model for the increase in BVTV.

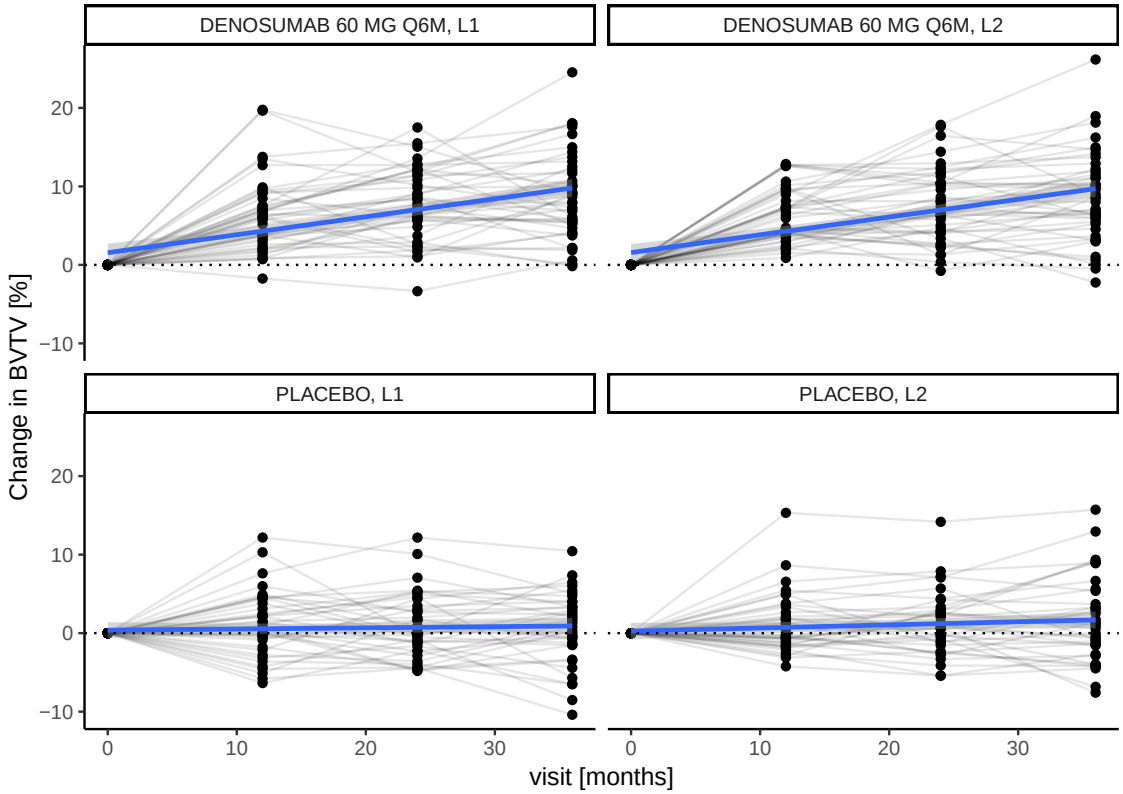

Figure 3.14: Normalized BVTV for each patient over treatment time for vertebrae (L1 and L2). The thick lines gives a linear model for the increase in BVTV.

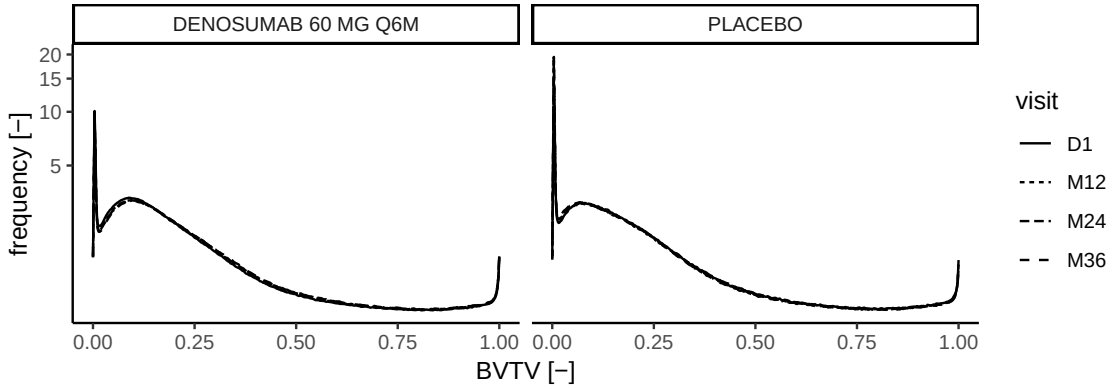

Figure 3.15: BVTV frequency model for the femur.

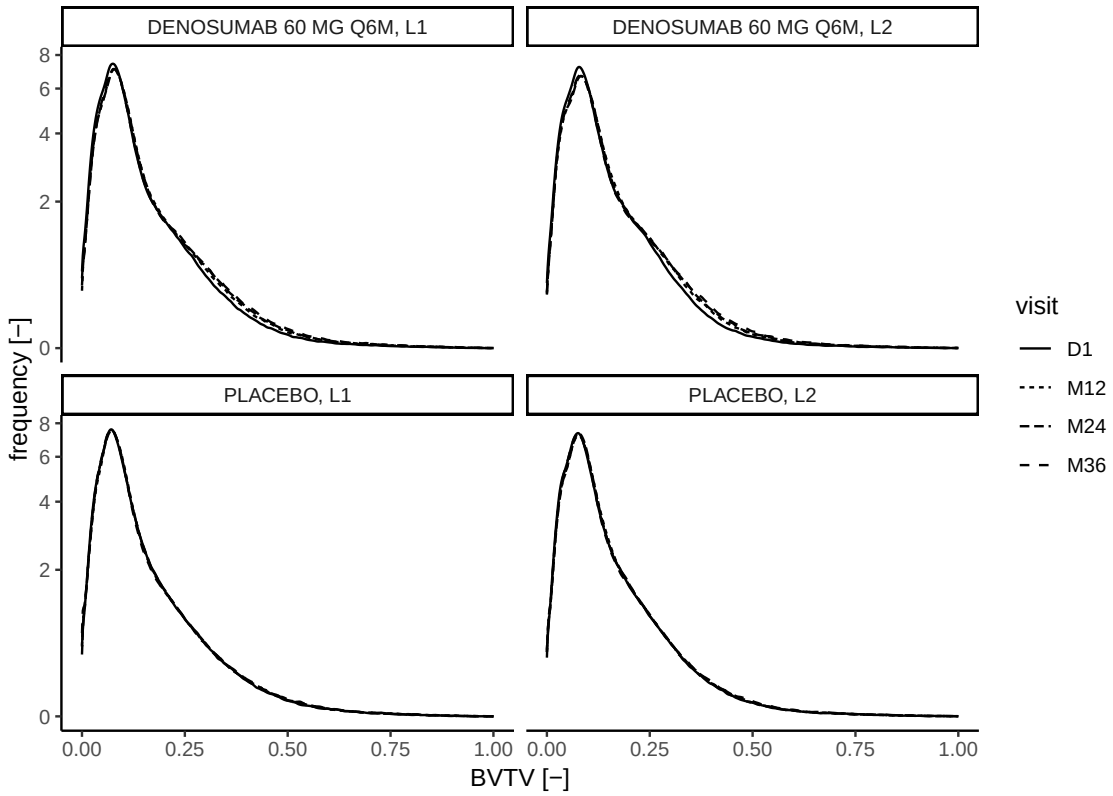

Figure 3.16: BVTV frequency model for vertebrae (L1 and L2).

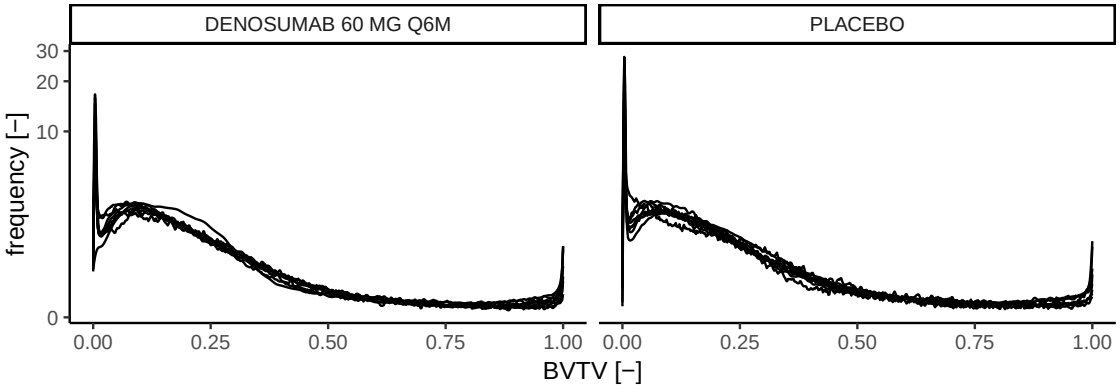

Figure 3.17: BVTV frequency model for the femur for the baseline only, split up per hospital.

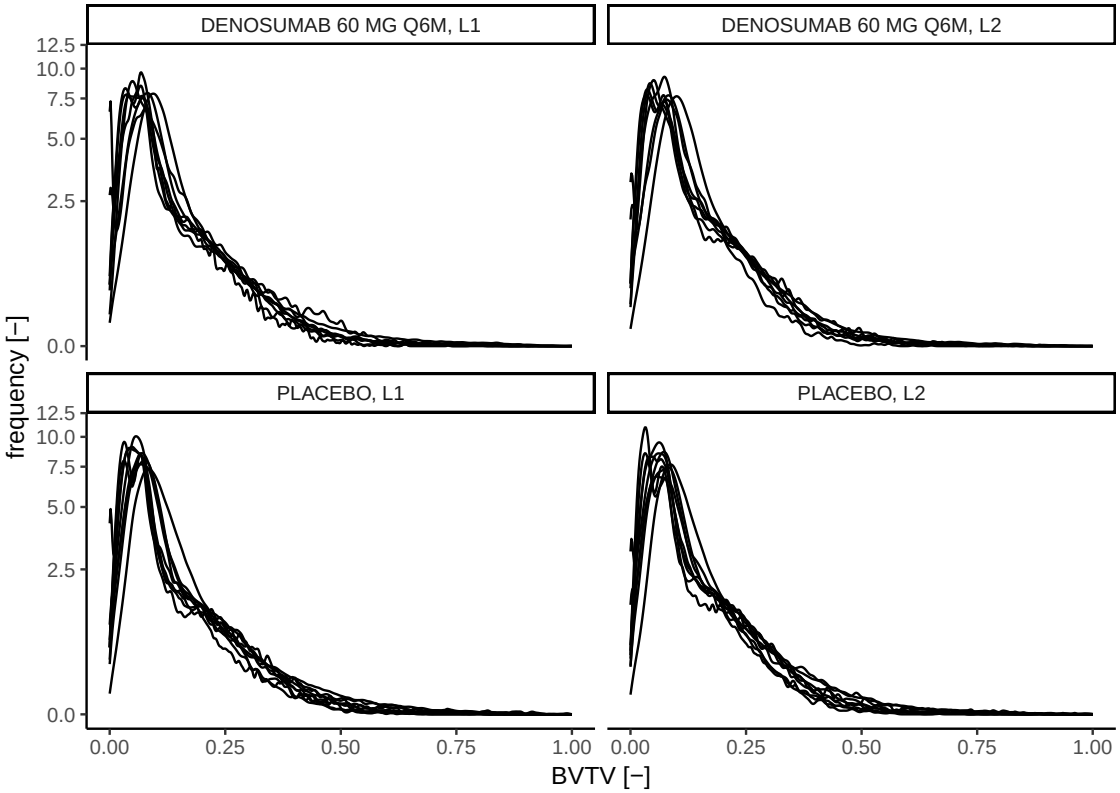

Figure 3.18: BVTV frequency model for vertebrae (L1 and L2) for the baseline split up per hospital.

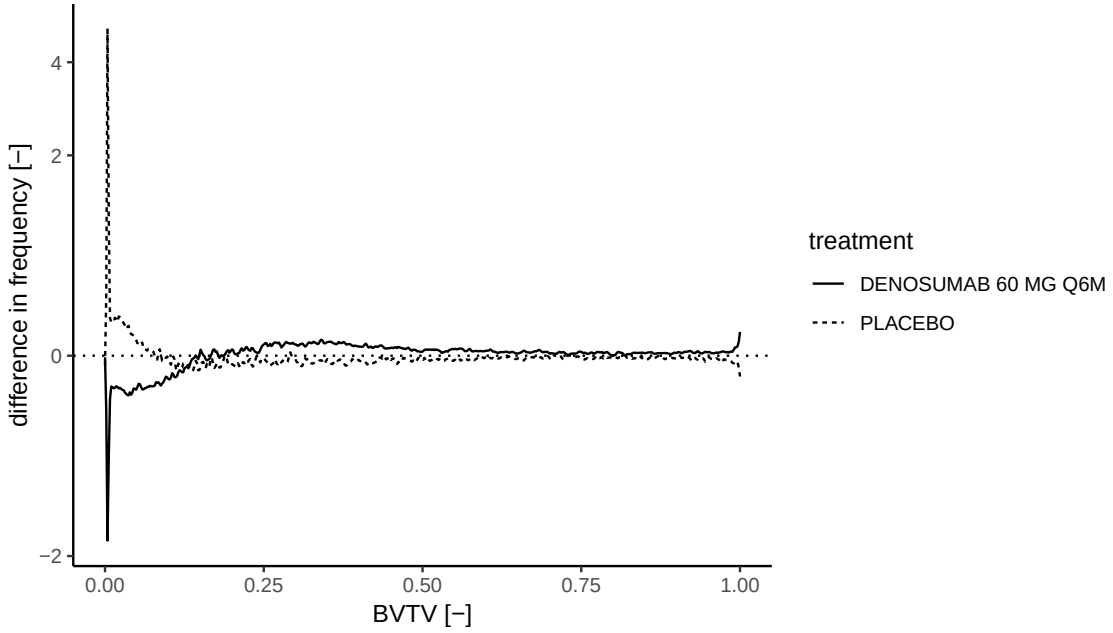

Figure 3.19: Differences between last image (36 months) and baseline for the femur.

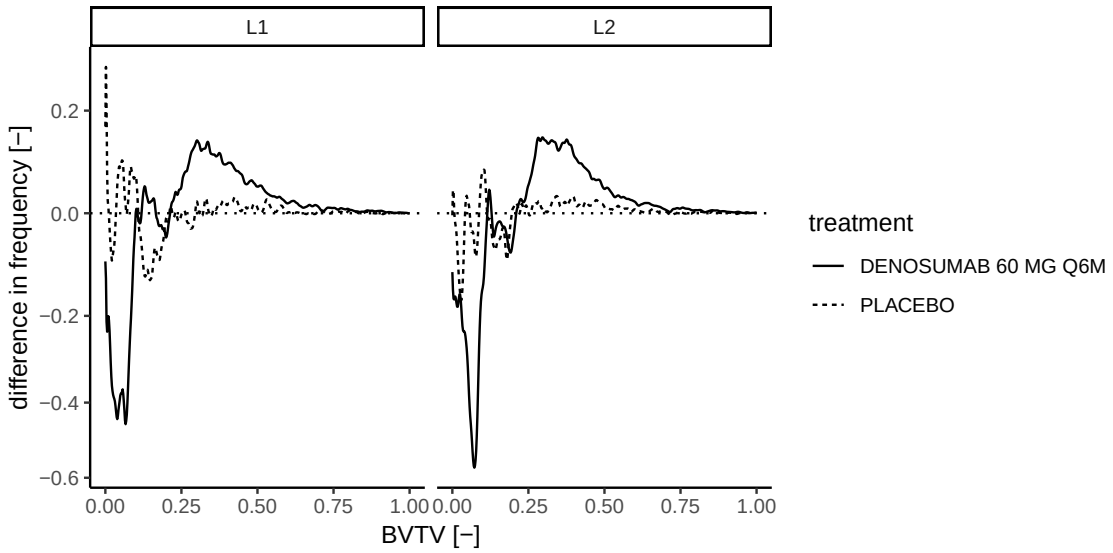

Figure 3.20: Differences between last image (36 months) and baseline for vertebrae (L1 and L2).

Chapter 4

Discussion

4.1 BVTV Frequency Distributions

Changes of bone mass are traditionally observed using mean values. Possible advantages of frequency distributions were investigated using the CT images of two different studies. HR-pQCT images of the radius were used in a first step to construct BVTV frequency distributions. Then the technique was applied to much coarser images of vertebrae and the femoral head which were taken using QCT. All the images were taken from existing studies and no additional information than already existing were required for the processing. Nevertheless, additional information would have been a good complement and could give new insights and open new possibilities for further processing. The process of evaluating the images is computational cheap and can be performed on regular workstations.

Additional models were created from the gathered frequency distributions. A difference model was constructed, which is able to show the differences in two frequency distributions. A linear rate model can be used to get rates in the traditional way using mean values, calculated directly from the frequency distribution. Both models were a useful visual aid, in order to see the changes of bone mass over time.

4.1.1 Age Related Changes Using HR-pQCT

An objective was defined to investigate the effects of ageing on the frequency distributions. Such age related changes in the BVTV frequency models were observed and were partially hypothesized beforehand. The resulting frequency distributions showed large deviations in the region of trabecular and cortical bone. Areas of less change are also visible. Not only were changes between age groups observed but also between sexes.

The trabecular distribution was shifting to the left, i.e. to lower BVTV values. These visual observations were also seen in the fitted parameters of the BVTV frequency model. The trabecular distribution's mean was lowered in both sexes. The distribution showed also a lower skewness, which indicates that the peak of the distribution is shifting faster than the tails. The cortical distribution did not changed as much as it was predicted. It did not shift as large as the trabecular part but diminished in height.

The changes can also be observed in the BVTV frequency difference model. It can be seen that cortical

and trabecular bone shifted to the left. The asymmetry of the trabecular shift is clearly visible, as the positive peak is larger than the negative peak. This indicates that the total BVTV decreased. Again, the changes to the cortical distribution are not as expected. It was hypothesized that the cortical distribution would show signs of increased porosity, thus show a shift to the left. But these changes might be concealed by the other distributions and are not easily distinguishable a posteriori as bone is regarded as trabecular rather than cortical [111]. A solution could be the separation of the cortical/trabecular transition zone [110] and the creation of individual models for each zone.

Comparison with existing studies is possible by calculating mean values from the distributions. Such linear rate models were created for age as a parameter. Additional rates for trabecular and cortical region were calculated from the overall distribution. HUNG et al. [44] used HR-pQCT to determine age related effects at the distal radius, thus this study is well suited for a comparison. This study was only conducted on women. The comparison can only be made using the figures for trabecular bone, as they note that their regression model for cortical bone is quadratic and not linear. The mean BVTV at the age group of 20 is given with 13.8% and an absolute reduction of 6% was observed until the age of 89. The associated rate can be calculated with $0.087\,\%/\mathrm{a}$, which is close to the value observed in the age rate model ($0.092\,\%/\mathrm{a}$). The absolute mean value for the age of 89 would be 7.8%, which is much lower than the absolute mean value for this age given by the age rate model, which is around 30%. This difference in absolute values might be explained by the choice of ROI.

Not only BVTV distributions were created but also the total volumes were calculated for each sample, separated by trabecular and cortical region. These data was surveyed in order to connect the findings with the changes in BVTV. The changes in volume give expected results. The cortical volume is decreasing while the trabecular volume is increasing. These findings go along with the already known cortex thinning and increasing endosteal diameter [88, 93]. If the endosteal diameter is increasing, but the cortical shell is thinning, then the trabecular core must increase in volume. The bone volume in the cortical region is decreasing while the bone volume in the trabecular region stays the same. One explanation for this behaviour might be the suspected porous cortex. More and more parts of the cortex are accounted as trabecular structure by the bone separation algorithm, as the porosity increases over a certain threshold. Due to this uncertainty in classification, it might be concluded, that the trabecular distribution gains enough density from cortical bone, to maintain the bone volume, even though the total volume is shrinking.

The BVTV curve for women ≥ 80 had unexpected low values of BVTV in the range below 5%. The porosity of trabecular bone is given with 70% to 80%, which would be a BVTV of about 20% to 30% [99]. But the given values in the literature might not be useful, because no reference volume size is given, nor the place at which this porosity is measured. Usually volumes completely filled with trabecular bone are used. This can be either a section of the femoral head, vertebrae or distal regions of radius or tibia [35]. As the whole scan of the radius was used to generate the BVTV histogram, it also contains a large section of diaphysis, where no trabecular bone is found. Also the transition area between trabecular bone and diaphysis might influence the measurement. Similar like the border zone between cortical and trabecular bone produces higher values than expected, also the zone between trabecular bone and marrow space might give lower values than expected.

A BVTV age rate model for cortical and trabecular bone was created. Men showed twice as high rates in the trabecular region than in the cortex, while women had similar rates in both parts of bone. But

the separation between cortical and trabecular bone in the linear age rate model raises some questions. A separation was performed using a BVTV threshold of 75%. All values below 5% are regarded as not belonging to the trabecular volume. While the cortical threshold seems to be work fine, the cut off below 5% might be problematic. The rationale for this cut off is the fact that the whole bone segmented was chosen as ROI. Thus, the ROI contains the medullary cavity which accounts for the void distribution. In order to separate "true" trabecular distribution from the overall distribution, a lower threshold must be defined. But also trabecular bone contains some intertrabecular voids. Maybe it is sufficient to change the cut off value to a lower number. Depending on the bone and VOI size, minimal values for BVTV are 3.65% ($4\,\mathrm{mm}$ VOI, transiliac bone) [70], 4% to 11.8% ($4\,\mathrm{mm}$ VOI, iliac crest / femoral head) [42], 5.37% ($4\,\mathrm{mm}$ VOI, calcaneus) [100], 7.17% (whole organ, L3) [87] and up to 22% (Distal Radius) [82]. Additional studies would be required in order to find the correct value for a given VOI size and bone.

A single threshold might not give pleasing results as it is also possible that the lower zone is actually a mixture of different distributions, namely the (medullary) voids, intertrabecular voids and the trabecular distribution. Such a mixture cannot easily be distinguished by a simple thresholding method. Threshold independent method for bone separation, also called labelling, are available and might give better results than the threshold based separation which was used in this work [102]. Also machine learning can be used for such tasks [104]. But non-threshold separation models usually require some sort of spatial information, which is already lost in the BVTV frequency model. Therefore, such models can only be applied at the stage of image processing and separated models must be created.

The values for the cortical distribution as shown in the BVTV frequency distribution were unforeseen high. Values for the mean were expected to be in the range of 88% to 90% [14] but were always larger than 99.5%. This behaviour could be explained due to the use of segmented bone images. Small pores and channels are not visible in the segmented HR-pQCT images. One solution would be higher resolution CT like micro CT (μCT), where the isotropic resolution is in the range of tens of $\mu\mathrm{m}$. Voxel sizes in the range of single $\mu\mathrm{m}$ are possible when using synchrotron radiation [52]. Even higher resolutions are possible with special CT, down to the sub-$\mu\mathrm{m}$ range [9]. All pores and channels are imaged correctly if such a resolution is used, as Haversian channels are in the range of $10\,\mu\mathrm{m}$ to $300\,\mu\mathrm{m}$ [105]. A single lacunae is in the range of $10\,\mu\mathrm{m}$. It might not even be necessary to conduct such efforts in order to see age related effects due to pores. The porosity based on lacunae is a function of age but not based on Haversian channels [105]. Therefore, it might be possible to use devices with a resolution of about $10\,\mu\mathrm{m}$.

In order to have more comparable parameters, the radius data was evaluated again using a slice approach which was described in literature [103]. Ten different figures were calculated for the most distal $20.5\,\mathrm{mm}$. While the total volume sizes are lower for the current data set, both BMC and BMD are higher. The largest difference shows $\mathrm{BVTV_{tb}}$, where VARGA et al. [103] reported 8.31 ± 2.70, while the current data gives 14.94 ± 5.34. But as both BMC and BMD are higher, also $\mathrm{BVTV_{tb}}$ must be higher. The age distribution is lower in the current data set (mean$\pm$sd: 79.17 ± 12.28 vs 81.2 ± 13.7) but the range is almost equal (min/max: $54/97$ vs $59/97$).

The slice approach was not investigated further as the slice method caused difficulties. The inter-specimen variability was large, due to different bone volumes in the slice. Using the whole limb resolves this problem, as the larger ROI size has an averaging effect. Many CT based studies use slices of bone though but many different methods are used at the radius [8, 45, 98]. Some of those methods work only if

the joint is visible in the scan, as the starting point is defined as the mid-joint line. As the scans were taken *ex-vivo*, no carpal bones were scanned. Other methods use a fixed length from an anatomical landmark but do not take into account the actual bone length and size. Therefore, the results are hard to comparable inside the group. A method of normalizing would be required to give comparable results. A standard method is %-of-total-limb ROI [4]. But neither the total length nor other anthropometric figures were available for the radius data set. Therefore, none of the slice methods worked on the radius data, as the inter-specimen variability was too high for the slices and normalization was not possible. Using the whole segment reduced the variability. Another reason for the usage of whole segment was the ability to construct a distribution from both cortical and trabecular bone at the same time. Most slice methods return only a small sample of cortical bone, as the cortex is much thinner in the distal part than in the diaphysis.

4.1.2 Changes in BVTV Frequency Distribution Using QCT

Bone frequency models were also created using QCT images of femur and vertebrae. The femoral head as well as the vertebral body do not contain much cortex, thus these models had almost only a trabecular distribution. But no theoretical model for the overall BVTV distribution was available. Therefore, no curve fitting was applied to the frequency distribution, Additionally the images showed a high variability between hospitals, although the devices were calibrated. The difference in voxel size and possible internal image processing of the QCT devices lead to the decision to not investigate further.

The study design differed from the radius study, as four consecutive images were created every year. Changes due to treatment and ageing (in the placebo group) can be seen in the series of BVTV frequency model. But also the placebo group increased on average in BVTV, which was not found in the study which used the same data set and the same ROI [113]. One reason might be a difference in the image processing. From the frequency difference models, a change in BVTV was observed. In comparison to the placebo group, treated patient gained bone in higher BVTV regions. This is indicated by a shift of the curve to the right side. Lower BVTV values are "lost", while higher values are gained. These changes are almost exclusively in the trabecular region below a BVTV of 75%.

A separation between cortical and trabecular distribution is impeded by the imbalance in volume fractions. Both vertebrae and femoral head did not contained much cortical bone. KEAVENY et al. [48] noted the difficulty when separating the influence of cortex and trabecular bone from each other in QCT images. The cortex is very thin in both femur and vertebrae and the low resolution leads to partial volume effects which hinder the exact differentiation between cortical and trabecular bone.

4.1.3 Analytical Model for BSTV and Remodelling

A simple geometry model for the relationship of BVTV to BSTV was created. The objective was to determine if such a model could be used in a remodelling tool to predict age related changes of the radius. A combined model of geometry and remodelling, called analytical model, was used to predict the older group's distribution based on the younger group's distribution as an input parameter.

The overall performance of the analytical model is not great, as the BVTV frequency curve of the older group was not exactly recreated. But the model shows the overall trend of ageing. The region with the largest changes is the trabecular region. The analytical model showed the ability to shift the trabecular

mean as well as skew the trabecular distribution to the left. It had also the ability to shrink the amount of cortical bone but induced a larger shift as shown in the BVTV frequency distributions.

There are many possibilities why the analytical model cannot reproduce the ageing effects. One of them might be, that the here found relationship between BVTV and BSTV is too simple. The shape matches the proposed "dome shape figure" of MARTIN [64] and LEREBOURS et al. [54]. But the reduction of the whole microstructure to one or two cylinders might be one step too much. In reality, the number of pores or trabeculae is much higher. Especially the large number of smaller pores has an influence on the ratio of surface to volume. Bone does not consist of circular or cylindrical shapes alone, but the microstructure of trabecular bone can also be divided into rods and plates [95]. It is also stated, that there is a shift from plate-like structure to a rod-like structure in ageing [41]. A more sophisticated model might include pores in different distributions as well as different types of geometry. To also test the influence of the BSTV model, the proposed model of LEREBOURS et al. [54] was also implemented but showed similar behaviour with the exception of producing very different values at the extremal BVTV values. There are certainly other parameters which affect the remodelling besides the specific surface.

The analytical model introduced two new, *a-priori* unknown parameters. In order to find values for these parameters, a exhaustive grid search was performed, minimizing the RSS of the two functions. While RSS might be a good parameter for minimization of a function, the limits are shown in the fitting of the parameters for the prediction model. The resulting RSS might be very high, although the curve fits partially. Curve similarity measures, like the Fréchet distance or time warping algorithms might be a better choice to fit the parameters [25].

4.2 Further Research

The most influential parameter is the position and size of the ROI. Therefore, much care should be taken when choosing a ROI. It is suggested to investigate the effect of different ROI positions and sizes in an advanced study more closely. Also the size of the VOI as well as segmentation method and parameters must be chosen carefully.

The cortical distribution can be refined by using higher resolution CT images in the range of several $\mu\mathrm{m}$. Using a different separation approach could help to get better results at the cortical border. One possibility would be to separate it from the two distributions and add the cortical/trabecular transition zone as a third distribution.

The observed changes in BVTV are often very small, especially in the QCT study. It is not clear if the observed changes are due to changed bone or stem from noise. This problem arises especially in longitudinal studies, where only a few months are between individual images. The sources of error should be investigated more closely, in order to produce better results. Using larger datasets would help to reduce the dispersion of the dataset. Also the range of ages could be extended to younger ages, as the youngest subjects were already over the age of 50.

4.3 Conclusions

BVTV frequency models give additional insight into the changes of bone due to age, sex, diseases or treatment. They give more information than a single value as the regions of activity are visible in the model. The successful application of BVTV frequency models was shown at the example of HR-pQCT data for observing age related changes. Such models can also be used with QCT, but additional models for each bone are required. The analytical model was too simple in order to explain the non-linearities of the bone frequency model but improvements to this model are possible. BSTV might not be the only factor influencing remodelling, thus more parameters might be required in order to create a working model. There are still many challenges in order to create robust models but this pilot study shows the advantage of this methods as being an easy and computational cheap way for creating remodelling models. Existing HR-pQCT data can be re-evaluated using the frequency model to get more insights into changes of bone without any harm for the patient and at low cost. Improvements to the current model might be made by using higher resolution images and larger data sets.

Appendix A

Appendix

A.1 Sum of Volume Fractions in PDF for BVTV

A generalized form of the PDF for the total BVTV, $f_{\mathrm{BVTV}}\colon [0,1] \to \mathbb{R}_0^+$ might be given by n different PDF $p_i\colon \mathbb{R} \to \mathbb{R}_0^+$ and volume fractions φ_i:

$$f_{\mathrm{BVTV}}(x) = \sum_{i=1}^{n} \varphi_i \, p_i(x) \tag{A.1}$$

Each PDF p has the following property:

$$\int_{-\infty}^{\infty} p(x)\, dx = 1 \tag{A.2}$$

In order to have each φ describe the actual fraction of the integral, each individual PDF p must have an integral of one. But as the input space of f_{BVTV} is defined as $[0,1]$ and each p has an input space of $\mathbb{R}$, the integral of p might not necessarily be one. It is the case, that the integral will be always less or equal to 1 and larger or equal to zero:

$$0 \leq \int_0^1 p(x)dx \leq 1 \tag{A.3}$$

Integrating f_{BVTV} leads to:

$$\int_0^1 f_{\mathrm{BVTV}}(x)dx = \sum_{i=1}^{n} \varphi_i \underbrace{\int_0^1 p(x)dx}_{[0,1]} = 1 \tag{A.4}$$

That means, that φ might be larger in order to "compensate" for the lower integral value. It can be concluded, that the sum of all φ might be equal or larger than one.

It is very easy to construct a simple example, where the sum of the volume fractions is not one, even when only a single PDF is used. By using a normal distribution with $\mu = 0$ and $\sigma = 1$, the integral between 0 and 1 is approximately 0.341. That means that the associated φ must be approximately 2.932 in order to ensure the integral of f_{BVTV} is one.

A.2 Simple Geometry Model for Specific Surface

For trabecular bone, there are no inclusions but dense cylinders. In a simple case, n bone cylinders with radius r are inside a volume of length L. If those cylinders do not intersect each other, a set of equation can be given:

$$\mathrm{BVTV_{tb}} = \frac{n\pi r^2}{L^2} \tag{A.5}$$

$$\mathrm{BSTV_{tb}} = \frac{2n\pi}{L}\sqrt{\frac{\mathrm{BVTV_{tb}}}{n\pi}} \tag{A.6}$$

A more difficult model for trabecular structure are two or three intersecting cylinders. Each cylinder has the same radius and all cylinders will intersect in the middle. In this case, the equations need to be modified by a correction term, which is actually the volume or the area of a Steinmetz solid. For the bicylinder, the volume can be calculated as $V = \frac{16}{3}r^3$ and the surface area as $A = 16r^2$.

For the bicylinder case, equations A.5 and A.6 need to be modified using the correction term:

$$\mathrm{BVTV_{tb}} = \frac{2L\pi r^2 - \frac{16}{3}r^3}{L^3} \tag{A.7}$$

$$\mathrm{BSTV_{tb}} = \frac{4L\pi r - 16r^2}{L^3} \tag{A.8}$$

It is required, that $L \geq \frac{4r}{\pi}$, otherwise the result will be a negative surface.

The equations be solved for $\mathrm{BVTV_{tb}}$ by applying Cardano's method. The discriminant is always negative, as $\mathrm{BVTV_{tb}}$ and $L > 0$:

$$\Delta = \frac{9}{8192}(-8\,\mathrm{BVTV_{tb}^2}\,L^6 - \pi\,\mathrm{BVTV_{tb}}\,L^4) \tag{A.9}$$

Therefore, three real solution exists. Only r_2 gives a valid result, which reads as:

$$r_2 = -\sqrt{-\frac{4}{3}p}\cos\left(\frac{1}{3}\ \arccos\left(-\frac{q}{2}\sqrt{-\frac{27}{p^3}}\right) + \frac{\pi}{3}\right) + \frac{L\pi}{8} \tag{A.10}$$

with

$$p = -\frac{3}{64}L^2\pi^2, \qquad q = -\frac{L^3\pi^3 - 48\,\mathrm{BVTV_{tb}}\,L^3}{256} \tag{A.11}$$

By setting p and q into equation A.10:

$$r_2 = -\frac{L\pi}{4}\cos\left(\frac{1}{3}\arccos\left(1 - \frac{48\,\mathrm{BVTV_{tb}}}{\pi^3}\right) + \frac{\pi}{3}\right) + \frac{L\pi}{8} \tag{A.12}$$

and finally putting equation A.12 into A.6, the result is:

$$\mathrm{BSTV_{tb}} = \frac{\pi^2}{L}\left(\frac{1}{4} - \sin^2\left(\frac{1}{3}\arcsin\left(1 - \frac{48\,\mathrm{BVTV_{tb}}}{\pi^3}\right)\right)\right) \tag{A.13}$$

There is also the possibility to include three intersecting cylinders into the model. The correction terms

are $V = (16 - 8\sqrt{2})r^3$ and $A = 3(16 - 8\sqrt{2})r^2$.

The resulting equations are now:

$$\mathrm{BVTV_{tb}} = \frac{2L\pi r^2 - \left(16 - 8\sqrt{2}\right) r^3}{L^3} \tag{A.14}$$

$$\mathrm{BSTV_{tb}} = \frac{4L\pi r - 3\left(16 - 8\sqrt{2}\right) r^2}{L^3} \tag{A.15}$$

Both equations can be solved by the same method as the Steinmetz 2-solid.

Bibliography

[1] A. AZZALINI. "A Class of Distributions Which Includes the Normal Ones". In: *Scandinavian Journal of Statistics* 12.2 (1985), pp. 171–178.

[2] N. BACHL et al. "Motomir - experiment muscle strength diagnosis under conditions of weightlessness". In: *Space Technology* 16 (1996), pp. 215–230.

[3] G. BOIVIN and P. MEUNIER. "The Degree of Mineralization of Bone Tissue Measured by Computerized Quantitative Contact Microradiography". In: *Calcified Tissue International* 70.6 (2002), pp. 503–511.

[4] S. BONARETTI et al. "The comparability of HR-pQCT bone measurements is improved by scanning anatomically standardized regions". In: *Osteoporosis International* 28.7 (2017), pp. 2115–2128.

[5] L. F. BONEWALD. "The amazing osteocyte". In: *Journal of Bone and Mineral Research* 26.2 (2011), pp. 229–238.

[6] L. F. BONEWALD and M. L. JOHNSON. "Osteocytes, mechanosensing and Wnt signaling". In: *Bone* 42.4 (2008), pp. 606–615.

[7] E. BONUCCI. "Basic composition and structure of bone". In: *Mechanical testing of bone and the bone-implant interface*. CRC Press, 2000, pp. 3–21.

[8] S. BOUTROY et al. "In VivoAssessment of Trabecular Bone Microarchitecture by High-Resolution Peripheral Quantitative Computed Tomography". In: *The Journal of Clinical Endocrinology & Metabolism* 90.12 (2005), pp. 6508–6515.

[9] O. BRUNKE et al. "Comparison between x-ray tube-based and synchrotron radiation-based micro-CT". In: *Developments in X-Ray Tomography VI*. SPIE, 2008.

[10] S. BUTZ et al. "Forearm BMD as measured by peripheral quantitative computed tomography (pQCT) in a German reference population". In: *Osteoporosis International* 4.4 (1994), pp. 179–184.

[11] P. R. CAVANAGH, A. A. LICATA, and A. J. RICE. "Exercise and pharmacological countermeasures for bone loss during long-duration space flight." In: *Gravitational and space biology bulletin : publication of the American Society for Gravitational and Space Biology* 18 (2 2005), pp. 39–58.

[12] H. CHEN et al. "Age- and gender-dependent changes in three-dimensional microstructure of cortical and trabecular bone at the human femoral neck". In: *Osteoporosis International* 21.4 (2009), pp. 627–636.

[13] H. CHEN et al. “Age-Related Changes in Trabecular and Cortical Bone Microstructure”. In: *International Journal of Endocrinology* 2013 (2013), pp. 1–9.

[14] S. C. COWIN. *Bone Mechanics Handbook, Second Edition*. Informa UK Limited, 2001.

[15] W.-Q. CUI et al. “Age-and region-dependent changes in three-dimensional microstructural properties of proximal femoral trabeculae”. In: *Osteoporosis International* 19.11 (2008), pp. 1579–1587.

[16] S. R. CUMMINGS et al. “Denosumab for Prevention of Fractures in Postmenopausal Women with Osteoporosis”. In: *New England Journal of Medicine* 361.8 (2009), pp. 756–765.

[17] E. DALL’ARA et al. “A nonlinear QCT-based finite element model validation study for the human femur tested in two configurations in vitro”. In: *Bone* 52.1 (2013), pp. 27–38.

[18] N. DALZELL et al. “Bone micro-architecture and determinants of strength in the radius and tibia: age-related changes in a population-based study of normal adults measured with high-resolution pQCT”. In: *Osteoporosis International* 20.10 (2009), pp. 1683–1694.

[19] D. W. DEMPSTER et al. “Standardized nomenclature, symbols, and units for bone histomorphometry: A 2012 update of the report of the ASBMR Histomorphometry Nomenclature Committee”. In: *Journal of Bone and Mineral Research* 28.1 (2012), pp. 2–17.

[20] J. E. DENNIS, D. M. GAY, and R. E. WALSH. “An Adaptive Nonlinear Least-Squares Algorithm”. In: *ACM Transactions on Mathematical Software* 7.3 (1981), pp. 348–368.

[21] M. DJURIC et al. “Region-Specific Sex-Dependent Pattern of Age-Related Changes of Proximal Femoral Cancellous Bone and Its Implications on Differential Bone Fragility”. In: *Calcified Tissue International* 86.3 (2009), pp. 192–201.

[22] C. L. DONALDSON et al. “Effect of prolonged bed rest on bone mineral”. In: *Metabolism* 19.12 (1970), pp. 1071–1084.

[23] J. N. DOWTHWAITE, P. P. FLOWERS, and T. A. SCERPELLA. “Agreement between pQCT- and DXA-derived indices of bone geometry, density, and theoretical strength in females of varying age, maturity, and physical activity”. In: *Journal of Bone and Mineral Research* 26.6 (2011), pp. 1349–1357.

[24] E. R. DRAPER et al. “Novel Assessment of Bone Using Time-Resolved Transcutaneous Raman Spectroscopy”. In: *Journal of Bone and Mineral Research* 20.11 (2005), pp. 1968–1972.

[25] A. EFRAT, Q. FAN, and S. VENKATASUBRAMANIAN. “Curve Matching, Time Warping, and Light Fields: New Algorithms for Computing Similarity between Curves”. In: *Journal of Mathematical Imaging and Vision* 27.3 (2006), pp. 203–216.

[26] K. ENGELKE et al. “Clinical Use of Quantitative Computed Tomography (QCT) of the Hip in the Management of Osteoporosis in Adults: the 2015 ISCD Official PositionsPart I”. In: *Journal of Clinical Densitometry* 18.3 (2015), pp. 338–358.

[27] J. S. FINKELSTEIN et al. “Bone Mineral Density Changes during the Menopause Transition in a Multiethnic Cohort of Women”. In: *The Journal of Clinical Endocrinology & Metabolism* 93.3 (2008), pp. 861–868.

[28] H. M. FROST. “Bone mass and the mechanostat: a proposal”. In: *The anatomical record* 219.1 (1987), pp. 1–9.

[29] D. FYHRIE et al. “Human vertebral cancellous bone surface distribution”. In: *Bone* 17.3 (1995), pp. 287–291.

[30] R. I. GAFNI and J. BARON. “Childhood Bone Mass Acquisition and Peak Bone Mass May Not Be Important Determinants of Bone Mass in Late Adulthood”. In: *Pediatrics* 119.Supplement 2 (2007), pp. 131–136.

[31] D. GATTI et al. “Effect of aging on trabecular and compact bone components of proximal and ultradistal radius”. In: *Osteoporosis International* 6.5 (1996), pp. 355–360.

[32] H. K. GENANT et al. “Noninvasive assessment of bone mineral and structure: State of the art”. In: *Journal of Bone and Mineral Research* 11.6 (2009), pp. 707–730.

[33] L. J. GIBSON. “Biomechanics of cellular solids”. In: *Journal of Biomechanics* 38.3 (2005), pp. 377–399.

[34] M. M. GIRAUD-GUILLE. “Twisted plywood architecture of collagen fibrils in human compact bone osteons”. In: *Calcified Tissue International* 42.3 (1988), pp. 167–180.

[35] S. A. GOLDSTEIN. “The mechanical properties of trabecular bone: Dependence on anatomic location and function”. In: *Journal of Biomechanics* 20.11-12 (1987), pp. 1055–1061.

[36] C. M. GORDON et al. “The Determinants of Peak Bone Mass”. In: *The Journal of Pediatrics* 180 (2017), pp. 261–269.

[37] M. A. HARTMANN et al. “Trabecular bone remodelling simulated by a stochastic exchange of discrete bone packets from the surface”. In: *Journal of the Mechanical Behavior of Biomedical Materials* 4.6 (2011), pp. 879–887.

[38] T. HAYASHI et al. “Analysis of bone mineral density distribution at trabecular bones in thoracic and lumbar vertebrae using X-ray CT images”. In: *Journal of Bone and Mineral Metabolism* 29.2 (2010), pp. 174–185.

[39] R. P. HEANEY et al. “Peak Bone Mass”. In: *Osteoporosis International* 11.12 (2001), pp. 985–1009.

[40] C. J. HERNANDEZ, G. S. BEAUPRE, and D. R. CARTER. “A theoretical analysis of the relative influences of peak BMD, age-related bone loss and menopause on the development of osteoporosis”. In: *Osteoporosis International* 14.10 (2003), pp. 843–847.

[41] T. HILDEBRAND and P. REGSEGGER. “Quantification of Bone Microarchitecture with the Structure Model Index”. In: *Computer Methods in Biomechanics and Biomedical Engineering* 1.1 (1997), pp. 15–23.

[42] T. HILDEBRAND et al. “Direct Three-Dimensional Morphometric Analysis of Human Cancellous Bone: Microstructural Data from Spine, Femur, Iliac Crest, and Calcaneus”. In: *Journal of Bone and Mineral Research* 14.7 (1999), pp. 1167–1174.

[43] R. HUISKES and S. J. HOLLISTER. “From Structure to Process, From Organ to Cell: Recent Developments of FE-Analysis in Orthopaedic Biomechanics”. In: *Journal of Biomechanical Engineering* 115.4B (1993), p. 520.

[44] V. W. Y. HUNG et al. “Age-related differences in volumetric bone mineral density, microarchitecture, and bone strength of distal radius and tibia in Chinese women: a high-resolution pQCT reference database study”. In: *Osteoporosis International* 26.6 (2015), pp. 1691–1703.

[45] IAEA. *Dual Energy X Ray Absorptiometry For Bone Mineral Density And Body Composition Assessment: IAEA Human Health Series No. 15*. International Atomic Energy Agency, 2011.

[46] J. A. KANIS et al. “Development and use of FRAX in osteoporosis”. In: *Osteoporosis International* 21.S2 (2010), pp. 407–413.

[47] S. KAPTOGE et al. “Geographical variation in DXA bone mineral density in young European men and women. Results from the Network in Europe on male osteoporosis (NEMO) study”. In: *Bone* 43.2 (2008), pp. 332–339.

[48] T. M. KEAVENY et al. “Femoral and Vertebral Strength Improvements in Postmenopausal Women With Osteoporosis Treated With Denosumab”. In: *Journal of Bone and Mineral Research* 29.1 (2013), pp. 158–165.

[49] J. S. KENKRE and J. H. D. BASSETT. “The bone remodelling cycle”. In: *Annals of Clinical Biochemistry: International Journal of Laboratory Medicine* 55.3 (2018), pp. 308–327.

[50] L. KONG et al. *Intersecting Cylinders: From Archimedes and Zu Chongzhi to Steinmetz and Beyond*. Tech. rep. University of Illinois at Urbana-Champaign, 2013.

[51] L. E. LANYON. “Osteocytes, strain detection, bone modeling and remodeling”. In: *Calcified Tissue International* 53.S1 (1993), pp. 102–107.

[52] A. LARRUE et al. “Synchrotron Radiation Micro-CT at the Micrometer Scale for the Analysis of the Three-Dimensional Morphology of Microcracks in Human Trabecular Bone”. In: *PLoS ONE* 6.7 (2011).

[53] A. D. LEBLANC et al. “Bone mineral loss and recovery after 17 weeks of bed rest”. In: *Journal of Bone and Mineral Research* 5.8 (2009), pp. 843–850.

[54] C. LEREBOURS et al. “The relationship between porosity and specific surface in human cortical bone is subject specific”. In: *Bone* 72 (2015), pp. 109–117.

[55] K. S. LEUNG et al. “Characteristics of Long Bone DXA Reference Data in Hong Kong Chinese”. In: *Journal of Clinical Densitometry* 7.2 (2004), pp. 192–200.

[56] J. B. LIAN and G. S. STEIN. “Concepts of Osteoblast Growth and Differentiation: Basis for Modulation of Bone Cell Development and Tissue Formation”. In: *Critical Reviews in Oral Biology & Medicine* 3.3 (1992), pp. 269–305.

[57] X. S. LIU et al. “Bone density, geometry, microstructure, and stiffness: Relationships between peripheral and central skeletal sites assessed by DXA, HR-pQCT, and cQCT in premenopausal women”. In: *Journal of Bone and Mineral Research* 25.10 (2010), pp. 2229–2238.

[58] A. C. LOOKER et al. “Updated Data on Proximal Femur Bone Mineral Levels of US Adults”. In: *Osteoporosis International* 8.5 (1998), pp. 468–490.

[59] J. LU et al. “Peak Bone Mass and Patterns of Change in Total Bone Mineral Density and Bone Mineral Contents From Childhood Into Young Adulthood”. In: *Journal of Clinical Densitometry* 19.2 (2016), pp. 180–191.

[60] H. M. MACDONALD et al. “Age-related patterns of trabecular and cortical bone loss differ between sexes and skeletal sites: A population-based HR-pQCT study”. In: *Journal of Bone and Mineral Research* 26.1 (2010), pp. 50–62.

[61] J. A. MACNEIL and S. K. BOYD. “Accuracy of high-resolution peripheral quantitative computed tomography for measurement of bone quality”. In: *Medical Engineering & Physics* 29.10 (2007), pp. 1096–1105.

[62] A. MAKKER et al. “Normative bone mineral density data at multiple skeletal sites in Indian subjects”. In: *Archives of Osteoporosis* 3.1-2 (2008), pp. 25–37.

[63] P. MAQUET, J. WOLFF, and R. FURLONG. *The Law of Bone Remodelling*. Springer Berlin Heidelberg, 2012.

[64] R. B. MARTIN. “Porosity and specific surface of bone”. In: *Crit Rev Biomed Eng* (1984).

[65] R. M. MARTIN and P. H. S. CORREA. “Bone quality and osteoporosis therapy”. In: *Arquivos Brasileiros de Endocrinologia & Metabologia* 54.2 (2010), pp. 186–199.

[66] P. MILOVANOVIC et al. “Porotic paradox: distribution of cortical bone pore sizes at nano- and micro-levels in healthy vs. fragile human bone”. In: *Journal of Materials Science: Materials in Medicine* 28.5 (2017).

[67] J.-Y. MIN et al. “Age curves of bone mineral density at the distal radius and calcaneus in Koreans”. In: *Journal of Bone and Mineral Metabolism* 28.1 (2009), pp. 94–100.

[68] E. R. MOREY-HOLTON and R. K. GLOBUS. “Hindlimb unloading rodent model: technical aspects”. In: *Journal of Applied Physiology* 92.4 (2002), pp. 1367–1377.

[69] R. MLLER et al. “Morphometric Analysis of Human Bone Biopsies: A Quantitative Structural Comparison of Histological Sections and Micro-Computed Tomography”. In: *Bone* 23.1 (1998), pp. 59–66.

[70] R. MLLER et al. “Morphometric Analysis of Human Bone Biopsies: A Quantitative Structural Comparison of Histological Sections and Micro-Computed Tomography”. In: *Bone* 23.1 (1998), pp. 59–66.

[71] NATIONAL INSTITUTES OF HEALTH. *Bone Mass Measurement: What the Numbers Mean*. 2015.

[72] K. K. NISHIYAMA et al. “Postmenopausal Women With Osteopenia Have Higher Cortical Porosity and Thinner Cortices at the Distal Radius and Tibia Than Women With Normal aBMD: AnIn VivoHR-pQCT Study”. In: *Journal of Bone and Mineral Research* (2009).

[73] L. de OLIVEIRA and R. LOPES. “3D histomorphometric quantification from 3D computed tomography”. In: *Nuclear Instruments and Methods in Physics Research Section A: Accelerators, Spectrometers, Detectors and Associated Equipment* 525.1-2 (2004), pp. 406–411.

[74] D. H. PAHR and P. K. ZYSSET. “From high-resolution CT data to finite element models: development of an integrated modular framework”. In: *Computer Methods in Biomechanics and Biomedical Engineering* 12.1 (2009), pp. 45–57.

[75] A. M. PARFITT et al. “Relationships between surface, volume, and thickness of iliac trabecular bone in aging and in osteoporosis. Implications for the microanatomic and cellular mechanisms of bone loss.” In: *Journal of Clinical Investigation* 72.4 (1983), pp. 1396–1409.

[76] A. M. PARFITT et al. “Bone histomorphometry: Standardization of nomenclature, symbols, and units: Report of the asbmr histomorphometry nomenclature committee”. In: *Journal of Bone and Mineral Research* 2.6 (2009), pp. 595–610.

[77] I. H. PARKINSON and N. L. FAZZALARI. “Characterisation of Trabecular Bone Structure”. In: *Studies in Mechanobiology, Tissue Engineering and Biomaterials*. Springer Berlin Heidelberg, 2012, pp. 31–51.

[78] R DEVELOPMENT CORE TEAM. *R: A Language and Environment for Statistical Computing*. ISBN 3-900051-07-0. R Foundation for Statistical Computing. Vienna, Austria, 2008.

[79] E. A. RENATE LLLMANN-RAUCH. *Taschenlehrbuch Histologie*. Thieme Georg Verlag, 2015. 752 pp.

[80] L. S. RICHELSON et al. “Relative Contributions of Aging and Estrogen Deficiency to Postmenopausal Bone Loss”. In: *New England Journal of Medicine* 311.20 (1984), pp. 1273–1275.

[81] B. van RIETBERGEN and K. ITO. “A survey of micro-finite element analysis for clinical assessment of bone strength: The first decade”. In: *Journal of Biomechanics* 48.5 (2015), pp. 832–841.

[82] B. van RIETBERGEN et al. “In Vivo Assessment of Architecture and Micro-Finite Element Analysis Derived Indices of Mechanical Properties of Trabecular Bone in the Radius”. In: *Osteoporosis International* 13.1 (2002), pp. 6–17.

[83] B. L. RIGGS et al. “Changes in Bone Mineral Density of the Proximal Femur and Spine with Aging”. In: *Journal of Clinical Investigation* 70.4 (1982), pp. 716–723.

[84] J. RITTWEGER et al. “Muscle atrophy and bone loss after 90 days’ bed rest and the effects of flywheel resistive exercise and pamidronate: Results from the LTBR study”. In: *Bone* 36.6 (2005), pp. 1019–1029.

[85] R. RIZZOLI et al. “Maximizing bone mineral mass gain during growth for the prevention of fractures in the adolescents and the elderly”. In: *Bone* 46.2 (2010), pp. 294–305.

[86] P. ROSCHGER et al. “Validation of quantitative backscattered electron imaging for the measurement of mineral density distribution in human bone biopsies”. In: *Bone* 23.4 (1998), pp. 319–326.

[87] J.-P. ROUX et al. “Contribution of Trabecular and Cortical Components to Biomechanical Behavior of Human Vertebrae: An Ex Vivo Study”. In: *Journal of Bone and Mineral Research* 25.2 (2009), pp. 356–361.

[88] C. RUFF and W. HAYES. “Subperiosteal expansion and cortical remodeling of the human femur and tibia with aging”. In: *Science* 217.4563 (1982), pp. 945–948.

[89] M. D. RYSER, N. NIGAM, and S. V. KOMAROVA. “Mathematical Modeling of Spatio-Temporal Dynamics of a Single Bone Multicellular Unit”. In: *Journal of Bone and Mineral Research* 24.5 (2009), pp. 860–870.

[90] E. SCHOENAU et al. “The Development of Bone Strength at the Proximal Radius during Childhood and Adolescence”. In: *The Journal of Clinical Endocrinology & Metabolism* 86.2 (2001), pp. 613–618.

[91] S. J. SHEATHER and M. C. JONES. “A Reliable Data-Based Bandwidth Selection Method for Kernel Density Estimation”. In: *Journal of the Royal Statistical Society* 53.3 (1991), pp. 683–690.

[92] R. S. SIFFERT and J. J. KAUFMAN. “Ultrasonic bone assessment: The time has come”. In: *Bone* 40.1 (2007), pp. 5–8.

[93] R. W. SMITH and R. R. WALKER. “Femoral Expansion in Aging Women: Implications for Osteoporosis and Fractures”. In: *Science* 145.3628 (1964), pp. 156–157.

[94] M. SODE et al. “Regional variations of gender-specific and age-related differences in trabecular bone structure of the distal radius and tibia”. In: *Bone* 46.6 (2010), pp. 1652–1660.

[95] M. STAUBER and R. MLLER. “Volumetric spatial decomposition of trabecular bone into rods and platesA new method for local bone morphometry”. In: *Bone* 38.4 (2006), pp. 475–484.

[96] A. SYNEK et al. “The influence of bone density and anisotropy in finite element models of distal radius fracture osteosynthesis: Evaluations and comparison to experiments”. In: *Journal of Biomechanics* 48.15 (2015), pp. 4116–4123.

[97] D. D. THOMPSON. “Age changes in bone mineralization, cortical thickness, and Haversian canal area”. In: *Calcified Tissue International* 31.1 (1980), pp. 5–11.

[98] S. TSUZUKU et al. “Bone Mineral Density Obtained by Peripheral Quantitative Computed Tomography (pQCT) in Middle-Aged and Elderly Japanese”. In: *Journal of Epidemiology* 10.1sup (2000), pp. 39–45.

[99] C. H. TURNER and D. B. BURR. “Experimental techniques for bone mechanics”. In: *Bone mechanics handbook* 2 (2001).

[100] D. ULRICH et al. “The ability of three-dimensional structural indices to reflect mechanical aspects of trabecular bone”. In: *Bone* 25.1 (1999), pp. 55–60.

[101] H. K. VNNEN et al. “The cell biology of osteoclast function.” In: *Journal of cell science* 113 (Pt 3) (2000), pp. 377–381.

[102] A. VALENTINITSCH et al. “Automated threshold-independent cortex segmentation by 3D-texture analysis of HR-pQCT scans”. In: *Bone* 51.3 (2012), pp. 480–487.

[103] P. VARGA et al. “Validation of an HR-pQCT-based homogenized finite element approach using mechanical testing of ultra-distal radius sections”. In: *Biomechanics and Modeling in Mechanobiology* 10.4 (2010), pp. 431–444.

[104] Q. WANG et al. *Machine Learning in Medical Imaging: 8th International Workshop, MLMI 2017, Held in Conjunction with MICCAI 2017, Quebec City, QC, Canada, September 10, 2017, Proceedings*. Lecture Notes in Computer Science. Springer International Publishing, 2017.

[105] X. WANG and Q. NI. “Determination of cortical bone porosity and pore size distribution using a low field pulsed NMR approach”. In: *Journal of Orthopaedic Research* 21.2 (2003), pp. 312–319.

[106] L. WARMING, C. HASSAGER, and C. CHRISTIANSEN. “Changes in Bone Mineral Density with Age in Men and Women: A Longitudinal Study”. In: *Osteoporosis International* 13.2 (2002), pp. 105–112.

[107] R. D. WASNICH et al. “Changes in bone density and turnover after alendronate or estrogen withdrawal”. In: *Menopause* 11.6, Part 1 of 2 (2004), pp. 622–630.

[108] G. D. WHEDON. “Disuse osteoporosis: Physiological aspects”. In: *Calcified Tissue International* 36.S1 (1984), pp. 146–150.

[109] X. P. WU et al. “A Comparison Study of the Reference Curves of Bone Mineral Density at Different Skeletal Sites in Native Chinese, Japanese, and American Caucasian Women”. In: *Calcified Tissue International* 73.2 (2003), pp. 122–132.

[110] R. ZEBAZE et al. “A new method of segmentation of compact-appearing, transitional and trabecular compartments and quantification of cortical porosity from high resolution peripheral quantitative computed tomographic images”. In: *Bone* 54.1 (2013), pp. 8–20.

[111] R. ZEBAZE and E. SEEMAN. “Cortical Bone: A Challenging Geography”. In: *Journal of Bone and Mineral Research* 30.1 (2014), pp. 24–29.

[112] P. ZIOUPOS, R. B. COOK, and J. R. HUTCHINSON. “Some basic relationships between density values in cancellous and cortical bone”. In: *Journal of Biomechanics* 41.9 (2008), pp. 1961–1968.

[113] P. ZYSSET et al. “Comparison of proximal femur and vertebral body strength improvements in the FREEDOM trial using an alternative finite element methodology”. In: *Bone* 81 (2015), pp. 122–130.